Università degli Studi di Bologna

Facoltà di Scienze Matematiche Fisiche e Naturali

Dottorato di Ricerca in Fisica, XVIII Ciclo

Area 02 - Scienze Fisiche: FIS/04 Fisica Nucleare e Subnucleare

PhD Thesis

A study of hadron yields and spectra with the ALICE experiment at LHC

Dr. Chiara Zampolli

Advisor:
Prof.
Luisa Cifarelli

PhD Coordinator:
Prof.
Roberto Soldati

Bologna, Italy, 2006

Contents

Introduction

Ultrarelativistic heavy-ion experiments have recently become a foreground subject in experimental physics. The very high centre-of-mass energies they deal with open the door to the exploration of new regimes, in terms of temperature of the system created in the collision, of available phase-space regions, and of reachable energy densities. This should allow to study a new state of matter, the so-called *quark-gluon plasma* (QGP). The QGP should result from a phase transition ordinary matter is expected to undergo when driven to extremely high temperatures and energy densities. It is a state in which quarks and gluons are thought to interact freely, not bound to form colour-singlet hadrons, and presumably with the quark bare masses restored. Another appealing aspect of the quark-gluon plasma is that it should have occurred also at the very first instants of life of the Universe ($\sim 10^{-5}$ s after the Big Bang). Moreover, the astrophysics interest in the QGP extends to the study of neutron stars, where it is believed to exist as well.

Heavy-ion collisions are the best way to artificially recreate the temperature and energy density conditions for the formation of the QGP. The final products of the interactions should carry clear evidence of the phase transition to the QGP. The first Chapter of this thesis summarizes the main predictions of quantum chromodynamics as far as the quark-gluon plasma is concerned. The expected signatures of the creation of the QGP in the final observables of heavy-ion experiments are described, and the most significant results from the recent heavy-ion experiments at the CERN *Super Proton Synchrotron* (SPS) and the at the Brookhaven *Relativistic Heavy-Ion Collider* (RHIC) are reported.

At the CERN *Large Hadron Collider* (LHC), four new experiments are being installed and should begin to take data in late 2007. Three of them, ALICE, ATLAS and CMS, will investigate quantum chromodynamics physics in Pb+Pb collisions at $\sqrt{s_{NN}} = 5.5$ TeV. While ATLAS and CMS will mainly search for (and study) the Higgs and supersymmetric particles, ALICE will concentrate on the possible formation of the quark-gluon plasma in the collisions. Chapter two describes the ALICE experiment. A schematic description of the ALICE detectors is presented, along with some remarks on their performance in terms of particle track reconstruction and particle identification. A particular attention is turned on the *Time Of Flight* (TOF) detector, since the results on its performance which are presented in this Chapter are a fundamental part of the analysis carried out for this thesis.

One of the physics observables ALICE will be interested in is the study of event-by-event (E-by-E) fluctuations of several quantities, such as particle transverse energy, multplicities, and net charge. Chapter three deals with the E-by-E physics in heavy-ion experiments. First, a theoretical overview of event-by-event fluctuations is presented, together with some of the most recent results from the SPS and RHIC experiments. Then, the analysis of charged hadron yields and their transverse momentum spectra on a sample of central Pb+Pb simulated collisions, which has been carried out for this thesis, is described. The ALICE particle identification performance on this sample is illustrated, both for what concerns the individual detectors, and according to a combined particle identification approach. The event-by-event studies on the identified charged particles spectra and ratios are finally reported. Some additional remarks concerning the role of the TOF detector in the analysis are provided.

Finally, this thesis focuses on one of the basic ingredients of every experiment: calibration. Chapter four regards the accurate calibration procedure developed for the ALICE TOF detector since, prior to any physics analysis, the ~ 160000 read-out channels of the TOF system will have to be corrected for time slewing effects and for delays introduced by cable lengths and electronics. A further application of the combinatorial particle identification procedure used for calibration is also described, that is the determination of the time zero of the collision, an essential input for the particle identification algorithm itself.

Some concluding remarks are given at the end.

Chapter 1

Heavy-Ion Physics

The recent development of heavy-ion physics has shed light on new challenging topics in the understanding of ultimate states of matter, such as the quark-gluon plasma, one of the well-estabilshed predictions of quantum chromodynamics. The very high energies available in heavy-ion collisions will make it possible to reproduce the conditions under which the transition from ordinary hadronic matter to the quark-gluon plasma could occur. If such a new phase of strongly interacting matter is created, the final states observed in heavy-ion experiments would manifest it in unordinary behaviours and new features in many physics observables.

In this Chapter, a review of quantum chromodynamics physics will be provided, as well as an overview of the physics observables of interest when dealing with ultrarelativistic heavy-ion experiments in searching for new states of matter.

1.1 QCD Fundamentals

1.1.1 The QCD Phase Diagram

Quantum chromodynamics (QCD) is the theory developed in the early 70s in order to face the compelling challenge of fully describing the interactions between the fundamental constituents of matter, an issue of great interest for particle physics, astrophysics and cosmology: from heavy-ion collision experiments, to the study of the early Universe, to that of neutron stars. QCD is nowadays able to provide a successful picture of the multitude of observed hadrons, as well as to describe the interactions at very high energies of the quarks and gluons they are made up of (and from which the production of particle jets in high-energy collisions originates). Nevertheless, when trying to describe the confinement of quarks and gluons inside hadrons, which is one of the most puzzling features of the strong interaction, then QCD still has some problems: the theory of strong interactions becomes too complicated, and a possible way to approach it is making use of numerical calculations based on a lattice. In particular, according to lattice QCD[1] results [1], for zero net baryon density, QCD matter undergoes a phase transition from a colour-confined hadron gas (HG) to a colour-deconfined quark-gluon plasma (QGP). The difference in the behaviour of strongly interacting matter at high temperatures/densities from what happens at low temperatures/densities is twofold: on one hand, the copious production of resonances in hadronic matter which will occur in a hot interacting gas sets a natural limit to hadronic physics described in terms of hadronic states. On the other, since QCD is an asymptotically free theory, its high temperature/density phases are dominated by its main constituents, the partons (quarks and gluons), which act as degrees of freedom, rather than by hadrons. As a consequence, the non-perturbative features characterizing hadronic physics at low energies, confinement and chiral symmetry breaking, are no more valid when strongly interacting matter is heated up or compressed.

Even if according to recent theories based on thermodynamics it could be straightforward to say that a phase transition from ordinary hadronic matter to a QGP should occur if the temperature/energy density is high enough, the nature of the transition from the low temperature/density hadronic state to the high temperature/density regime strongly depends on the parameters of the QCD Lagrangian, in particular on the number of light or even massless quark flavours. Besides, if considering the quark masses as they show in nature, the physical boundary conditions (i.e. the value of the net baryon number density, or chemical potential μ) play a crucial role. As a consequence, it is fundamental to determine whether the colour-confined hadronic matter turns into a colour-deconfined quark-gluon plasma through either a very phase transition (which could be both of the first and of the second order) or a more or less rapid crossover.

At vanishing or small values of μ, the strange quark mass becomes the control parameter of the transition. In particular, in the limit of light up and down quark masses the transition is first order if the strange mass stays below a certain critical value m^c [2], while above m^c it becomes a continuous crossover. The value of m^c strongly depends on the masses of the light u and d quarks, and it is the value for which the transition is of second order. Figure 1.1 shows how the number of flavours and the values of the quark masses affect the nature of the transition from ordinary matter to QGP. Obviously, the

[1]Lattice QCD (LQCD) is a method for calculating equilibrium properties of strongly interacting systems directly from the QCD Lagrangian by numerical evaluation of the corresponding path integrals, discretizing space and time into $N_\sigma^3 N_\tau$ space-time lattice points.

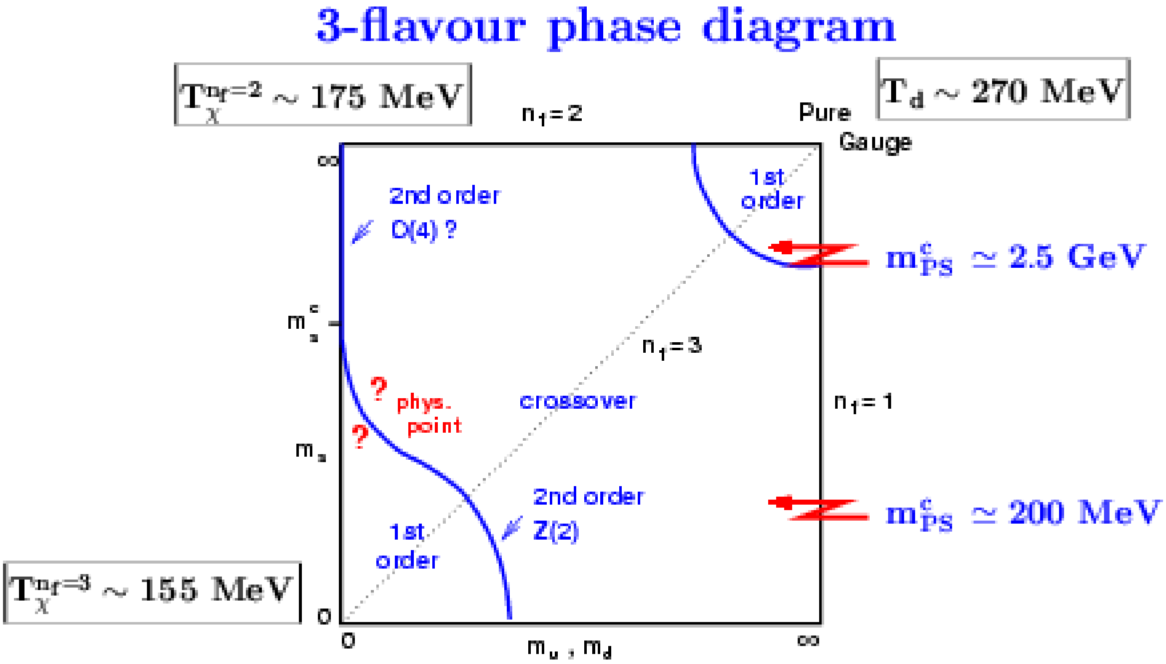

Figure 1.1: The QCD phase diagram of 3-flavour QCD as a function of the quark masses, with degenerate (u, d)-quark masses and a strange quark mass m_s for vanishing chemical potential. Here, n_f refers to the number of degenerate quark flavours. T_d is the temperature at which deconfinement is expected to occur, while T_χ corresponds to chiral symmetry restoration [3]; m^c_{PS} indicates the mass of the pseudo-scalar meson (which is the Goldstone-particle corresponding to the broken chiral symmetry of QCD, the pion), $Z(2)$ corresponds to the global symmetry of the 3-dimensional theory controlling the transition in the light quark regime [4]. To be noted that $Z(2)$ is not a symmetry of the QCD Lagrangian, but takes the place of the axial $U_A(1)$ symmetry at low temperature. O(4) stands for the symmetry (typical of spin models in three dimensions) which is expected to characterize the behaviour of the chiral order parameter (and its derivative) in the $n_f = 2$ region [5]. The question marks emphasize the importance of the location of the physical point in the QCD diagram due to its extreme complexity and richness.

critical values for the temperature and for the masses reported in Fig. 1.1 have to be considered just as indicative. As it can be seen, there is an extended range of quark masses for which the transition to the QGP regime is no more a phase transition but becomes a crossover. The regions of first order transition in the low and in the high quark mass ranges are separated from the crossover region through lines (the *chiral critical lines*) corresponding to second order transitions, where the critical quark mass m^c lies. So far, numerical calculations of m^c have been being carried out [6, 7, 8, 9].

To be noted that the dependence of the QCD phase diagram on the baryon chemical potential is, in fact, a multi-parameter issue, since a chemical potential μ_f should be defined for each quark flavour. The quark number density would then be a function of μ_f.

The QCD phase diagram can also be represented showing T as a function of μ (see Fig. 1.2). Here, the regime of high temperatures and low chemical potential is of great interest especially in experimental particle physics. On the other side of the phase diagram there is the region corresponding to low temperature and high density, extremely important for astrophysical studies. In this regime it is expected that interesting new phases of dense matter exist. At low temperature and asymptotically large baryon number densities asymptotic freedom ensures that the force between quarks will be dominated by one-gluon exchange. As this leads to an attractive force among quarks, it seems unavoidable that the naive perturbation ground state is unstable at large baryon number density and that the formation of a quark-quark condensate leads to a new colour-superconducting phase of cold dense matter (see [10] for a review).

The sketch of the QCD phase diagram in Fig. 1.2 refers to a realistic mass spectrum. Again, different types of transitions can be identified. In particular, the transition to the plasma phase is expected to be a continuous crossover (dashed line) for small values of the quark chemical potential and turns into a first order trasition only beyond a critical value for the chemical potential or baryon number density. The details of this phase diagram, in particular at the low temperature regime are, however, largely unexplored in lattice calculation.

1.1.2 Colour Deconfinement and Chiral Symmetry Restoration

The form of the QCD phase diagram at finite temperature is deeply influenced by the two properties of QCD which also explain the basic features of the obseved hadronic matter, that is to say, confinement and chiral symmetry breaking. The first is responsible for the colourless nature of hadronic spectra, while the second accounts for the presence of light

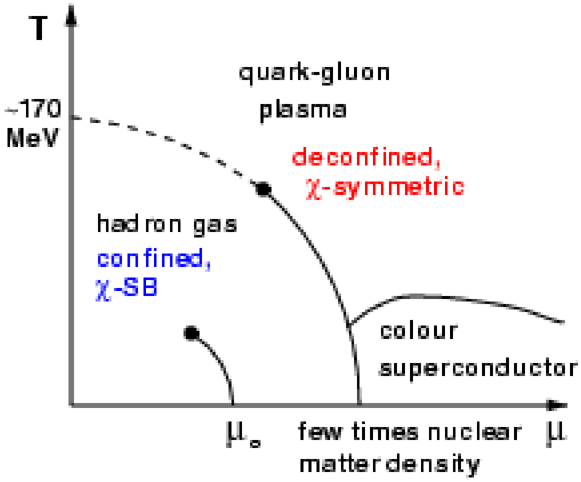

Figure 1.2: The QCD phase diagram in the $T-\mu$ plane as it might look like in the case of non-zero mass but light up and down quarks and a heavier strange quark. In the plot, χ-SB stands for chiral symmetry breaking. The transition to the plasma phase is shown, both in the crossover range, and in the first transition regime. At large baryon number density, the formation of quark-quark condensates (due to the dominating one-gluon exchange in the interactions between quarks) leads to a colour-superconducting phase of cold dense matter. The value μ_0 refers to the transition between a nuclear matter "liquid" and a gas of individual nucleons, ending at a critical point of order 10 MeV, characteristic of the forces which bind nucleons into nuclei. The "few times nuclear matter" corresponds to ~ 1 GeV.

Goldstone particles, the pions.

The most significant evidence of confinement is the long range behaviour of the heavy quark potential, which at zero temperature rises linearly at large distances[2] ($V_{q\bar{q}} \sim \sigma r$, where $\sigma \sim (425 \text{ MeV})^2$ is the quark string tension), and makes quarks and gluons to be confined in a *hadronic bag*. On the other hand, chiral symmetry breaking leads to a non-zero quark-antiquark condensate $\bar{\psi}\psi \simeq (250 \text{ MeV})^2$ (where ψ and $\bar{\psi}$ are the quark and antiquark fields in QCD), which, by the way, vanishes inside the hadron bags. Moreover, at high temperatures, the individual hadronic bags merge to a single one, in which quarks and gluons are able to move freely.

When dealing with lattice QCD, two observables are of particular importance. On

[2]For large distances we mean $r \simeq 1$ fm. At larger distances, the spontaneous creation of quark and anti-quark pairs from the vacuum makes the potential tend to a constant value.

one hand, there is the expectation value $\langle L \rangle$ of the Polyakov loop operator defined as the trace of a path-ordered exponential:

$$L = \frac{1}{3}\mathrm{tr}\left(\mathcal{P}e^{-ig\int_0^{1/T} A_0(\mathrm{x},\tau)d\tau}\right). \tag{1.1}$$

Here, $A_0(\mathrm{x},\tau)$ is the gluon gauge field in the four space-time coordinates (x,τ), which satisfies periodic boundary conditions in the Euclidean time τ with period $1/T$ (being T the temperature of the system), and g is the coupling constant. The Polyakov loop operator characterizes the behaviour of the heavy quark free energy at large distances and it is an order parameter for deconfinement in the $SU(3)$ Gauge theory (valid in the heavy quark mass limit $m_q \to \infty$). In particular, a vanishing value of $\langle L \rangle$ indicates infinite energy for a free quark, i.e. quark confinement. However, as temperature increases, $\langle L \rangle$ increases as well. Then, at a certain critical value T_c its derivative, the Polyakov loop susceptibility χ_L[3], shows a peak and changes sign, which means that quark confinement is broken at T_c (see Fig. 1.3, left).

On the other hand, as already been said, the scalar quark density $\bar{\psi}\psi$ has a nonvanishing expectation value ("chiral condensate") at low temperature, and approaches zero while temperature increases as shown in the right panel of Fig. 1.3. The derivative of $\bar{\psi}\psi$, that is the chiral susceptibility χ_m[4], shows a peak, at the same T_c as $\langle L \rangle$. In the absence of quark masses the QCD Lagrangian is chirally symmetric, i.e. invariant under separate flavour rotations of right-handed and left-handed quarks. Since the up and down masses in the QCD Langrangian ($\mathcal{L}_{\mathrm{QCD}}$) are very small, neglecting them is a good approximation. The nonvanishing chiral condensate at $T = 0$ breaks this chiral symmetry and generates a dynamic mass of order 300 MeV for the quarks; the corresponding "constituent" masses in vacuum are thus about 300 MeV for the up and down quarks, and about 450 MeV for the strange (whose bare mass in $\mathcal{L}_{\mathrm{QCD}}$ is already about 150 MeV). As one can see from the right panel of Fig. 1.3, above T_c the dynamically generated mass melts away, which means that the quarks become light again, and that the chiral symmetry of QCD is restored.

[3]The Polyakov loop susceptibility is defined as:

$$\chi_L = V(\langle L^2 \rangle - \langle L \rangle^2),$$

where V is the volume of the system.

[4]The chiral susceptibility χ_m is defined as:

$$\chi_m = \frac{\partial}{\partial m_q}\langle \bar{\psi}\psi \rangle,$$

where ψ and $\bar{\psi}$ are the quark and antiquark fields, respectively.

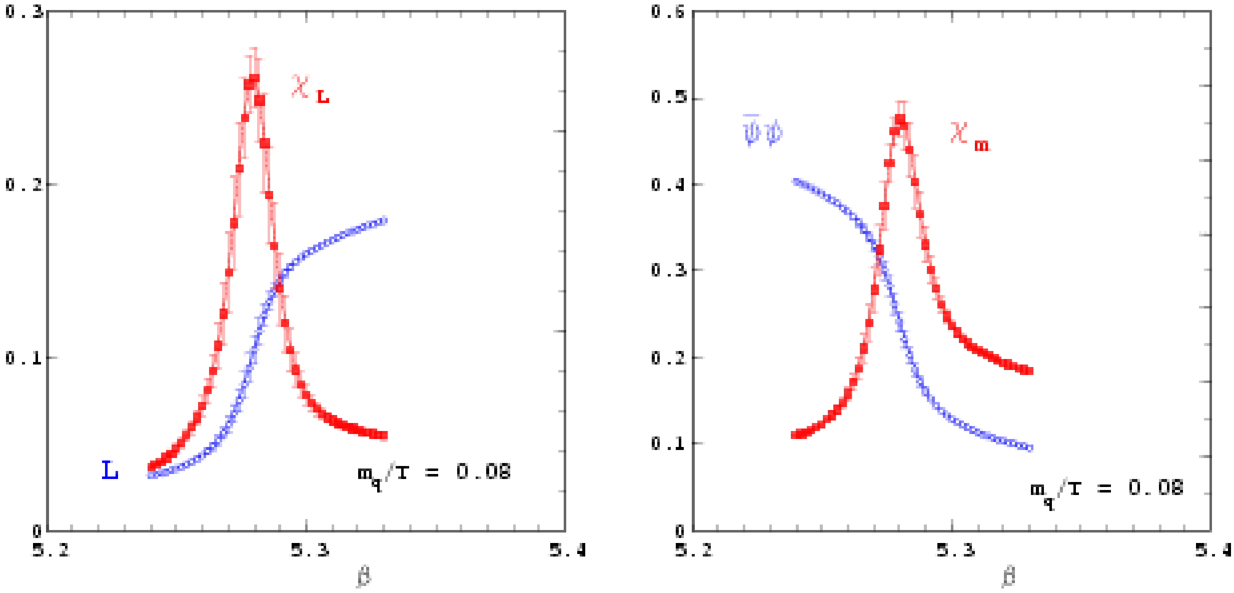

Figure 1.3: Left: Polyakov loop expectation value $\langle L \rangle$ and its temperature derivative (Polyakov loop susceptibility χ_L) as a function of the lattice coupling $\beta = 6/g^2$ which is monotonically related to the temperature T (larger β correspond to larger T). Right: The chiral condensate $\langle \bar{\psi}\psi \rangle$ and the negative of its temperature derivative (chiral susceptibility χ_m as a function of temperature. (From [11].)

Moreover, as can be seen from Fig. 1.3, deconfinement and chiral symmetry restoration occur at the same critical value of the temperature T_c which is a result valid in all lattice QCD calculations made starting form different values for the quark masses, and then extrapolating to zero. As a matter of fact, the transition from the low temperature hadronic phase to the QGP phase which occurs just at T_c, is characterized by sudden changes in the non-perturbative vacuum structure, like a sudden decrease of the chiral condensate, as well as a drastic change of the heavy-quark free energy (heavy-quark potential). This characterizes the QCD transition as chiral-symmetry restoring and deconfinig at the same time.

Both deconfinement and chiral symmetry restoration strongly affect the intermedium properties of both light- and heavy-quark bound states. Deconfinement is responsible for a greater quantity of gluons which can produce extra quark-antiquark pairs, leading to an equilibrium state of quarks, antiquarks and gluons. At the same time, the melting of the quark masses at high temperature (above T_c) reduces the threshold for a quark-antiquark pair formation. This is particularly important for the strange quarks, which have a constituent mass well above T_c, but a current mass comparable with the critical temperature. As a consequence, during a heavy-ion collision in which T_c is reached and even exceeded, thermal processes are likely to balance strange and anti-strange abundances.

The heavy-quark free energy shows a temperature dependence for $T > 0.6\ T_c$: while the temperature increases, it becomes easier to separate heavy quarks at infinite distance. For example, already at $T \simeq 0.9\ T_c$, the free energy difference for a heavy quark pair separated by a distance similar to the J/ψ radius (i.e. ~ 0.2 fm) and a pair separated to inifinity is only 500 MeV, which is compatible with the average thermal energy of a gluon. As a consequence, the bound $c\bar{c}$ states are expected to disappear at high temperature. With respect to this, detailed studies on the spectral functions of $c\bar{c}$ bound states such as the J/ψ and the χ_c have been and have to be carried out. The same holds true for the light-meson spectra since, as a consequence of chiral symmetry restoration, hadronic correlation functions constructed from light quark flavours show a drastically different behaviour below and above T_c.

1.1.3 The Equation of State

One of the main goals of QCD is the calculation of the basic thermodynamics quantities and their temperature dependence, in particular the pressure p and the energy density ε, fundamental when dealing with highly dense matter, and when discussing different computational schemes, such as lattice calculations and analytic approaches in the continuum.

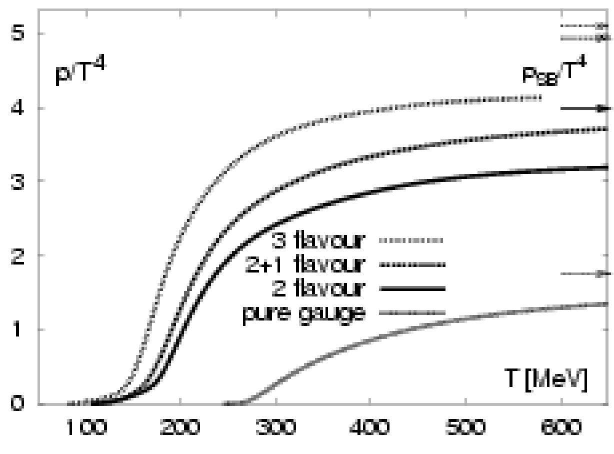

Figure 1.4: The pressure in QCD with two and three degenerate quarks flavours as well as with two light quarks and a heavier (strange) one [12].

At high temperature, because of asymptotic freedom, these observables would be expected to show ideal gas behaviour, being directly proportional to the basic degrees of freedom contributing to the thermodynamic properties of the plasma. For example, the asymptotic behaviour of the pressure p would be given by the Stefan-Boltzmann law

$$\lim_{T\to\infty}\frac{p}{T^4} = (16 + 10.5n_f)\frac{\pi^2}{90}, \tag{1.2}$$

where n_f is the number of quark flavours. However, perturbative calculations fail to serve the purpose of studying bulk thermodynamics when deviating from this ideal gas behaviour, and in this case lattice calculations are used, starting from the basic relations:

$$\frac{p}{T^4} = \frac{1}{VT^3}\ln Z(T,V,\mu_f), \tag{1.3}$$

$$\frac{\varepsilon - 3p}{T^4} = T\frac{\mathrm{d}}{\mathrm{d}T}\left(\frac{p}{T^4}\right)\Big|_{fixed\,\mu/T}. \tag{1.4}$$

Here $Z(T, V, \mu_f)$ is the grand canonical partition function (suitable for elementary particles interacting only through the strong force), T is the temperature, V is the volume, and μ_f is a set of chemical potentials ($f = 1, ..., n_f$ different quark flavours). Figure 1.4 shows the results obtained in calculations with different numbers of flavours [12]. As one can see, at high temperatures the value of p/T^4 depends on the number of degrees of freedom, even if when rescaling the pressure by the correspondent ideal gas value, a common pattern of the dependence of p from T shows up. Nonetheless from Fig. 1.4 it is possible to infer that the transition region shifts to smaller temperatures as the number of quark flavours increases.

Figure 1.5 shows the results of lattice calculations for the energy density (see Eq. 1.4). For a massless gas of quarks and gluons the energy density is proportional to T^4, and the proportionality constant strongly depends on the number of massless degrees of freedom. For $T < 4T_c$ the lattice data remain about 20% below the Stefan-Boltzmann limit indicated by the arrow in the upper-right corner of Fig. 1.5, left. Near T_c the ratio ε/T^4 drops rapidly by more than a factor 10, as a consequence of hadronization. According to Fig. 1.5 the critical energy density for deconfinement is about $0.6 - 0.7$ GeV/fm^3. In fact, ε_c could be rather different from this value (ranging from ~ 1 GeV/fm^3 to 500 MeV/fm^3) as a consequence of the 15 MeV of uncertainty on the determination of T_c. Anyway, an easy value to handle and to quote is $\varepsilon = 1$ GeV/fm^3 since it corresponds to the density in the centre of a proton.

The right panel of Fig. 1.5 is meant to stress the importance of the factor T^4 in terms of energy density. For example, to reach even only $2T_c$ in order to approach the edge of the transition region, energy densities $\varepsilon \simeq 23$ GeV/fm^3, that is to say ~ 40 times the

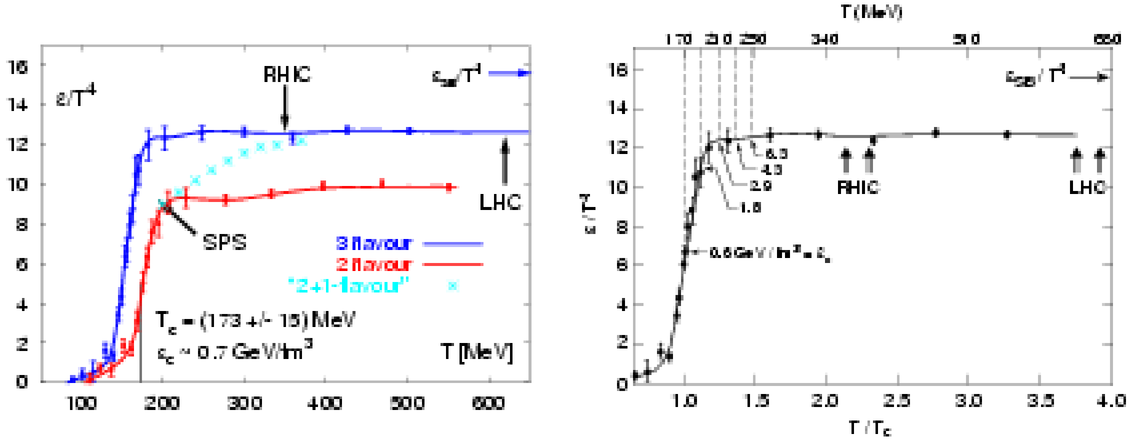

Figure 1.5: Left: Energy density in units of T^4 for QCD with two and three degenerate quark flavours. The curves labelled "2 flavour" and "3 flavour" were calculated for two and three light quark flavours of mass $\frac{m_q}{T} = 0.4$, respectively; "2+1 flavour" indicates a calculation for two light and one heavier strange quark flavours of mass $\frac{m_q}{T} = 1$. In this case the ratio ε/T^4 interpolates between the two light flavours at $T \lesssim T_c$ and three light flavours at $T \gtrsim 2T_c$. For 2 and 2+1 flavours the critical temperature is $T_c = 173 \pm 15$ MeV (see [1]). Right: Absolute values for the energy density ε at several temperatures for the 3-flavour case. ε_{SB} refers to the Stefan-Boltzmann asymptotic behaviour of the pressure.

critical one ε_c, are required. Such energies have been achieved for example during the last few years at the Relativistic Heavy Ion Collider (RHIC) at BNL in Au+Au collisions at $\sqrt{s_{NN}} = 130$ GeV. The Large Hadron Collider (LHC) at CERN will be able to reach even higher energy densities, of the order of ~ 500 GeV/fm^3, near the right edge of Fig. 1.5.

1.2 QCD Matter and Relativistic Heavy-Ion Collisions

As already said, the interest in heavy-ion collision experiments as the best test-bed for the predictions of QCD is manyfold. On one hand, they offer the oppportunity to study the phase transition from ordinary hadronic matter to a plasma of quarks and gluons (QGP), as it is expected to occur under extreme conditions of temperature and energy density, and to investigate the main properties of the QGP itself (see Sec. 1.1.1 and Sec. 1.1.2). On the other hand, cosmological and astrophysical implications are involved, since the phase transition mentioned above is believed to have happened in the first stage of the evolution of the Universe (during the first 10^{-5} seconds after the Big Bang) and it may even happen in the core of neutron stars.

Anyway, the system created in a heavy-ion collision is very different both from that predicted by the calculations of lattice QCD, and from the status of the early Universe, as well as from what exhists inside neutron stars. The small size of the available nuclei sets the scale for the temporal and spacial extent of the system created in the collision. The asymmetry of the incoming system, with its momentum in the direction of the incoming beams, is reflected in the evolution of the system. What remains is just a bulk of hadronic and leptonic residues.

The main experimental and theoretical goal is then to reconstruct the properties of the earlier stages of the system from the experimental observables related to the products of the collision. For example, leptonic probes, $\gamma, e^+e^-, \mu^+\mu^-$, carry information concerning the chromoelectric field fluctuations in the QGP. The very abundant hadronic probes, such as π, p, $\bar{\text{p}}$, K, Λ..., are useful to study the chemical composition of the QGP. Furthermore, decays such as $\rho \to e^+e^-$ should carry indirect information related to the chiral symmetry restoration.

1.2.1 Evolution of a Heavy-Ion Collision

The Early Stage of the Collision

The development of heavy-ion collisions can be schematically divided into three main phases: thermalization, expansion, and decoupling. Before thermalization begins, that is to say, before the QGP forms, hard particles with either a large mass or large transverse momenta $p_t \gg 1$ GeV/c are produced. Since their creation involves large momentum transfers (of the order of $Q^2 \sim p_t^2 \gg 1$ GeV^2), it can be studied with perturbative QCD. Even if hard particles are a product of the very first instants after the collisions, when the collision energy is high enough (at RHIC, for example) high-p_t jets may be produced from the fragmentation of hard partons. These are then useful in order to probe the soft matter created by the bulk of soft particles [13].

During the first stages of the collision, direct photons are produced as well [14] by the electric charges in the medium (i.e. quarks and antiquarks). They can be either real or virtual, and in this latter case, they then materialize in lepton-antilepton pairs, called dileptons. Direct photons are then important because, as they can escape from the interaction region without rescattering, they carry signatures of the initial phase of the collision, in particular of the momentum distributions of their parent quarks and antiquarks. The spectra of direct photons and dileptons are affected by a very large background of indirect photons and from a combinatorial background of uncorrelated lepton-antilepton pairs.

Thermalization and Expansion

One of the main characteristics of nucleus-nucleus collisions, which distinguishes them from nucleon-nucleon collisions, is the fact that the quanta produced in the primary collisions do not escape from the medium formed but rescatter with each other. In this way, the highly dense plasma of quarks and gluons referred to as QGP generates as the result of the thermalization process which the strongly interacting matter coming from the collision undergoes.

The produced partons rescatter both elastically and inelastically, equipartitioning the deposited energy. Inelastic processes, however, are also responsible for the relative abundances of gluons, and of light and strange quarks. Even if strange quarks are not present at the initial stage of nucleon-nucleon collisions and their constituent mass ($\sim$ 450 MeV) makes it difficult to produce them during hadronization, in heavy-ion collisions strangeness suppression should be reduced or even completely absent because in these collisions it is possible to reach an energy density so high that deconfinement and chiral symmetry restoration occur, and the strange quarks become much lighter ($m_s \sim 150$ MeV, see Sec. 1.1.2).

A thermalized system has an internal pressure which, acting against the surrounding vacuum, leads to a collective expansion of the fireball. As a consenquence, while the fireball expands, both the temperature of the system and the energy density decrease. When reaching $\varepsilon_c \sim 1$ GeV/fm^3 (see Sec. 1.1.3), hadronization begins. The energy density drops steeply over a small temperature interval. At the same time, since entropy can not decrease, the volume of the fireball increases by a large factor as temperature stays almost at the same value T_c for quite a long time interval. Moreover, during hadronization the sound velocity stays small ($c_s = \sqrt{\partial p/\partial \varepsilon}$) and the collective flow[5] does not increase. The direct photon spectrum and the centre-of-mass energy dependence of the collective flow would then be affected by the consequent softness of the equation of state.

[5]The collective flow is an unavoidable consequence of quark-gluon plasma formation in heavy-ion collisions. Since a quark-gluon plasma is by definition an (approximately) thermalized system of quarks and gluons, it has thermal pressure, and the pressure gradients with respect to the surrounding vacuum causes the quark-gluon plasma to collectively expand, originating the collective flow.

Chemical and Thermal Freeze-out

After hadronization, hadrons go on rescattering with each other, continuing building up expansion flow. The chemical composition of the hadronic system changes, i.e. the identity of the hadrons changes, till the rates for inelastic scatterings become too small to allow further expansion. At this point the so-called *chemical freeze-out* occurs. Then, when the distances among hadrons become larger than the range of strong interactions, elastic processes stop as well, and the *thermal* or *kinetic freeze-out* takes place. This happens later than the ceasing of inelastic processes, since the inelastic cross section is only a small fraction of the total one.

To be noted that resonant processes such as $\pi + N \rightarrow \Delta \rightarrow \pi + N$ contribute to the elastic cross section since in the end they do not change the chemical composition of the system.

At kinetic freeze-out, all hadron transverse momentum spectra show an approximately exponential shape, reflecting the temperature of the fireball at that point, which is blueshifted by the average transverse flow[6]. In order to well understand the measured stable particle spectra, the products of the decays of unstable resonances have to be taken into account, especially in the case of pions at low p_t.

1.3 QGP Signatures

If after a heavy-ion collision one could see free quarks and gluons, then it would be straightforward to prove whether a QGP had formed or not. Since, in fact, this cannot happen, and the only remnants of such a collision are colour neutral composite many-body systems, i.e. hadrons, then the only possible approach to a study of the QGP and its features is indirect, via the measurement of several suitable observables. The strategy should consist in a systematic variation of an external parameter (such as the centrality[7] of the collision and the beam energy) with the consequent measurement of excitation functions of several signals which in the case of a phase transition show *simultaneously*

[6] In a heavy-ion collision, the transverse flow is the component of the flow velocity in the plane perpendicular to the beam axis.

[7] In high-energy physics experiments, the centrality of a collision is determined by the distance between the centers of the two colliding nuclei (i.e. the impact parameter) in such a way that the smaller the impact parameter, the more central the collision. As a consequence, centrality is strongly related to the geometry of the collision, and in particular to the number of participating nucleons. Moreover, since the inelastic cross-section $\sigma^{\rm inel}_{\rm A+A}$ is a function of the impact parameter [15], the centrality is often defined in terms of percentage of $\sigma^{\rm inel}_{\rm A+A}$.

an anomalous behaviour.

Obviously, one serious problem in trying to investigate the properties of the quark-gluon plasma in a laboratory is the very limited lifetime of the plasma that would be possibly created, at most a few fermi in diameter and perhaps 5 fm/c in duration. Furthermore, the signals from the QGP would be screened by the backgrounds coming from the hot hadronic gas phase that follows hadronization, and would be significantly modified by the interactions occuring later in the hadronic phase. Nevertheless, some physical observables have been identified as appealing and promising signatures of the quark-gluon plasma.

1.3.1 Kinematic Probes

Kinematic probes are aimed at the investigation of the energy density ε, the pressure p, and entropy density s dependence on temperature T for a highly dense hadronic system. Measurable observables that are related to T, s and ε are the average transverse momentum $\langle p_T \rangle$, the hadron rapidity distribution, dN/dy[8] and the transverse energy dE_T/dy[9] respectively [16]. For example, it has been suggested that the equation of state, which gives ε as a function of T, can be probed experimentally plotting the average transverse momentum $\langle p_T \rangle$ vs. the particle density dN/dy or the transverse energy density dE_T/dy. If a phase transition occurs (i.e. a rapid change in the number of degrees of freedom) one expects a monotonously rising curve interrupted by a plateau, which would be caused by the saturation of $\langle p_T \rangle$ during the mixed phase (QGP + hadronic phases). After the transition, the mean transverse momentum rises again, although according to detailed hydrodynamical studies the plateau is washed out due to collective flow [17, 18].

[8] Being E and p_z the particle energy and momentum component along the z axis (usually the beam direction), then rapidity y is defined as:

$$y = \frac{1}{2}\ln\left(\frac{E + p_z}{E - p_z}\right).$$

To be noted that if $p \gg m$ (where p and m are the momentum and the mass of the particle), the rapidity coincides with the pseudorapidity $\eta = -\ln\tan\theta/2$ (where $\cos\theta = p/p_z$).

[9] The transverse energy E_T is defined as:

$$E_T = E\sin\theta,$$

where E is the energy of the particle, and θ is the angle between the particle trajectory and the beam axis.

Particle Spectra

Collective (transverse) flow, feeding from resonance decays, strongly influences the shape of particle spectra, which can be seen in a shoulder-arm shape of the transverse momentum spectra [19]. A useful and practical parameter to study is the transverse mass ($m_T = \sqrt{m^2 + p_T^2}$, where p_T is the transverse momentum of the particle), which reflects the transverse flow created after the impact between the two nuclei. We could say that if rescattering among the fireball constituents results in thermalization and collective flow, and if all the hadrons decouple (i.e. stop interacting) simultaneously, the shape of all hadrons m_T spectra are characterized by only two parameters, the freeze-out temperature T_f and the mean transverse flow velocity $\langle v_T \rangle$ at freeze-out.

In the relativistic region ($m_T \gg m$), it has been found that all hadron spectra follow the same exponential ("m_T scaling effect"), that is $dN/(m_T dm_T dy) \sim m_T^{1/2} e^{-m_T/T}$, from which the fireball temperature T can be directly extracted. Moreover, the effect of the flow on the spectra in this p_T regime can be expressed by the formula:

$$T \approx T_f \sqrt{\frac{1 + v_T}{1 - v_T}}. \tag{1.5}$$

where T is the inverse slope of the particle spectra. While at large values of m_T the spectra of all hadrons should have the same inverse slope T, in the non-relativistic region where $m_T \ll m$, the particle mass becomes a crucial parameter and the relation

$$T \approx T_f + \frac{1}{2} m \langle v_T \rangle^2 \tag{1.6}$$

holds true. Figure 1.6 shows the collective flow contribution contained in the spectra, which results, for example, in an inverse slope for protons of ~ 300 MeV. From Fig. 1.6 (see also Eq. 1.5 and Eq. 1.6) it is also possible to infer that an accurate determination of $\langle v_T \rangle$ can not be obtained simply from the distribution of T. Actually, the transverse flow velocity affects other observables, such as quantum statistical Bose-Einstein correlations (Hanbury Brown-Twiss, HBT) between identical bosons which have to be studied.

Usually, a simple exponential approximation of the spectra is chosen to parametrize the experimental data concerning hadron transverse mass distributions:

$$\left. \frac{dN}{m_T dm_T dy} \right|_{y=0} = C exp\left(-\frac{m_T}{T}\right). \tag{1.7}$$

Figure 1.7 shows the transverse mass distributions obtained for charged hadrons by the PHENIX experiment at RHIC [21].

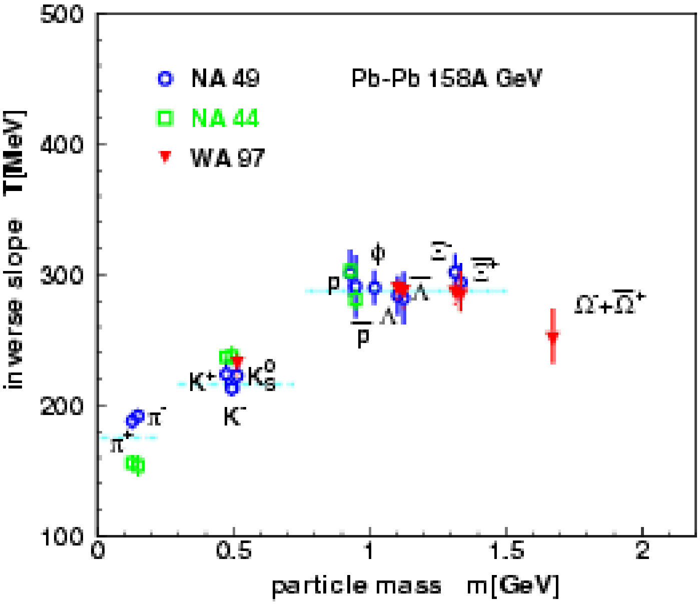

Figure 1.6: Inverse slopes T of the measured m_T–distributions from 158 $AGeV/c$ Pb+Pb collisions for various hadron species, plotted as a function of the rest mass [20]. Results from different experiments are labelled by different symbols. The lines are to guide the eye.

The ρ Particle and the Lepton Pairs

Information concerning the stages between immediately after the collision, and just before hadron decoupling can be obtained studying the ρ meson. The ρ decays in dilepton pairs (e^+e^- or $\mu^+\mu^-$) which escape from the fireball without interacting again. But after a first generation of ρ particles has decayed, a second generation is produced by $\pi\pi$ resonant scattering. This second ρ flush decays, in turn, into lepton pairs. As a consequence, the measure of the number of extra dileptons with the invariant mass of the ρ meson can be considered as a first, fast measure of the fireball lifetime.

Moreover, lepton pairs from hadronic sources in the invariant mass range between 0.5 and 1 GeV are important signals of the very highly dense medium which is formed during the collision. They provide important information on possible medium modifications of hadronic properties, such as a broadening of the ρ peak in the e^+e^- spectrum. This should be due to the fact that pions not only strongly rescatter among each other, but also with the baryons in the hadronic resonance gas, and this modifies their spectral densities, and smears the ρ resonance in the $\pi\pi$ scattering cross section. The intense rescattering of pions (which are the most abundant particle specie in the hadron gas)

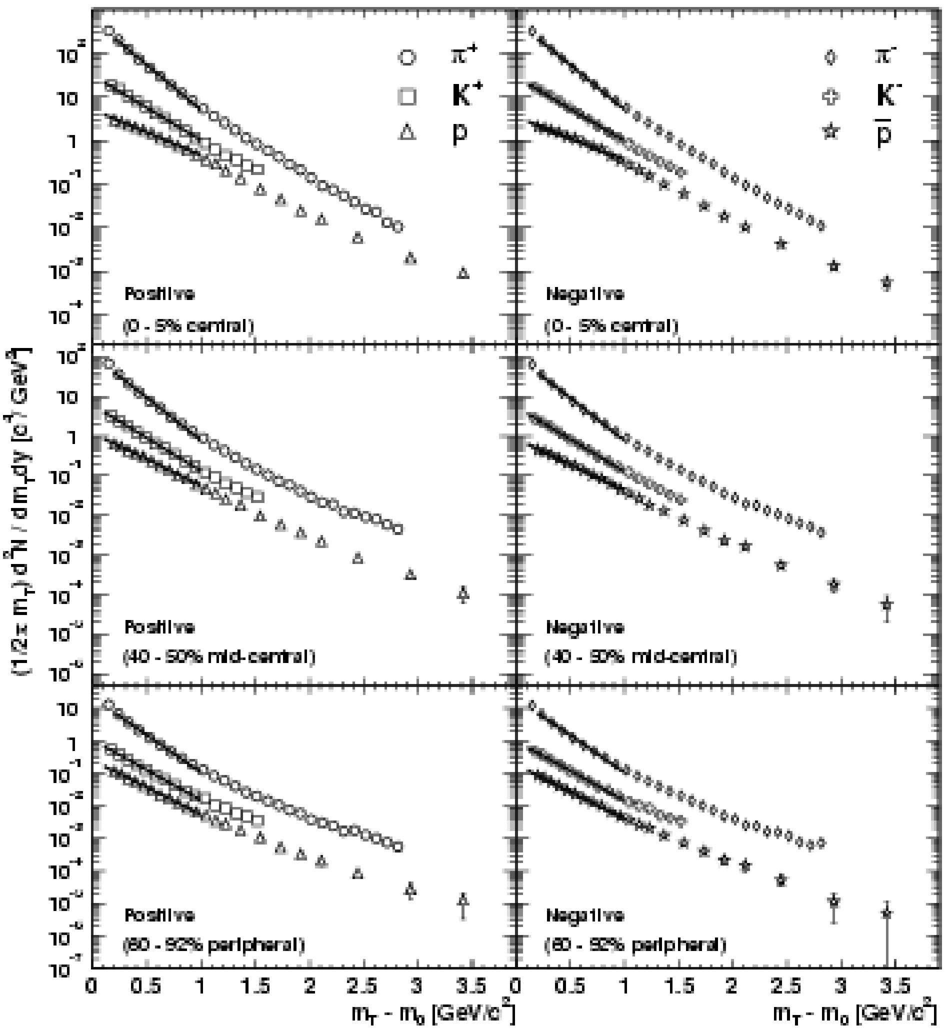

Figure 1.7: Transverse mass (minus the rest mass) distributions for $\pi^{\pm}$, $K^{\pm}$, p, $\bar{p}$, for different centralities in Au+Au collisions at $\sqrt{s_{NN}}$ = 200 GeV obtained from the PHENIX experiment. See [21] for details.

allows the fireball to reach and almost maintain a local thermal equilibrium, to build up thermodynamic pressure, and to collectively explode. The outnumbering of the dileptons from the "broadened" ρ with respect to those from the "unmodified" ρ emitted at thermal freeze-out (which should show up as a normal ρ peak) would indicate that the hadronic rescattering stage has lasted several ρ lifetimes.

Direct Photons

Heavy-ion collisions are characterized by a large amount of direct (thermal) photons produced, coming from various processes, the most important of which are $q\bar{q} \to \gamma g$ (annihilation) and $gq \to \gamma q$ (Compton scattering). Moreover, other processes contribute

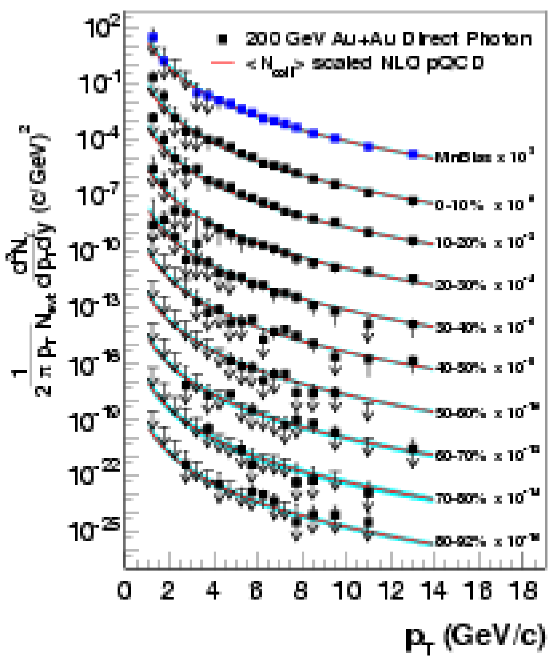

Figure 1.8: Direct photon invariant yields as a function of transverse momentum for nine different centrality selections and minimum bias Au+Au collisions at $\sqrt{s_{NN}} = 200$ GeV. See [29] for more details.

to the observed rate of direct photons, such as initial state momentum broadening of the incoming partons (the Cronin effect), additional fragmentation contributions [22, 23] or additional scatterings in the thermalized matter of the final state. Measurements of direct photon production allow a more definite discrimination between initial and final state suppression of high-p_T hadrons due to the fact that photons, once produced, are essentially unaffected by the surrounding matter. Hence, photons produced directly in initial parton scatterings will not be quenched unless the initial parton distributions themselves are suppressed in the nucleus.

Besides, the production rate of thermal photons and their momentum distribution are strongly affected by the momentum distribuitions of quarks, antiquarks, and gluons in the plasma. As a consequence, the photons may carry information in the thermodynamic state of the plasma at the moment of their creation.

The main hadronic background processes which can interfere with the detection of direct photons are [24, 25] pion annihilation $\pi\pi \rightarrow \gamma g$, dominant during the plasma phase, and Compton scattering $\pi\rho \rightarrow \gamma\pi$, which mostly occur during the thermal hadron gas phase and to which the broad a_1 resonance may be an important contribution.

Even if screening effects are responsible for photon spectra of almost equal intensity and shape at T_c for both the hadronic phase and the QGP phase, a clear signal of photons from the quark-gluon plasma could be visible for transverse momenta p_T in the range $2 \div 5$ GeV/c if a very hot plasma is formed [26, 27]. Separate contributions from the different stages of the system evolution are difficult to distinguish because of transverse flow effects, which, however, are important up to momenta ~ 5 GeV.

Figure 1.8 shows the direct photon momentum distribution as measured from the data taken by the PHENIX experiment [28] during the second RHIC run for Au+Au collisions at $\sqrt{s_{NN}} = 200$ GeV. The perturbative QCD (pQCD) lines reported are described in [29].

1.3.2 Probes of Deconfinement

Heavy-ion collisions are drastically different from nucleon-nucleon collisions. One of the main features which distinguishes the two classes of phenomena is, as already said, the formation of a quark-gluon plasma, expected in the case of heavy-ion physics but not for nucleon-nucleon collisions. When dealing with heavy ion experiments, it is thus important to identify the observables which can be considered as QGP signatures.

Strangeness enhancement

Strangeness enhancement is one of the earliest predicted QGP signatures [30], and it can be studied through the production of strange particles such as $\phi(s\bar{s})$, $\mathrm{K}(u\bar{s})$, $\Lambda(uds)$. Figure 1.9 shows the K/π ratio as obtained by the STAR experiment at RHIC as a function of collision energy compared with p+p data from [31] and p+$\bar{\mathrm{p}}$ from [32]. On one hand, colour deconfinement leads to a large gluon density which can create $s\bar{s}$ pairs by gluon fusion. On the other, chiral symmetry restoration makes the strange mass relatively light (see Sec. 1.1.2), thus reducing the production threshold. These effects result in a significant reduction for strangeness saturation and chemical equilibration, compared to hadronic rescattering processes after hadronization where the production of strange hadron pairs with opposite strangeness is suppressed by large thresholds and small cross sections. Another remarkable feature is that in a baryon rich environment as that created in heavy-ion collisions, the baryon stopping is large. As a matter of fact, if the hadronic

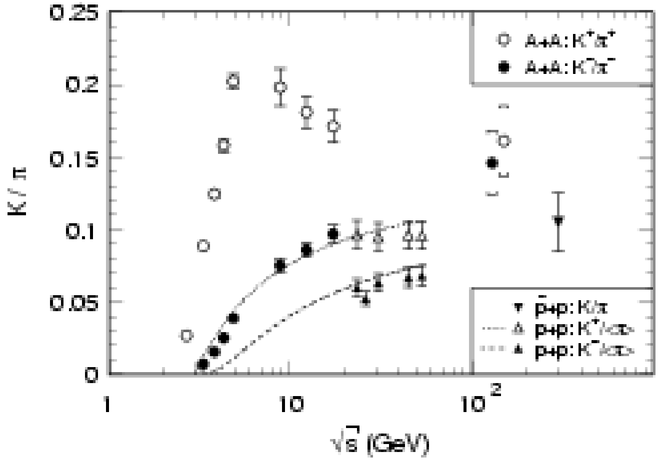

Figure 1.9: Mid-rapidity K/π ratios vs. $\sqrt{s_{NN}}$. The curves refer to p+p data [31]. See [33] for more details.

matter is deconfined during the collision, the volume of the central fireball will be already occupied by many u and d quarks coming from the interacting nuclei. As a consequence, while the production of u and d is suppressed because of Pauli blocking, the production of s will be relatevely enhanced.

Multistrange particles are abundantly produced in heavy-ion collisions during the QGP hadronization phase [34]. As a consequence, after the gluon fusion process $gg \to s\bar{s}$, quark recombination leads to the emergence of particles such as $\Xi(sqq)$ and $\bar{\Omega}(\bar{s}\bar{s}\bar{s})$ which otherwise would be very difficultly produced. Enhancement of these particles can be then considered a QGP signature. Figure 1.10 shows the rise of the enhancement with strange content, with the p+Be reaction system taken as reference. The results are presented as yields per participant, where a participant is an inelastically reacting wounded nucleon. Fig. 1.10 confirms the QGP prediction of an enhancement growth with strangeness (left) and antiquark content (right) [35].

Charmonium and Open Charm Production

Charmonium production in hadronic processes [36] and nuclear [37] collisions is usually described as made up of three different stages: the creation of a $c\bar{c}$ pair, the formation of a bound $c\bar{c}$ state, and its subsequent interaction with the surrounding medium. The last process is responsible for the suppression of the finally observed bound $c\bar{c}$ states with respect to the initially created number, which is proportional to the number of Drell-Yan

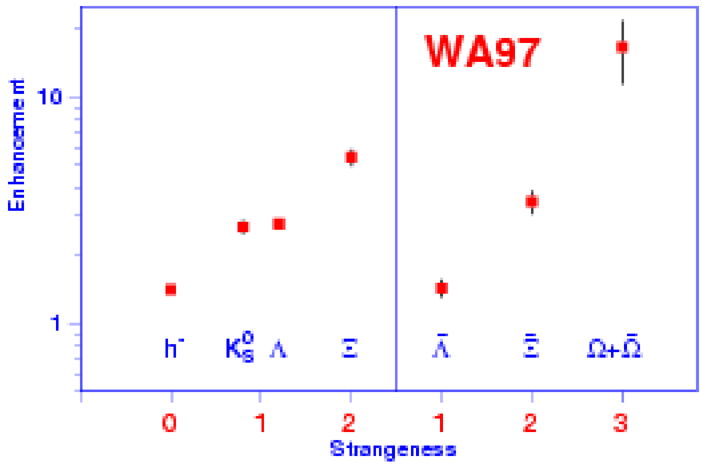

Figure 1.10: Strangeness abundance enhancement in Pb+Pb collisions at $\sqrt{s_{NN}} = 158$ GeV with respect to the yield in p+Be collisions, scaled with the number of wounded nucleons [35].

lepton pairs. The entity of the suppression in nuclear collisions can probe the formation of a highly dense intermediate medium, and the rapid increase of the suppression when going from peripheral to central collisions is often attributed to a QGP state as well [38].

Charmonium suppression is expected because the highly dense gluon system resulting from deconfinement. This should Debye-screen the colour interaction potential between a $c\bar{c}$ quark pair produced during the initial impact of the two nuclei and thus prevent the quarks from binding into a charmonium state (J/ψ, χ_c, ψ'). To be noted that the first states to be suppressed while increasing the energy achieved are the losely bound ψ' and χ_c, followed by the strongly bound J/ψ.

Owing to its finite size, the formation of a $c\bar{c}$ bound state requires a time of the order of 1 fm/c [39], after which the J/ψ may still survive, if it escapes from the region of high density and temperature before the $c\bar{c}$ pair has been separated by more than the size of the bound state [13]. This could happen if the quark-gluon plasma cools very fast, or if the J/ψ momentum is sufficiently high.

Moreover, J/ψ suppression could be due also to collisions with comoving hadrons, after which a D-meson pair[10] should be created, and other contributions may come from nuclear shadowing of soft gluons, initial state scatterings of partons resulting in a widened

[10] The D meson multiplicity is determined by the number of $c\bar{c}$ quarks in the early parton stage before hadronization. As a result, the production of open charm is carried mainly by the D meson in the final state.

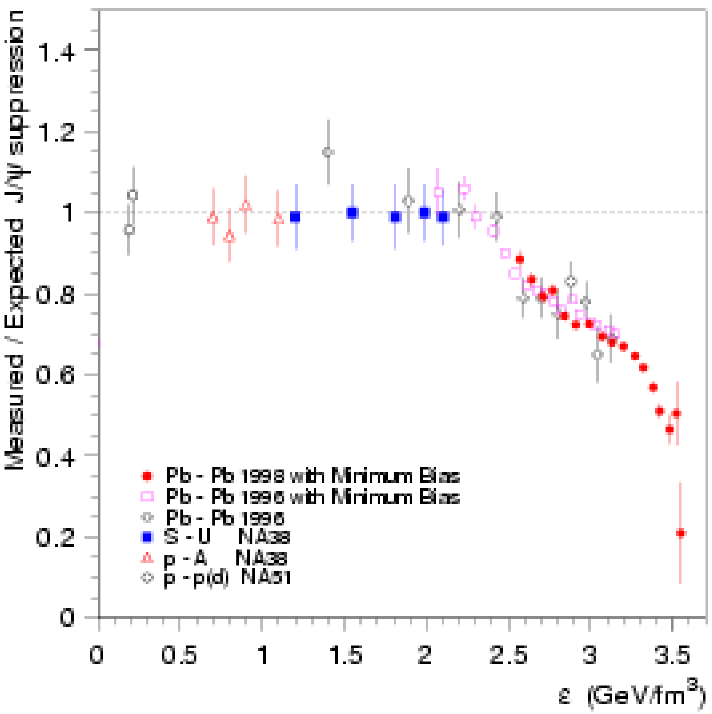

Figure 1.11: The anomalous J/ψ suppression as a function of the energy density reached in the heavy-ion collision. Suppression is obtained from the measured cross sections divided by the values expected from nuclear absorpion. The latter are deduced from a fit to measurements on interactions of incident protons with various targets (open circles and triangles) and on sulfur-uranium collisions (closed black squares). As can be seen from the figure, in lead-lead interactions J/ψ is suppressed normally, i.e. according to pure nuclear absorption, for energy densities lower than 2.2 GeV/fm^3. For higher density values, a peculiar abnormal suppression pattern is observed, as can be expected from charmonium melting due to deconfinement.

transverse momentum distribution, and final state absorption on nucleons [40].

Figure 1.11 shows the experimentl results concerning the predicted J/ψ suppression obtained from Pb+Pb collisions by the NA50 experiment, as well as those from NA38 with lighter incident ions. From Fig. 1.11 it is possible to infer that a new physical process should happen for energy densities above 2.2 GeV/fm^3. Besides, the higher the energy density, the more the J/ψ production rate differs from the nuclear absorption regime.

However, some models predict that at energies as high as those now available at RHIC (and in a near future at LHC), an enhancement of heavy quarkonia should occur as a consequence of $c\bar{c}$ coalescence in the quark-gluon plasma [41], as well as to a detailed balance of $D + \bar{D} \leftrightarrow J/\psi + X$ [42] and/or statistical J/ψ production [43]. In addition, initial state effects of shadowing and possible parton saturation may play an important role in charm production.

1.3.3 Jet Tomography

One of the main consequences of the interaction between high momentum partons and the extremely dense intermedium created early in a heavy-ion collision is the modification of the yield and momentum distribution of the particles themselves. This effect, which results from the induced radiative energy loss, is one of the most important results obtained at RHIC for the production of particles with p_T up to 10 GeV, which falls very near the expectations of binary scaling relative to nucleon-nucleon collisions. Figures 1.12 and 1.13 show, as a function of the transverse momentum, and for charged hadrons, the nuclear modification factor R_{AA} as measured at RHIC, defined as a collision-number-scaled ratio between $A + A$ and p+p collisions scaled by the number of binary collisions N_{bin}:

$$R_{AA} = \frac{[yield]^{AA}}{N_{bin} \times [yield]^{pp}}. \tag{1.8}$$

In other words, a R_{AA} of the order of unity would imply that particle production from $A + A$ collisions is equivalent to a superposition of indipendent nucleon-nucleon collisions. In Fig. 1.13, R_{AB} refers to same as R_{AA}, with the specification that the two colliding nuclei may be different.

Since energy loss in a hot and dense medium through gluon bremsstrahlung is expected to be larger in a system of deconfined colour charges than in hadronic matter, this is considered an effective signature of the formation of a quark-gluon plasma. The jets of hadrons which should result from the hard scattering of partons (as it is found in p+p collisions) during the earliest time of the collision, are then quenched with a correspondent depletion of the particle yields. This effect is referred to as "jet quenching".

Studies of the angular correlation of high-p_T particles, with respect to a high-p_T trigger particle selected in each event, have been carried out by the STAR experiment at RHIC [45], as shown in Fig. 1.14. For p+p and d+Au collisions, these studies show the characteristic near-side and back-to-back correlation of high-p_T particle jets. On the contrary, when looking at Au+Au collisions, while the near-side correlation still remains, the back-to-back is almost completely suppressed. As said before, jet quenching is due

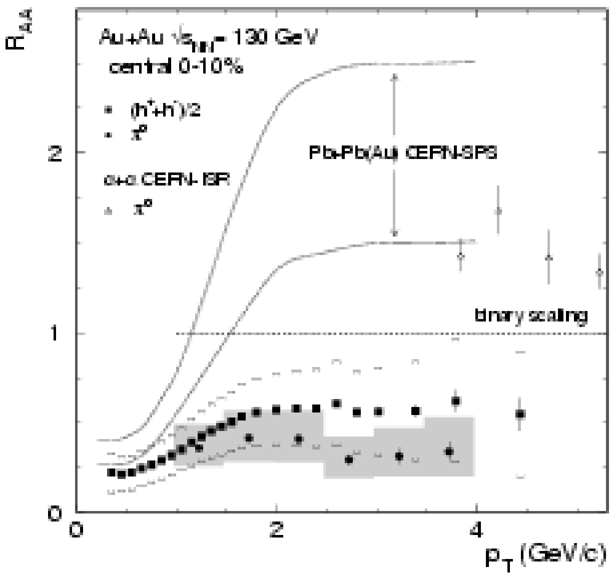

Figure 1.12: Nuclear modification factor R_{AA} for charged hadrons (squares) and neutral pions (circles) as a function of transverse moemntum for Au+Au collisions at $\sqrt{s_{NN}} = 130$ GeV (PHENIX, [44]).

to the interaction with the dense medium: while the away-side jet has to traverse it, the same-side jet is not quenched, due to surface emission.

Figure 1.15 shows the results of STAR studies concerning the pathlength dependence of the radiative energy loss. In particular, it has been shown that in peripheral collisions the suppression of the back-side jet is influenced by the relative orientation of the back-to-back pair with respect to the reaction plane[11], as a consequence of elliptic flow (see Sec. 1.3.4) [47].

1.3.4 Elliptic Flow

In heavy-ion collisions the initially spacially-anisotropic participant zone evolves through possible new forms of highly dense matter, into the final observed hadronic state. This is made of a bulk of particles with anisotropic momentum distribution in the transverse plane. Since the azimuthal anisotropy should originate in the early stages of the collision, it could shed light on the evolution of the system. A large observed anisotropy in the momentum range $p_T < 2$ GeV/c (as hydrodynamic models predict) [48], is thought to be indicative of early thermal equilibrium, while the mass dependence of this effect is argued

[11] The reaction plane is defined by the impact parameter direction and the beam direction.

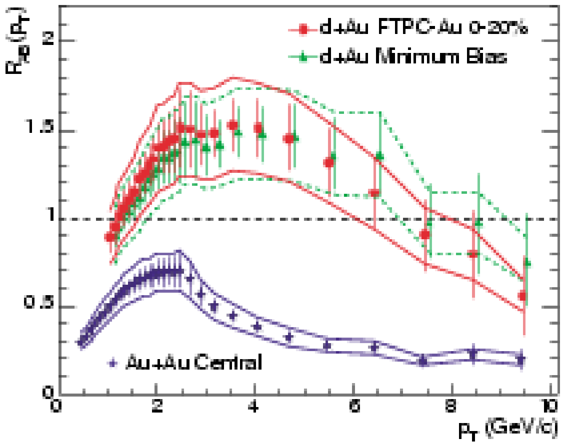

Figure 1.13: Nuclear modification factor R_{AB} (analogous to R_{AA}) for charged hadrons measured in d+Au and Au+Au collisions at $\sqrt{s_{NN}}$ = 200 GeV from the STAR experiment at RHIC [45].

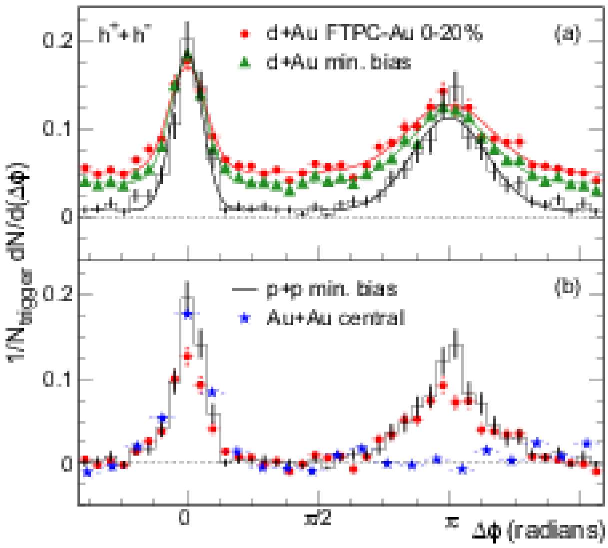

Figure 1.14: Top: Two-particle azimuthal correlations in p+p as well as in minimum bias and central d+Au collisions, [46]. Curves are fitted as described in [45]. Bottom: Comparison of two-particle azimuthal distributions for p+p, central d+Au and Au+Au collisions [46].

to be a consequence of the formation of a quark-gluon plasma [48]. At large momenta, anisotropy measurements are also important for jet quenching studies (see Sec. 1.3.3).

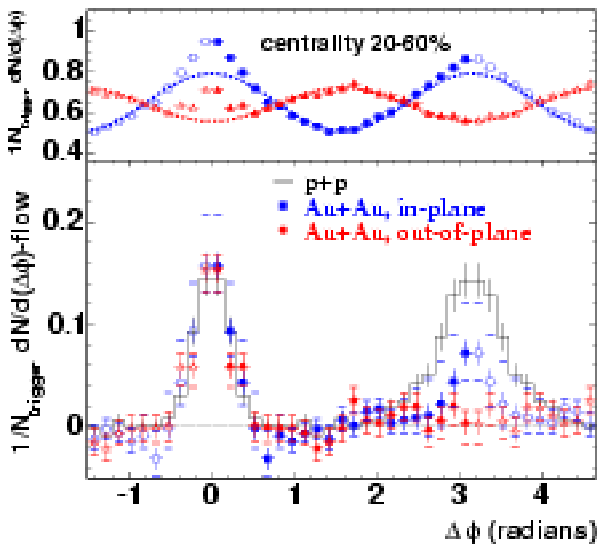

Figure 1.15: Top: Azimuthal distributions of associated particles for trigger particles in-plane (squares) and out-of-plane (triangles) for Au+Au collisions at centrality 20-60%. Open symbols are reflections of solid symbols around $\Delta\phi = 0$ and $\Delta\phi = \pi$. The elliptic flow contribution is shown by dashed lines. Bottom: Distributions after subtracting elliptic flow, and the corresponding measurement in p+p collisions (histograms) [47].

The azimuthal angular particle distribution can be described by a Fourier expansion:

$$\frac{d^2n}{p_T dp_T d\phi} \propto \left(1 + 2\sum_n v_n \cos n\left(\phi - \Psi_R\right)\right) \tag{1.9}$$

where Ψ_R is the reaction plane angle and v_2 has been called "elliptic flow" [49]. If we represent a non-central $A + A$ collision as an almond shaped particle emission source, then along the short axis (i.e. in-plane with respect to the reaction plane) the pressure gradient is larger than along the long axis (i.e. out-of-plane), resulting, eventually, in an ellipsoidal final transverse momentum space. According to thermodynamical models, this p_T dependence of v_2 is generated at the very early stages of the collision. In particular, since v_2 is driven by pressure anisotropies, and the spatial deformation of the reaction zone responsible for these anisotropies quickly disappears, the elliptic flow is sensitive to the equation of state only during the early expansion stage (~ 5 fm/c in semicentral Au+Au collisions [50]). Moreover, since particles produced from a hot dense medium can be squeezed more in the reaction plane than out of it, a freeze-out geometry will be reflected in a particle abundance ellipticity.

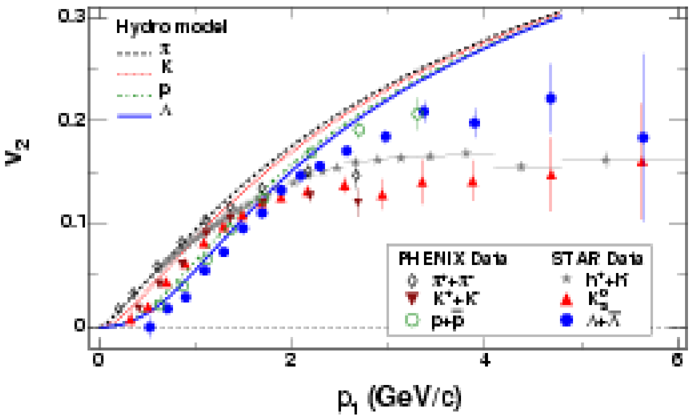

Figure 1.16: The minimum bias v_2 as a function of p_T. The STAR K_s^0 and $\Lambda+\bar{\Lambda}$ data are from [51], while the PHENIX data can be found in [52]. Hydrodynamical calculations are from [53].

Figure 1.16 shows v_2 as a function of transverse momentum for different species of particles, as measured by STAR and PHENIX experiments at RHIC [51]. As can be seen, there are three main features characterizing v_2: first, particles exhibit a thermodynamic behaviour in the low p_T region, which means that a common expansion velocity can be identified, and that the heavier the particle, the larger the momentum from hydrodynamic motion. To be noted that the mass splitting strongly depends on the equation of state [53], and the equation of state including a phase transition describes the observed data better than one without phase transition. Second, at intermediate p_T, v_2 does not strongly depend on p_T. Finally, the v_2 saturation values for baryons are higher than those from mesons, and baryons group together, as mesons do. The proposed idea that parton energy loss in the dense medium created during the collision could be the mechanism underlying the angular anisotropy v_2 (that is, the effective particle emission should occur from a shell area of the whole volume, because of the quenching of the partons inside the dense medium) is, however, still under discussion.

Studies on a quark scaling of the azimuthal anisotropy have also been perfomed [54] which can explain the v_2 dependence on the particle specie as a constituent quark anisotropy just prior to hadron formation.

1.3.5 Hanbury-Brown-Twiss Source Radii

Information about the space-time evolution of the system, about the freeze-out volume, and about the reaction geometry of heavy-ion collisions can be obtained from studies

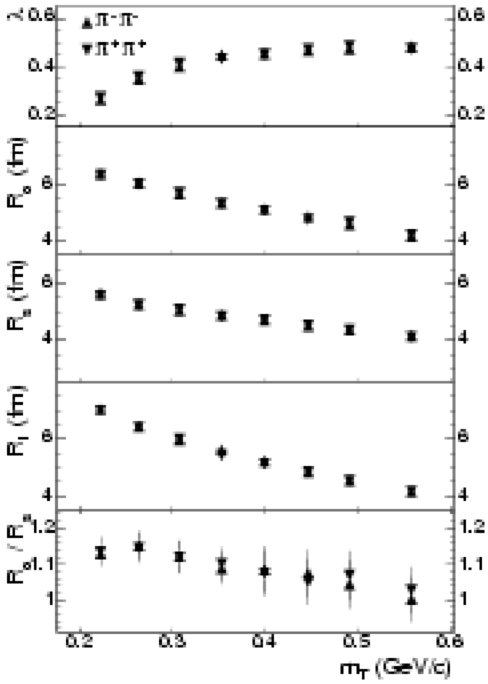

Figure 1.17: HBT parameters for 0-5% most central Au+Au events for $\pi^+\pi^+$ and $\pi^-\pi^-$ correlation functions as obtained by STAR at RHIC. For more details, see [63].

concerning intensity interferometry between identical particles (such as $\pi\pi$, KK and pp pairs). This approach was first adopted by Hanbury-Brown and Twiss when studying the angular diameter of a star using the correlation of two photons [55, 56]. According to the theory, the probability of detecting two photons in coincidence in two different detectors is correlated to the relative separation of the two detectors themselves, and, moreover, to the angular diameter of the emitting source (*Hanbury-Brown-Twiss* (HBT) *effect*). This effect has also been observed in p+$\bar{\text{p}}$ annihilations [57].

As regards heavy-ion collisions, HBT measurements can provide two correlation functions from which it is possible to obtain the longitudinal and the transverse radii, the lifetime and the flow pattern of the emitting source at freeze-out [58]. For example, the inverse width R_{out} of the "out" correlation function and R_{side} of the "side" correlation function can be used to extract a measure for the duration of the particle emission ($R^2_{out} - R^2_{side}$) and the transverse size of the source (R_{side}) [59, 60]. Besides, the lifetime of the mixed phase after the collision can appear in an enhancement of the ratio of the inverse width (R_{out}/R_{side}) of the two-particle correlation functions in the out- and sidedirections [59]. HBT also contains dynamical information that can be explored studying the transverse momentum dependence of the apparent source size [61], since the size of the regions that can be measured through HBT are controlled by velocity gradients and temperature [62]. Figure 1.17 shows the HBT dependence on the transverse mass as recently obtained by STAR at RHIC, from which, as said, dynamical information on the particle emitting source can be obtained (see [63] for more details).

Chapter 2

A Large Ion Collider Experiment: ALICE

During the last decades, the increasing interest in Quantum Chromo Dynamics favoured the proposal and the consequent realization of many experiments devoted to the study of high energy physics. The first experiments based on ultra-relativistic heavy-ion collisions developed on existing facilities, such as the Brookhaven AGS and the CERN SPS. The studies performed by fixed-target experiments (WA98, NA50 and NA57 at the SPS, and E814, E877 and E895 at the AGS, for example) acted as a launching pad for the construction of dedicated accelerators, the most important of which are the recent *Relativistic Heavy-Ion Collider* (RHIC, [64]) at Brookhaven, which has been running since summer 2000, and the *Large Hadron Collider* (LHC, [65]) at CERN (presently under construction).

During the past three years, RHIC has delivered Au+Au collisions at $\sqrt{s_{NN}} = 19.6$, 56, 62.4, 130 and 200 GeV, and d+Au and p+p collisions at $\sqrt{s_{NN}} = 200$ GeV. The results obtained by the four experiments installed at RHIC (PHENIX, STAR, BRAHMS and PHOBOS) have offered the opportunity to explore new ranges of energies and centralities, integrating with the data already available from past experiments. New frontiers can anyway be reached with the future facilities, mainly RHIC II, which is substantially an upgrade of the existing accelerator and detectors at Brookhaven, and LHC. At LHC, in particular, a program concerning Pb+Pb collisions at $\sqrt{s_{NN}} = 5.5$ TeV will be carried out by three experiments, ALICE, ATLAS, and CMS.

The LHC experimental program is going to open the door to new regimes in heavy-ion particle physics, from several points of view, such as the centre-of-mass energy, the energy density reached, the lifetime and the volume of the quark-gluon plasma system created in the collision. This is well summarized in table 2.1 where some significant heavy-ion collision parameters for SPS, RHIC and LHC are compared. Here, $\sqrt{s_{NN}}$ is the energy per nucleon pair in the centre-of-mass, $dN_{ch}/d\eta$ corresponds to the charged particle multiplicity densityper pseudorapidity unit, ε refers to the energy density at initial thermalization, V_f is the volume at freeze-out, τ_{QGP} indicates the duration of the QGP phase, and τ_0 is the time of initial thermalization. As can be seen, the values corresponding to LHC stay well above those referred to the other accelerators while the formation time τ_0 is ~ 3 times smaller.

Collision Parameter	SPS	RHIC	LHC
$\sqrt{s_{NN}}$ (GeV)	17	200	5500
$dN_{ch}/d\eta$	500	850	$2 \div 8 \times 10^3$
ε (GeV/fm^3)	2.5	$4 \div 5$	$15 \div 40$
V_f (fm^3)	10^3	7×10^3	2×10^4
τ_{QGP} (fm/c)	≤ 1	$1.5 \div 4.0$	$4 \div 10$
τ_0 (fm/c)	~ 1	~ 5	≤ 0.2

Table 2.1: Central collision parameters (see text) for the SPS, RHIC and LHC accelerators.

As a consequence of this progress with respect to past (SPS) and present (RHIC) facilities, LHC is expected to investigate new particle physics frontiers. For example, the charged particle multiplicity (which reflects the energy density of the collison), starting from the lower value of 600 at RHIC [66], at LHC is thought to reach the level of $dN_{ch}/d\eta \sim 1500 \div 4000$ [67, 68, 69] (even if ALICE, one of the four LHC experiments, has been designed to be able to work with multiplicity values up to 8000). Also the Bjorken-x range will be extended to even lower values than those reached by RHIC, where the gluon density is much higher and closer to saturation. Moreover, hard processes will dominate the $A + A$ cross-section, and high-p_T probes will be abundantly produced.

The expected luminosity for Pb+Pb collisions at LHC is about 10^{27} cm^{-2}s^{-1} which means a rather low minimum-bias interaction rate of 8 kHz (obviuosly, for lighter ions a higher luminosity can be reached). To be noted that LHC luminosity limitation comes both from the intrinsic characteristics of the detectors and from the accelerator.

2.1 The ALICE Layout

ALICE (*A Large Ion Collider Experiment*) [70, 71] is the LHC experiment fully dedicated to the study of the quark-gluon plasma which should be created during LHC Pb+Pb collision runs (p+p runs, besides offering the opportunity of studying p+p physics in an unexplored energy range at LHC, will be taken as a benchmark for the results of the heavy-ion program). Its main characteristics make ALICE highly performing to deal with the extensive LHC relativistic ion physics program and to explore nuclear matter under extreme conditions of temperature and energy density. As a consequence, the ALICE experimental program will include the study on one hand of the global properties of the collisions, such as multiplicities, rapidity distributions, collective effects, emission geometry and fluctuations in particle emission. On the other hand, more selective signatures of the creation of a quark-gluon plasma will be looked for with observables such as hadron spectra, dileptons, direct photons, charmonium and bottonium, and various other resonances (see Sec. 1.3 for a summary).

Figure 2.1 shows a schematic layout of the ALICE experiment. To be noted that the scale of the detector is mainly determined by the dimensions of the LEP L3 magnet (15 m of outer length, and 15 m of outer diameter) which provides the central detectors with a relatively weak magnetic field of 0.5 T.

2.1.1 ALICE Detectors

Central Detectors

ALICE central detectors covering the pseudorapidity region $-0.9 < \eta < 0.9$ (ITS, TPC, TRD, TOF, HMPID and PHOS) will be those aimed at particle tracking and identification.

- **Inner Tracking System - ITS**:

  Around the thin-wall beryllium beam pipe, the *Inner Tracking System* (ITS) will be mounted within the radial distance between 4 and 45 cm. It will be made up of six silicon layers: the two innermost will be made of silicon pixel detectors (SPD), the middle two of silicon drift detectors (SDD), and the outermost two of double-sided silicon strip detectors (SSD) with a small angle between the strips on the two sides. The main aim of the ITS detector is the reconstruction of the primary vertex of the collision, and of the secondary vertexes for hyperons and for charm and beauty particles. Besides, it will be able to provide particle identifiaction at low

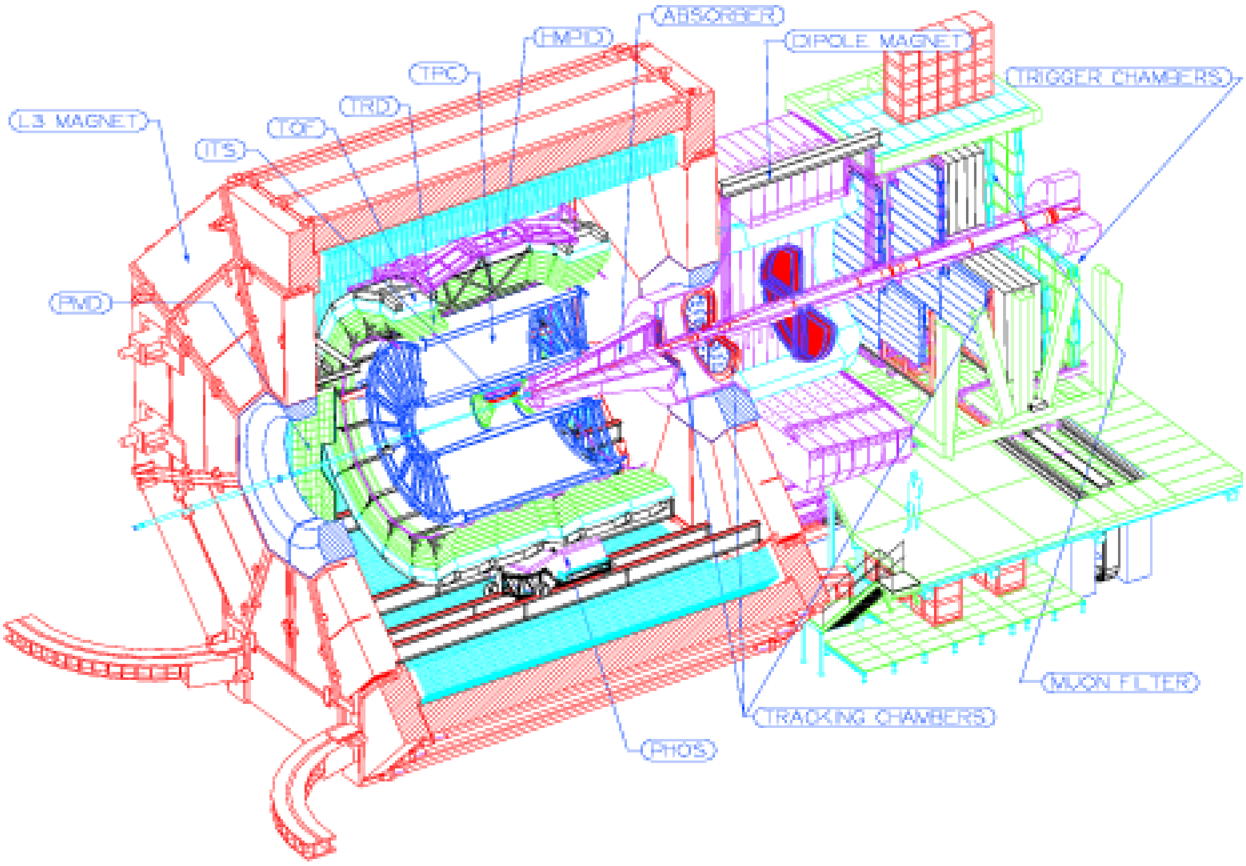

Figure 2.1: Schematic layout of the ALICE experiment.

momenta ($p < 1$ GeV/c) via dE/dx measurements, and to improve the momentum measurements coming from the TPC. Moreover, the ITS will be able to perform a stand-alone track reconstruction for low-p_T particles.

- **Time Projection Chamber - TPC**

  The ALICE *Time Projection Chamber* (TPC, see Fig. 2.2), the largest in the world, will be placed at a radial distance 85–250 cm and will have a detecting volume of 88 m^3. It will be equipped with two drift volumes of 2.5 m each, from the middle high-voltage membrane towards the two end-wheels, instrumented with proportional chambers using the cathode-pad readout. In total, the TPC will have about 6×10^5 readout channels provided with highly-integrated electronics.

  The TPC can be considered as the ALICE main tracking device with a very high

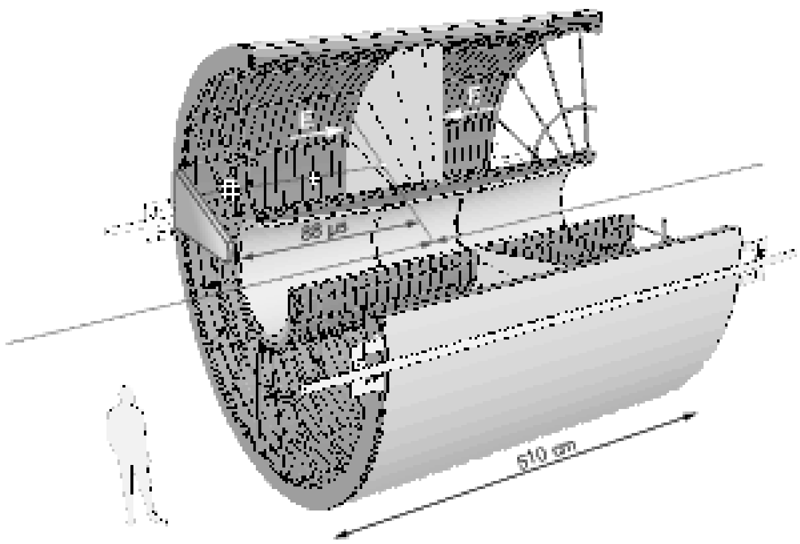

Figure 2.2: TPC schematic layout.

tracking efficiency ($> 90\%$). The two-track resolution stays below 10 MeV/c, and the momentum resolution $\sigma_p/p < 2.5\%$ up to momenta of the order of 10 GeV/c. The space-point resolution is 0.8 mm in the x- and y-directions, and 1.2 mm in the z-direction. Besides, with a dE/dx resolution of $\sim 6.8\%$ (in the worst scenario of $dN_{ch}/dy = 8000$, becoming 5.5% for isolated tracks), the TPC will provide particle identification for low-p particles (for example in the range $0.4 < p < 0.5$ GeV/c for pions).

- **Transition Radiation Detector - TRD**

  Immediately after the TPC, at a radial distance of 2.9-3.7 m, the *Transition Radiation Detector* (TRD) will concentrate mainly on the identification in the central region of high momentum electrons ($p > 1$ GeV/c, with a discrimination electrons/hadrons between ~ 1 GeV/c and ~ 100 GeV/c). It will consist of six modules in the radial direction, each with a radiator, a multi-wire proportional readout chamber and the front-end electronics for this chamber. Each readout chamber consists of a drift region of 3.0 cm separated by cathode wires from an amplification region of 0.7 cm.

  In addition to its electron identification goal, the TRD will be also used for tracking, and it will improve the transverse momentum resolution for high-momentum tracks, as shown in Fig. 2.3.

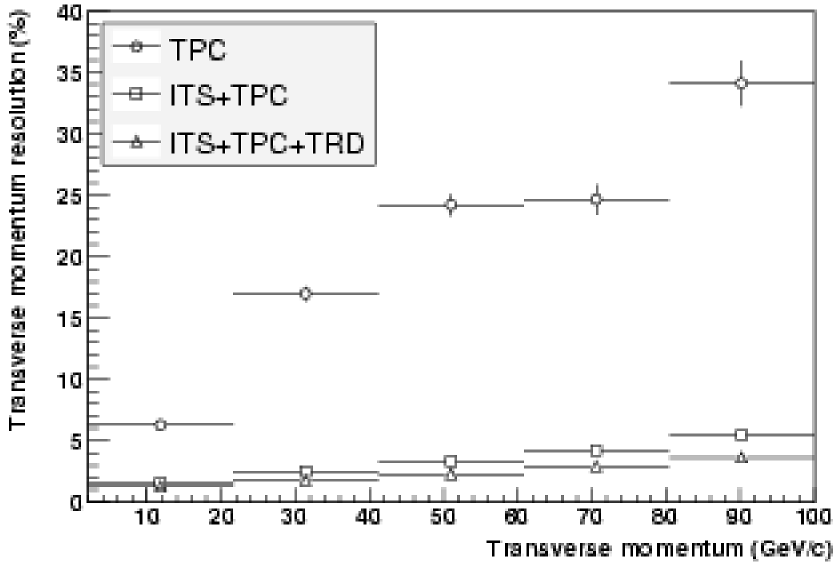

Figure 2.3: Transverse momentum resolution for different combinations of the tracking detectors in central Pb+Pb collisions ($dN_{ch}/dy = 6000$).

- **Time Of Flight - TOF**

The *Time Of Flight* (TOF) system is the detector dedicated to particle identification in the intermediate and relatively high momentum region through the measurement of the time the particle takes to travel from the interaction point to the sensitive surface of the detector (time of flight). It will be placed at 3.7 m from the centre of the experiment and will cover a cylindric surface of $\sim$ 160 m^2 with a complete azimuthal coverage. The TOF will be made up of 18 sectors in φ ($0° \leq \varphi \leq 360°$) each of which will be segmented in five units along the z coordinate. For more details, see [71].

Since the two main requirements for the TOF detector are a time resolution lower than 100 ps (to achieve a good K/π and K/p separation up to few GeV/c momentum) and a very high granularity (in order to keep the occupancy below 15%), a gauseous detector has been chosen. The TOF technology is based on the double-stack Multigap Resistive Plate Chamber (MRPC, see Figs. 2.4, 2.5, 2.6) which has an active area of 7.4×120 cm^2 and is segmented into 96 readout pads (for a total number of readout channels $\sim$ 160000). The ten gaseous gaps are of 250 μm thick each.

Thanks to an extensive R&D, according to the latest test beam results [72] the TOF

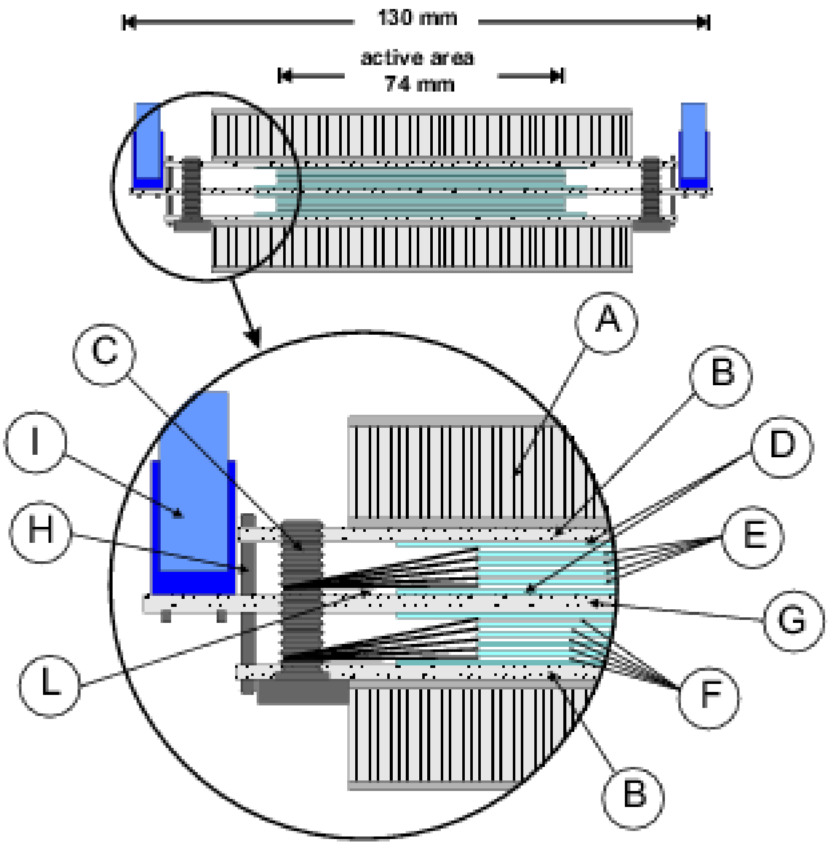

Figure 2.4: Transverse section of a TOF double-stack MRPC. The following elements can be seen: (A) honeycomb panel; (B) PCB with cathodic pads; (C) plexiglass screws for the fishing line wiring; (D) external glasses; (E) internal glasses; (F) 250 μm width gaps; (G) central PCB with anodic pads; (H) metallic pins for transporting the signal from the cathodes to the central PCB; (I) flat cable connector.

intrinsic resolution is now ~ 50 ps, with an efficiency $> 99\%$. The particle identification capabilities of the Time Of Flight detector thus allow a $\sim 3\sigma$ separation in the range $0.2 \div 2.5$ GeV/c for K/π and up to 4 GeV/c for K/p, as required.

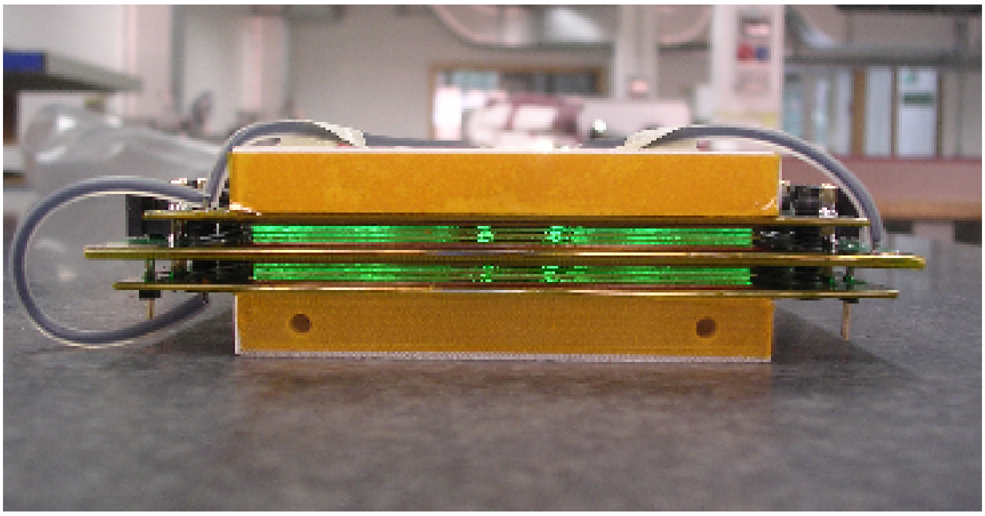

Figure 2.5: Transverse section of a TOF double-stack MRPC.

Figure 2.6: Photograph of a TOF MRPC during the assembly phase.

- **H**igh **M**omentum **P**article **I**dentification **D**etector - **HMPID**

  Positioned at ~ 4.9 m from the beam line, the *High Momentum Particle IDentification* detector (HMPID) is aimed at the identification of very high-p particles (up to 5 GeV/c for K/p separation) in a small acceptance window. It is a single arm proximity focus ring-imaging Cherenkov counter, consisting of seven modules (with a surface of 1.5×1.5 m^2 each), for a total of 160000 readout channels, and a total active surface of ~ 10 m^2.

  Cherenkov photons, emitted when a fast charged particle traverses the radiator, are detected by a photon counter which exploits the novel technology of a thin layer of CsI deposited onto the pad cathode of a Multi-Wire Pad Chamber (MWPC). The ALICE HMPID represents the largest scale application of this technique [73].

- **P**hoton Spectometer - **PHOS**

  At the bottom of L3, in the pseudorapidity region $-0.12 < \eta < 0.12$, there will be a high-resolution high-granularity electromagnetic calorimeter, the *Photon Spectrometer* (PHOS). The PHOS will include a highly segmented ElectroMagnetic CAlorimeter (EMCA) and a Charged-particle Veto (CPV) detector. It will be divided into five independent EMCA+CPV units (named PHOS modules).

  The PHOS detector will detect electromagnetic particles and identify photons and neutral mesons through the two-photon decay channel. The aim of the PHOS is to test the thermal and dynamical properties of the very first stages of the collision, and to study jet quenching as a QGP signal.

Forward **D**etectors

Far away from the interaction point, at large rapidity values, ALICE will be endowed with smaller detectors.

- Muon Spectometer: The ALICE *Muon Spectometer*, which will be placed in the region $2.5 < \eta < 4.0$, is the detector encharged of studying the spectrum of heavy quark vector mesons (such as the J/ψ and the ψ', see Fig. 2.7), as well as the ϕ meson via the $\mu^+\mu^-$ decay channel. In particular, since at LHC energies the continuum of the unlike-sign dimuon spectrum is expected to be dominated by semileptonic decays of open charm and open beauty, the muon spectrometer will offer the opportunity of studying the production of open heavy flavours.

The muon spectrometer will consist of a passive front absorber (to absorb hadrons and photons from the interaction vertex), a highly-granularity tracking system of ten detection planes, a large dipole magnet, a passive muon filter wall followed by four planes of trigger chambers, and an inner beam shield to protect the chambers from particles and secondaries produced at large rapidities.

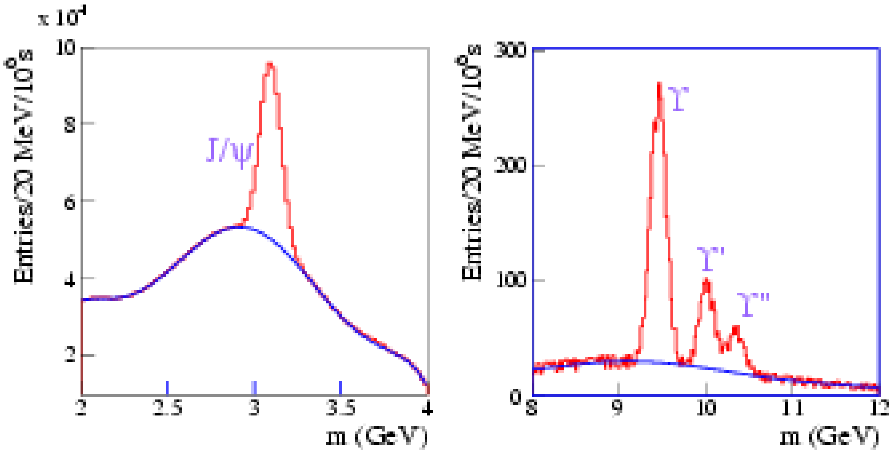

Figure 2.7: Opposite sign dimuon mass spectra in the region $2 < m < 4$ GeV (left) and $8 < m < 12$ GeV (right) for the 10% most central Pb+Pb reactions (see [74] for more details). The centrality definition in terms of percentage refers to the total Pb+Pb inelastic cross-section $\sigma^{\text{inel}}_{\text{Pb+Pb}}$.

- **Zero Degree Calorimeter - ZDC**: The *Zero Degree Calorimeter* (ZDC) is the detector which will be placed at 116 m from the interaction point. It will provide a measure of the number of participating nucleons, which is strongly related to the centrality and, as a consequence, to the geometry of the collision.

  The ZDC will be equipped with two distinct detectors, one for spectator neutrons (at zero degree relative to the LHC beam axis) and one for spectator protons (placed externally to the outgoing beam pipe, on the side where positive particles are deflected). The ZDC detector will use a quartz fibre calorimetry technique: the shower generated by incident particles in a dense absorber (the "passive" material) will produce Cherenkov radiation in the quartz fibres (the "active" material) interspersed in the absober. Since the available space is very limited, the ZDC passive material for the absorber has to be very dense to contain the shower. Moreover, the high level of radiation exposure will be contrasted thanks to the radiation resistance of the quartz fibres.

- **Photon Multiplicity Detector - PMD**: The *Photon Multiplicity Detector* (PMD) will be installed at 360 cm from the centre of the interaction, and will cover the pseudorapidity region $2.3 \leq \eta \leq 3.5$. It is a preshower detector aimed at the measurement of the multiplicity and spacial ($\eta - \phi$) distribution of photons on an event-by-event basis. It will investigate the formation of the Disoriented Chiral Condensate (DCC) [75], and carry on studies related to event-by-event fluctuations, flow, transverse electromagnetic energy, and reaction plane.

  The PMD will consist of two identical planes of detectors with a $3X_0$ thick lead converter in between them. The front detector plane will be used for vetoing charged-particle hits, while the detector plane behind the converter (the preshower plane) will register hits from both photons and charged hadrons.

- **Forward Multiplicity Detector - FMD**: The *Forward Multiplicity Detector* (FMD) will provide charged-particle multiplicity information in the pseudorapidity region $-3.4 < \eta < -1.7$ and $1.7 < \eta < 3.4$.

  The FMD will consist of 51200 silicon strip channels distributed over five rings (three inner and two outer), placed at three different distances from the nominal interaction point, with 10 (for the inner rings) or 20 (for the outer rings) silicon sectors in azimuthal angle. Each sector will be read out independently. With respect to an outer ring, an inner one will contain half of the strips (512 (1024) or 256 (512) strips for the inner and the outer, respectively). The total number of strips has been set such to have, on average, approximately one particle per strip per event.

- **V0 and T0 Detectors**: Finally, the *V0* and *T0* detectors will provide fast trigger signals. In particular, V0 will be encharged of providing a fast measure of the event multiplicity and interaction vertex, while T0 will determine the time of collision (providing in this way a reference timing signal for the TOF detector).

  The V0 detector will be made up of two arrays located asymmetrically on each side of the interaction point, segmented into 32 elementary counters distributed in four rings. The rings will be subdivided into eight sectors of 45° each. The elementary counters will consist of scintillator material with embedded wavelength shifter (WLS) fibres. The light from the WLS fibres will be collected by clear fibres and transported to a photomultiplier. The time resolution of each individual counter will be better than 1 ns.

On the other hand, the T0 detector will consist of two arrays of Cherenkov counters, with 12 counters per array. Each Cherenkov counter is based on a fine-mesh photomultiplier tube. The two arrays will be placed at different longitudinal distances from the nominal beam interaction point (the one on the right side will be very close to it, because of the presence of other detectors), as close to the beam pipe as possible in the radial direction to maximize triggering efficiency.

2.2 ALICE Detector Performance

As already said, ALICE physics program will cover several issues mainly concerning QCD, and, in particular, the predicted quark-gluon plasma as the highly dense matter state resulting from ultra-relativistic heavy-ion collisions. As this is an open field in particle physics, ALICE will hopefully shed light on many aspects of the theory still obscure, measuring observables, involving soft and hard processes, related both to the global characteristics of the fireball created in the collision, and more specific probes of the deconfinment and the chiral symmetry restoration predicted by QCD. For example, extensive studies on multiplicities and transverse energy distributions, hadron ratios and spectra will be carried on, as well as on open heavy flavour production and jet quenching effects (for a recent overview, see [76]). Obviously, in order to garantee a good performance with respect to all these measurements, a large acceptance, secondary vertex reconstruction, photon identification, and, most of all, an accurate tracking system and a remarkable hadron and lepton particle identification capability over a wide momentum range (up to ~ 100 GeV/c), are required.

Sec. 2.1 has given a rather general overview of the ALICE detectors, which have to be able to satisfy all the requirements of the experiment. In this Section, the combined detector performance in terms of tracking and charged particle identification will be described. The results which are going to be presented have been obtained using the ALICE off-line simulation and reconstruction framework AliRoot [71]. Details about the GEANT3 transport code are reported in [77], while those concerning the HIJING Monte Carlo generator used can be found in [78].

2.2.1 Reconstruction

Track reconstruction is one of the most challenging tasks of ALICE detectors. As a matter of fact, determining the momentum of the particles at the point where they had been generated (was it the interaction point or a secondary vertex) is of great interest, as well as a detailed reconstruction up to the detectors devoted to particle identification (TOF, HMPID, and PHOS), which are farther from the centre of the experiment than the tracking detectors.

Coordinate System in Central Detectors

The reconstruction algorithms developed for ALICE central tracking detectors (ITS, TPC and TRD) are based on a common convention on the coordinate system, such that all the clusters[1] and the tracks are always expressed in some local coordinate system related to a given subdetector. In particular, the local coordinate system is right-handed Cartesian, with the origin and the z axis coinciding with those of the ALICE global coordinate system, and the x axis perpendicular to the subdetector's sensitive plane. In this way, the symmetry of the ALICE set-up reflects in the local system, and the reconstruction equations become easier.

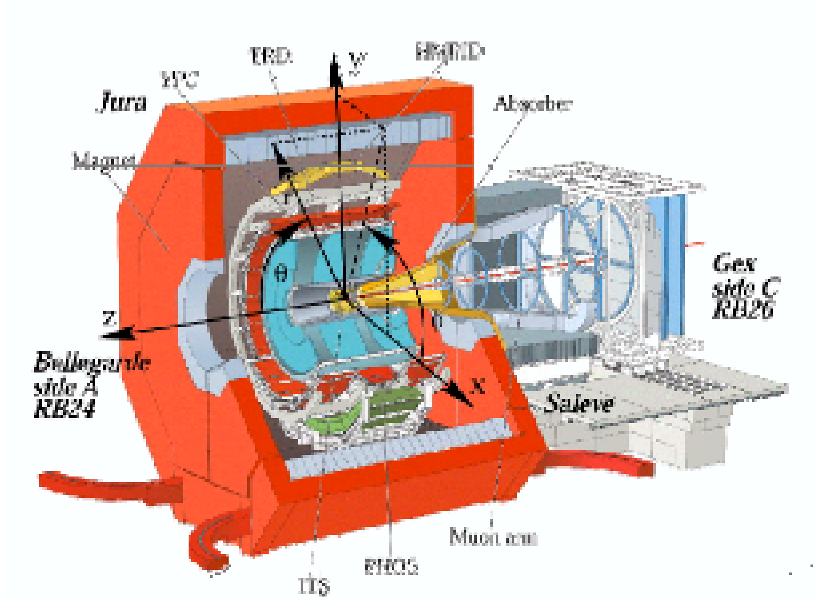

Figure 2.8: Definition of the ALICE coordinate system axes, angles and detector sides.

[1]Let's call *digit* a digitized signal obtained by a sensitive unit of a detector at a certain time. Then, a *cluster* is defined as a set of adjacent (in space and/or time) digits, presumably originated by the same particle while crossing a detector sensitive volume.

With *space points* one refers to the estimates of the position where a particle crossed the detector volume (usually calculated from the centre of gravity of the correspondent cluster), while the *reconstructed tracks* are, in fact, sets of parameters (curvature, angles...) of the particle's trajectory together with the corresponding covariance matrix estimated at a given point in space.

Vertex Reconstruction

The first step in the reconstruction procedure is the estimation of the position of the primary vertex. This is done by the ITS detector, using the clusters reconstructed in the two pixel layers. In the case of central Pb+Pb collisions, a resolution of about 5 μm in the beam direction and of about 25 μm in the transverse plane will be reached, while for p+p collisions it will be about an order of magnitude worse. Anyway, in the p+p case, since particle multiplicity will be very low (almost three orders of magnitude lower than that in Pb+Pb central collisions), the lower precision on the determination of the primary vertex will not have any signifcant impact on the reconstruction of physical signals (such as D^0's and V^0's[2]). Figure 2.9 shows the results obtained for the reconstruction of the primary vertex by the ITS in Pb+Pb collisions [76].

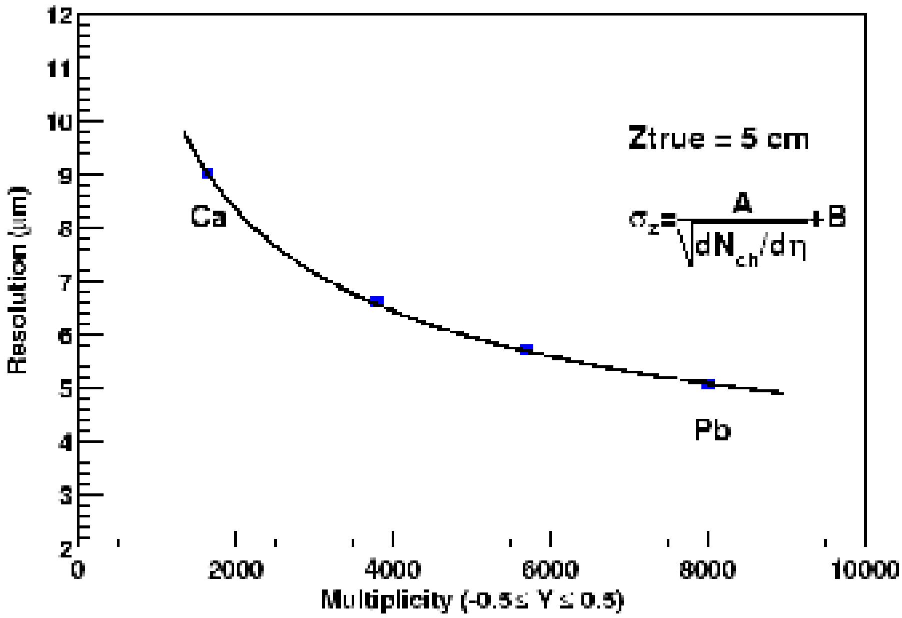

Figure 2.9: Resolution of the reconstructed vertex position as a function of the charged particle multiplicity for $B = 0.2$ T. For details on the solid line fit see [76].

[2] V^0 refers to the decay topology of the strange particles (Λ, $\bar{\Lambda}$ and K^0_s).

ALICE Track Finding and Reconstruction

There are two possible approaches when performing track reconstruction. On one hand, one can choose to apply a so-called global method; on the other, reconstruction can be carried out using a local method approach. In global methods, such as those based on combinatorial algorithms, or the Hough transfom [79], the track measurements are all treated at the same time, and all the information available for each track is always used in each step of the algorithm (for example, when deciding if a measurement has to be included of not). The main advantage of these methods is the fact that they are quite insensible of noise, and that they can operate directly on raw data. The drawback is, however, the fact that these approaches require a precise global track model, i.e. a parametrization of the whole track trajectory taking into account the effects from the magnetic field and multiple scatterings, with respect to which the entire set of measured points must be fitted.

On the contrary, local methods do not need to know any global track model, and exploit local estimates of the track at a given space point. Every decision concerning the track is taken considering the local information, or the information coming from the previous "history" of the track itself. The main disadvantages of these methods are the fact that they are more affected by uncertainties due to noise, by wrong or displaced measurements, and by the precision of the space point error parametrization. As a conseuqence, even if they can well take into account the peculiarities of the tracks, local approaches have to rely on sophisticated space point reconstruction algorithms. The most advanced kind of local track-finding is the Kalman filtering [80].

Kalman Filter

The Kalman filter is a set of mathematical equations that provides an efficient computational (recursive) solution of the least-squares method. The filter is very powerful from several points of view: it gives an estimation of past, present and even future states, and this holds true even when a precise model for the system is not available.

The Kalman filter addresses the general problem of describing the state of a discrete-time controlled process that is governed by a stochastic difference equation (linear or not). Let's assume that a certain "system" is described at a given time t_k by a state vector x_k. This system varies its state from time $t_k - 1$ to t_k according to the evolution equation:

$$x_k = f_k(x_k - 1) + \varepsilon_k, \tag{2.1}$$

where f_k is a known deterministic function and ε_k is a random vector of intrinsic "process noise" with a zero mean value ($\langle\varepsilon_k\rangle = 0$) and a known covariance matrix ($\mathrm{cov}(\varepsilon_k) = Q_k$). Generally, only a function of the state vector can be observed, and the result of the observation m_k is corrupted by a "measurement noise" δ_k:

$$m_k = h_k(x_k) + \delta_k,$$

where h_k is the measurement function which, in this case, is a certain matrix H_k. The measurement noise is also assumed to be unbiased ($\langle\delta_k\rangle = 0$) and to have a definite covariance matrix ($\mathrm{cov}(\delta_k) = V_k$). Let's suppose that some estimates of the state vector $\tilde{x}_{k-1}$ and of its error matrix $\tilde{C}_{k-1} = \mathrm{cov}(\tilde{x}_{k-1} - x_{k-1})$ are known at a certain time slot t_{k-1}. Then, these estimates can be extrapolated to the next time slot t_k by means of formulas:

$$\begin{aligned} \tilde{x}_k^{k-1} &= f_k(\tilde{x}_{k-1}), \\ \tilde{C}_k^{k-1} &= F_k \tilde{C}_{k-1} F_k^T + Q_k, \qquad F_k = \frac{\partial f_k}{\partial x_{k-1}}, \end{aligned} \tag{2.2}$$

which are called "prediction". The value of the predicted χ^2-increment can also be calculated:

$$\left(\chi^2\right)_k^{k-1} = \left(r_k^{k-1}\right)\left(R_k^{k-1}\right)^{-1} r_k^{k-1}, \quad r_k^{k-1} = m_k - H_k \tilde{x}_k^{k-1}, \qquad R_k^{k-1} = V_k + H_k \tilde{C}_k^{k-1} H_k^T \tag{2.3}$$

where the number of degrees of freedom is equal to the dimension of the vector m_k. The difference r_k^{k-1} in Eq. 2.3 is called the measurement innovation, or the residual. The residual reflects the discrepancy between the predicted measurement $H_k \tilde{x}_k^{k-1}$ and the actual measurement m_k. In particular, a residual of zero means that the two are in complete agreement.

If the result of the state vector measurement at the moment t_k is available, together with the results of the prediction, it is possible to combine this additional information with the prediction results to improve the state vector estimate using the "filtering" procedure:

$$\tilde{x}_k = \tilde{x}_k^{k-1} + K_k\left(m_k - H_k \tilde{x}_k^{k-1}\right), \tag{2.4}$$

$$\tilde{C}_k = \tilde{C}_k^{k-1} - K_k H_k \tilde{C}_k^{k-1}, \tag{2.5}$$

where K_k is the *Kalman gain* (or *blending factor*) matrix:

$$K_k = \tilde{C}_k^{k-1} H_k^T \left(V_k + H_k \tilde{C}_k^{k-1} H_k^T\right)^{-1}. \tag{2.6}$$

It can be shown that K_k minimizes the *a posteriori* error covariance $\tilde{C}_k$ of Eq. 2.5.

From Eq. 2.6 it is possible to infer that as the measurement error covariance V_k approaches zero, K_k weights the residuals more heavily. That is,

$$\lim_{V_k \to 0} K_k = H_k^{-1}.$$

On the other hand, as the *a priori* estimate error covariance $\tilde{C}_k^{k-1}$ approaches zero, the gain K_k weigths the residuals less heavily:

$$\lim_{\tilde{C}_k^{k-1} \to 0} K_k = 0.$$

Another way of interpreting the weighting effect of K_k is that as the measurement error covariance V_k approaches zero, the actual measurement m_k is "trusted" more and more, while the predicted measurement $H_k \tilde{x}_k^{k-1}$ is trusted less and less. On the other hand, as the *a priori* estimate error covariance $\tilde{C}_k^{k-1}$ approaches zero the actual measurement is trusted less and less, while the predicted one $H_k \tilde{x}_k^{k-1}$ is more and more trusted.

Finally, the value of the filtered χ^2-increment is given by:

$$\chi_k^2 = (r_k)^T (R_k)^{-1} r_k, \quad r_k = m_k - H_k \tilde{x}_k, \quad R_k = V_k - H_k \tilde{C}_k H_k^T. \tag{2.7}$$

It can be shown that the predicted chi-square equals the filtered chi-square:

$$\left(\chi^2\right)_k^{k-1} = \chi_k^2.$$

The algorithm described so far makes the Kalman filter estimate a process using a form of feedback control: the filter estimates the process state at a certain time, and then obtains feedback in the form of noisy measurements. The "prediction" and "filtering" steps are repeated as many times as we have measurements of the state vector.

The Kalman filter procedure can be applied to two types of problems: time update and measurement update. In the first case, the resulting equations are responsible for projecting forward in time the current state and error covariance estimates to obtain the *a priori* esimates for the next time step (see Eqs. 2.2). On the other hand, measurement update equations are responsible for incorporating a new measurement into the *a priori* estimate to obtain an improved *a posteriori* estimate (see Eqs. 2.5). While in the first case we speak of "predictor" equations, in the latter case we speak of "corrector" equations, making the algorithm a *predictor-corrector* algorithm.

After each time and measurement update pair, the process is repeated with the previous *a posteriori* estimates used to project the new *a priori* estimates. This recursive nature is one of the very appealing features of the Kalman filter with respect to other techniques such as the Wiener filter [81].

Kalman Filter in High-Energy Physics

Kalman filtering algorithms are extensively used in high-energy physics, with lots of advantages, and some shortcomings as well [82]. In particular, for track reconstruction problems, the main attractive features of the Kalman filter are:

- It is a method for simultaneous reconstruction and fitting.
- As already pointed out, with this method it is possible to reject incorrect space points “on the fly”, during the only tracking step. Such incorrect points can appear as a consequence of the imperfection of the cluster finder. They can be due to noise or they can be wrong points from other tracks accidentally captured in the list of points to be associated with the track under construction. With respect to this, in the case of a global tracking approach, one usually needs an additional fitting pass to get rid of these incorrect points.
- In the case of substantial multiple scattering, track measurements are correlated, and therefore large matrices (of the size of the number of measured points) are to be inverted during a global fit. In the Kalman filter procedure we only have to manipulate up to 5×5 matrices (although as many times as we have measured space points), which is much faster.
- One can handle multiple scattering and energy losses in a simpler way than in the case of global methods.
- It is a natural way to find the extrapolation of a track from one detector to another (e.g. from the TPC to the ITS or the TRD).

Considering the list of features mentioned above, it is easy to understand the extensive use of the Kalman filter procedure in high-energy experiments. In particular in ALICE, the Kalman filtering technique has been chosen for the offline reconstruction since it well suits the ALICE requirements of having a good track-finding efficiency and a precise reconstruction for tracks even at low momenta ($p_T \sim 100$ MeV/c). Such a technique will be required also because energy loss and multiple scattering effects will considerably affect track reconstruction (because of the significant material budget of the tracking detectors, ITS and TRD in the first place), as well as rather big dead zones between the detectors. As a consequence, considering its features (as listed above), Kalman filter has been chosen for the offline reconstruction.

For what concerns the mathematical formalism, the track parametrization in ALICE is given by:

$$\begin{cases} \phi(r) &= \gamma_0 + \arcsin \frac{Cr+(1+CD)D/r}{1+2CD} \\ z(r) &= z_0 + \frac{\tan\lambda}{C} \arcsin\left(C\sqrt{\frac{r^2-D^2}{1+2CD}} \right) \end{cases}$$

where ϕ, z, and r are cylindrical coordinates of a given track point, λ is the track dip angle, $C = 1/(2R)$ is half track curvature, γ_0 is the slope of the track projection in the xy-plane at the point of minimal distance from the coordinate origin and D and z_0 are the track transverse and longitudinal impact parameters, respectively. The sign of C and D depends on the particle charge and track position with respect to the coordinate origin. The state vector for the Kalman filter procedure is defined as:

$$x_k^T = (\phi_k, z_k, D, \tan\lambda, C).$$

The vector of measurements, its error matrix and the measurement matrix are given respectively by:

$$m_k = \begin{pmatrix} r_k\phi_k \\ z_k \end{pmatrix}, \quad V_k = \begin{pmatrix} \sigma_{r\phi}^2 & 0 \\ 0 & \sigma_z^2 \end{pmatrix}, \quad H_k = \begin{pmatrix} r_k & 0 & 0 & 0 & 0 \\ 0 & 1 & 0 & 0 & 0 \end{pmatrix}.$$

Then, according to the general Kalman formulae, the prediction of the state vector is:

$$\tilde{x}_k^{k-1} = f_k(\tilde{x}_{k-1}) \Leftrightarrow \begin{cases} \tilde{\phi}_k^{k-1} &= \tilde{\phi}_{k-1} + \arcsin(A_k) - \arcsin(A_{k-1}) \\ \tilde{z}_k^{k-1} &= \tilde{z}_{k-1} + \frac{\tilde{\tan}\lambda_{k-1}}{\tilde{C}_{k-1}}(\arcsin(B_k) - \arcsin(B_{k-1})) \\ \tilde{D}_k^{k-1} &= \tilde{D}_{k-1} \\ \tilde{\tan}\lambda_k^{k-1} &= \tilde{\tan}\lambda_{k-1} \\ \tilde{C}_k^{k-1} &= \tilde{C}_{k-1} \end{cases}$$

where

$$A_k = \frac{\tilde{C}_k r_k + (1+\tilde{C}_k\tilde{D}_k)\tilde{D}_k/r_k}{1+2\tilde{C}_k\tilde{D}_k}, \quad \text{and} \quad B_k = \tilde{C}_k\sqrt{\frac{r_k^2-\tilde{D}_k^2}{1+2\tilde{C}_k\tilde{D}_k}}.$$

The error matrix prediction $\tilde{C}_k^{k+1}$ can be obtained with the F_k-matrix calculated from the system above ($x_{k-1} = \tilde{x}_{k-1}$)

$$F_k = \left. \frac{\partial(\phi_k^{k-1}, z_k^{k-1}, D_k^{k-1}, \tan\lambda_k^{k-1}, C_k^{k-1})}{\partial(\phi_{k-1}, z_{k-1}, D_{k-1}, \tan\lambda_{k-1}, C_{k-1})} \right|_{x_{k-1}=\tilde{x}_{k-1}}.$$

Finally, the matrix Q_k should be evaluated: it describes the multiple scattering distortion and takes into account the energy losses. In particular, the multiple scattering is assumed to affect only the track direction, without distorting the track position. On the other hand, the energy loss is taken into account using a simplified Bethe-Block formula, which adopts the pion mass for all the particles:

$$\Delta E = \frac{0.153}{\beta^2}\left(\ln\frac{5940\beta^2}{1-\beta^2} - \beta^2\right)\Delta x. \tag{2.8}$$

With this formula, the change of the current track curvature when the track crosses a layer of the next detector is

$$C_{new} = C_{old}\left(1 - \frac{E}{p^2}\Delta E\right)$$

where C_{new} and C_{old} are the track curvatures after and before the layer crossing, respectively, E and p are the particle energy and momentum (assuming the pion mass for the particle), and ΔE comes from Eq. 2.8.

ALICE Tracking Strategy

After having reconstructed the primary vertex using the clusters in the two pixel layers of the ITS detector, the track finding procedure starts. Each tracking detector is endowed with its own specific algorithm, which depends on the features of the detector itself (see [76] for more detailed descriptions). Moreover, because of the very high occupancy and the big number of overlaps between different clusters, the cluster finding and track reconstruction are not always independent the one from the other, and the number of cluster is finally set only during the track finding step.

The strategy which has been chosen starts from the ALICE subdetector with the most excellent tracking capabilities, the TPC, and, in particular, from its outer radius, where the track density is lower. The candidate "seeds" (which are basically good initial approximations of the track parameters and of their covariance matrices) are looked for, but since the precision on the parameters is quite low (because the number of associated clusters is small), no outward extrapolation can be performed. Instead, the tracking goes on inwards, towards the TPC inner radius, and whenever possible, new clusters are associated to the track applying a Kalman filter algorithm, and the parameters of the track are more and more refined.

Then, when the innermost radius of the TPC has been reached, the tracking in the ITS detector is performed. The ITS tries to prolong the TPC tracks to the primary vertex, while the tracks are continuously updated with additional, precisely reconstructed ITS clusters, also improving the estimation of the track parameters.

After this, a special standalone tracking procedure is applied to the rest of the ITS clusters which have not been associated to any track. This step is meant to recover the tracks which were not found in the TPC because of p_T cuts, dead zones between the TPC sectors or decays.

The next step is a tracking back to the outer layer of the ITS, and then to the outer radius of the TPC. For the tracks that were labelled by the ITS as primary, some particle-mass dependent time-of-flight hypothesis are calculated, which will be then used during the particle identification procedure performed by the TOF detector.

Once the outer layer of the TPC has been reached, the precision on the track parameters is sufficient to extrapolate them to the external detectors, the TRD, TOF, HMPID and PHOS. In the TRD, the track reconstruction is performed in a way similar to that in the TPC: the track is prolonged to the outer TRD radius, and the assigned cluster is used to improve the momentum resolution. Next, the extrapolation goes on to the TOF, the HMPID and the PHOS, where particle identification occurs. Finally, a Kalman filter algorithm is applied backwards to the primary vertex (or the innermost possible radius, in case of secondary tracks).

The tracks that have been fit back to the primary vertex are then used for secondary vertex (V^0, cascade, kink) reconstruction. At present, an algorithm which should identify secondary vertexes "on the fly" is under study. It should have the advantage of minimizing the risk of wrong track prolongations, since it will not propagate the tracks coming from secondary vertexes beyond it.

ALICE Track Finding Performance

The performance of the track finding procedures adopted by the various detectors (see [76] for more detailed descriptions) can be characterized by many different parameters. Here the results of the track reconstruction algorithms developed by each tracking detector (ITS, TPC, TRD) will be briefly presented.

- **TPC**

  For what concerns the TPC track reconstruction algorithm, two types of efficiency can be defined, the algorithmic efficiency, and the "physical" efficiency. While the first is the ratio of the number of "good found" tracks to the number of "good generated" tracks reflecting the efficiency of the algorithm, the physical efficiency includes also all other factors, like dead zones in the detectors, inefficiency of the electronics, decays, and so on.

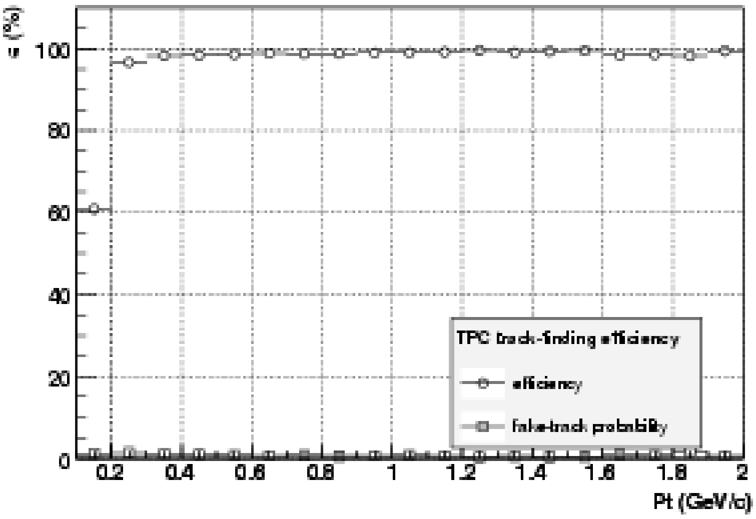

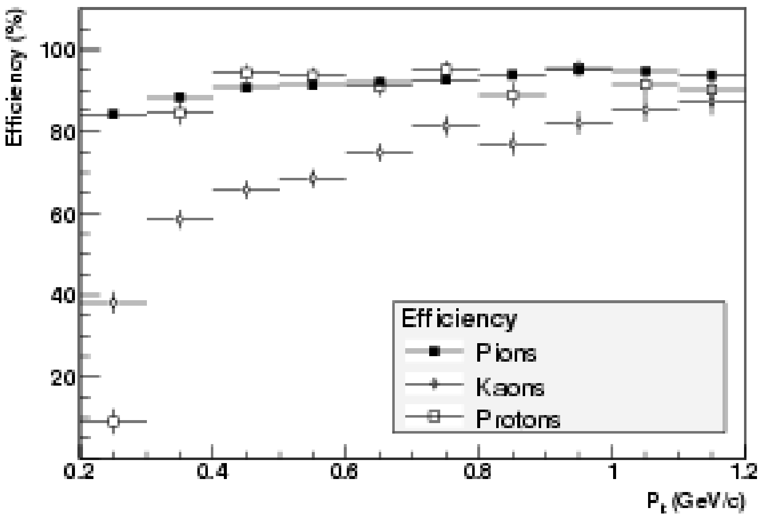

Figure 2.10: Top: Efficiency of the TPC track-finding algorithm as a function of particle transverse momentum. Bottom: Physical efficiency of the TPC track-finding algorithm as a function of particle transverse momentum for different particle species. The results refer to central Pb+Pb collisions ($dN_{ch}/d\eta = 6000$).

Figure 2.10, upper panel, shows the algorithmic efficiency for the TPC track finding procedure as a function of the particle transverse momentum. The fake-track probability is also shown, referring to uncorrect assignment of clusters to tracks

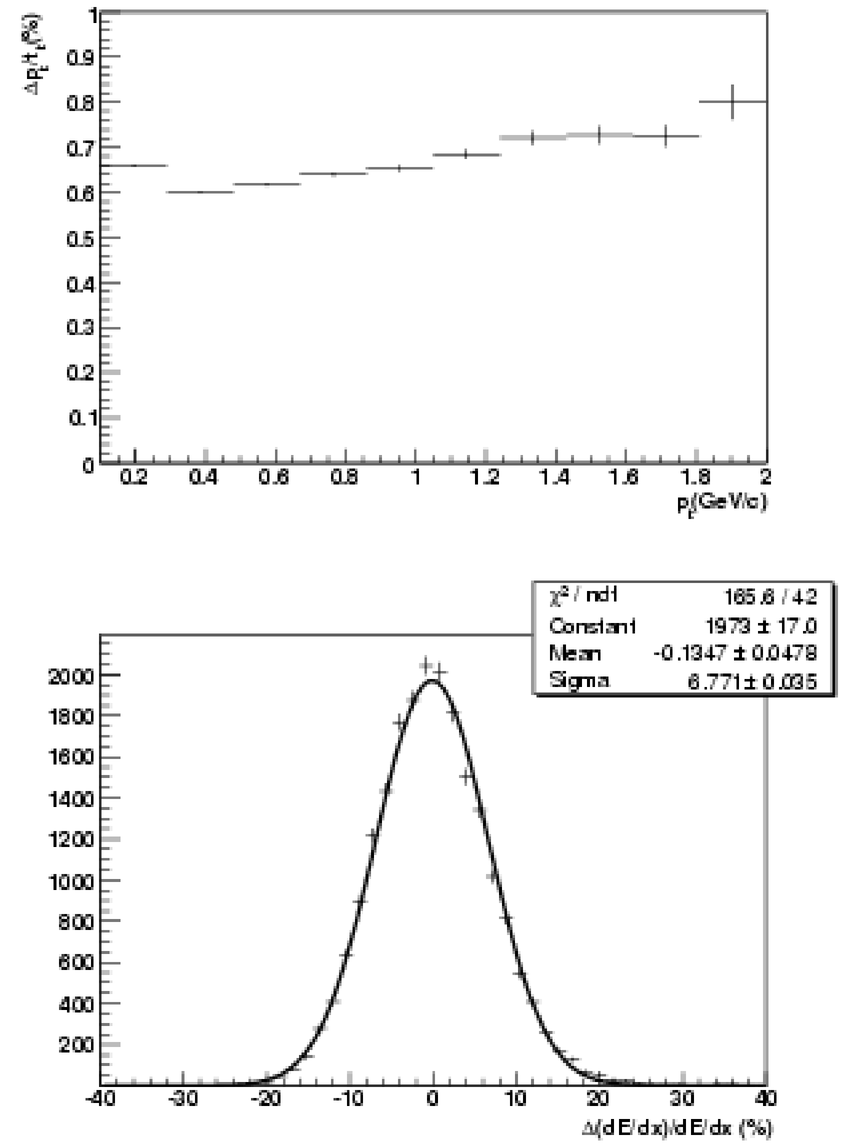

Figure 2.11: Transverse momentum (top) and dE/dx (bottom) resolutions for TPC measurements in central Pb+Pb collisions ($dN_{ch}/d\eta = 6000$). The former is given as a function of p_T.

(see [76] for more details). As it can be seen, there is no significant dependence of the efficiency on the particle transverse momentum: the efficiency stays around $\sim 100\%$ for the whole range, apart from a small decrease at low momenta ($p_T < 0.2$ GeV/c).

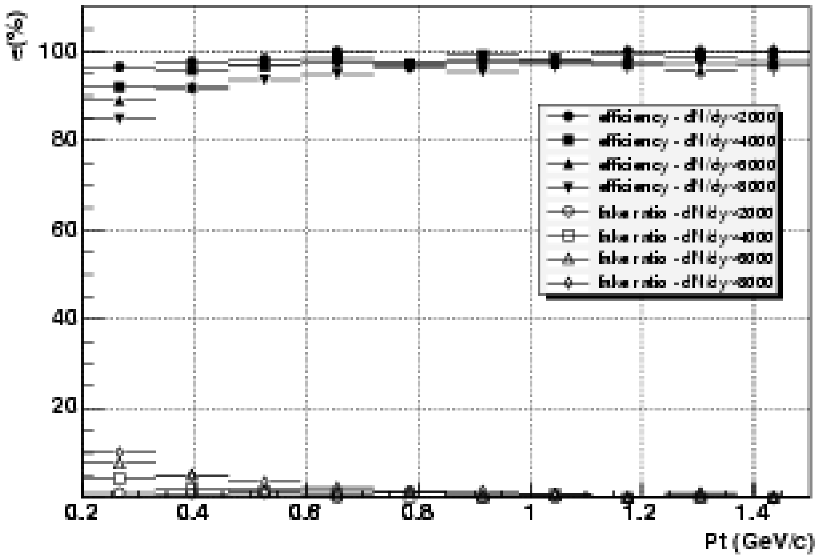

Figure 2.12: TPC+ITS track-finding efficiency and fake-track probability as a function of the transverse momentum for different track multiplicities.

The lower panel of Fig.2.10 shows the physical efficiency of the TPC reconstruction. In this case, in the low-momentum region a decrease can be observed, which is due to energy loss, interactions in the material and particle decays. The physical efficiency dependence on the particle species can be explained bearing in mind that, for the same value of p_T, these effects affect in a different way different types of particles.

The transverse momentum and dE/dx resolutions for Pb+Pb collisions are shown in Fig. 2.11 (upper and lower panels, respectively). The obtained resolutions are well within the theoretical expectations.

- **ITS**

As said in the previous section, the track finding in the ITS starts with the TPC-ITS matching. This is a quite complicate step to be performed, since the distance between the TPC and the ITS is rather large, and the track density in the ITS so high that a simple continuation of the track-finding procedure applied in the TPC will be ineffective. In this case, since the probability of assigning a wrong hit to the track is high if using just the criterion of minimal χ^2, a few modifications of the Kalman filter procedure have been implemented (see [76] for more details). Notice that the efficiency of the reconstruction in the ITS is not so high as that in the TPC.

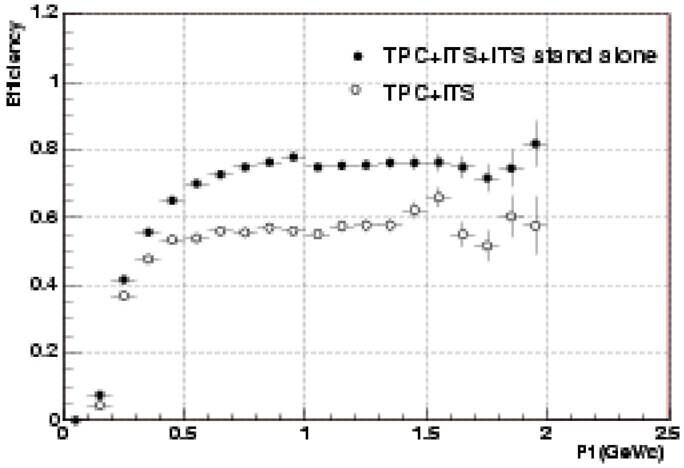

Figure 2.13: Comparison between the efficiency (as a function of the transverse momentum) obtained with and without the ITS stand-alone procedure for central Pb+Pb collisions ($dN_{ch}/d\eta = 6000$).

The combined TPC+ITS track-finding efficiency as a function of momentum is shown in Fig. 2.12 (see [76] for the definition of the efficiency).

As already said, for the tracks which cannot be reconstructed by the TPC (in other words, high-momentum tracks falling entirely inside the dead zones between the TPC sectors, or decaying between the TPC and the ITS, and low-momentum tracks with $p_T < 100$ MeV/c), an ITS stand-alone track finding algorithm has been developed. Figure 2.13 shows the reconstruction efficiency when including the ITS stand-alone procedure, compared with the main TPC+ITS algorithm. As can be seen, the stand-alone track finding reconstructs about 10% more tracks with respect to the results obtained by the main TPC+ITS procedure.

- **TRD**

  The TRD track finding algorithm is fully described in [76]. It is based on the Kalman filter approach, propagating a track from the outer radius of the TPC, to the outer layer of the TRD. As for the other detectors, at each extrapolation step, the track parameters and the covariance matrix are re-evaluated and updated with the information about the expected multiple scattering and energy loss.

  In the case of the TRD, the energy loss due to the interaction with the material is considerable high, being easily at the level of 10%. This implies that after corrections have been applied to those tracks crossing a large amount of material in order to take into account the energy loss effects, a rather high uncertainty in the track reconstructed momentum remains, which is even larger than that after the only TPC+ITS reconstruction. As a consequence, the final refitting backward is performed in a slightly different way for tracks which have lost a lot of energy and for those which have not. Besides, to improve the space and momentum resolution and track-finding efficiency, several parameters (such as the drift velocity) have to be tuned, depending on the hit position. In fact, since a precise correction for these parameters is unpracticable (because of the very loose precision on the track space coordinate z which is essential here), indicative values are used.

It is worth to say that every detector, if contributing to the reconstruction of a track, improves the reconstruction quality of this track. The requirement of being reconstructed in all the detectors (as many as possible, in fact) reduces the statistics of such tracks. So, while the overall algorithmic efficiency stays quite high ($\sim 90\%$ for almost the whole momentum range taken into account), the physical efficiency depends more on the number of detectors taken into account (see Fig. 2.14, upper panel), since it is strongly affected by particle decays, and by the presence of dead zones and interactions with the material. As can be seen from Fig. 2.14, the most considerable loss of efficiency occurs in the TRD where the material budget is the highest. Nevertheless, the TRD is crucial for electron identification, and improves the resolution of both transverse momentum (see Fig. 2.3) and azimuthal angle (see Fig. 2.14, lower panel).

2.2.2 Single-Detector Charged Particle Identification

The ALICE experiment will be able to identify charged particles in a wide momentum range, from 0.1 GeV/c up to a few GeV/c (and even more, up to a few tens of GeV/c thanks to the TPC dE/dx measurements in the relativistic region [76]). This will be possible taking advantage of the particle identification (PID) capabilities of the ALICE different detectors each of which plays a role in this sense in some narrower momentum range, complementary one to the others. Moreover, when some tracks are reconstructed simultaneously by different detectors, then a dedicated particle identification procedure can be applied, in order to combine all the available PID information.

In this section, the particle identification procedure and performance in the central detectors (ITS, TPC, TRD, TOF, HMPID) for charged particles will be presented, paying particular attention to the TOF tracking and PID procedure, since it is the result of an extensive study carried out for this thesis. Results concerning neutral particle identification can be found in [76].

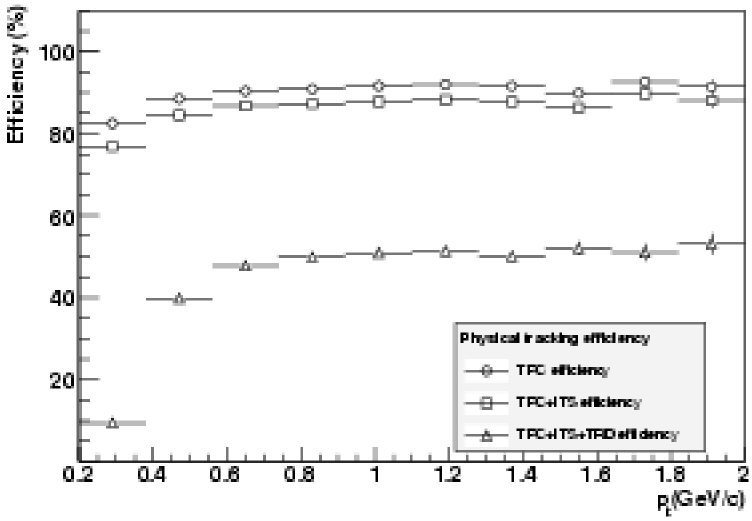

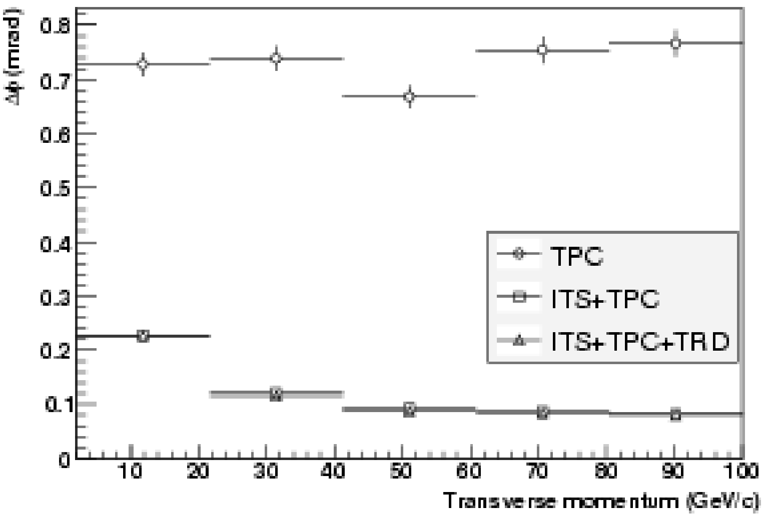

Figure 2.14: Top: Physical efficiency, bottom: azimuthal angle resolution as a function of p_T for different combinations of tracking detectors. The results refer to central Pb+Pb collisions ($dN_{ch}/d\eta = 6000$).

ITS

The ITS detector will provide particle identification in the non-relativistic region via the dE/dx measurements coming from the two-silicon-strip and the two-drift detector layers. The ITS PID information can be combined with that from the other detectors, but for

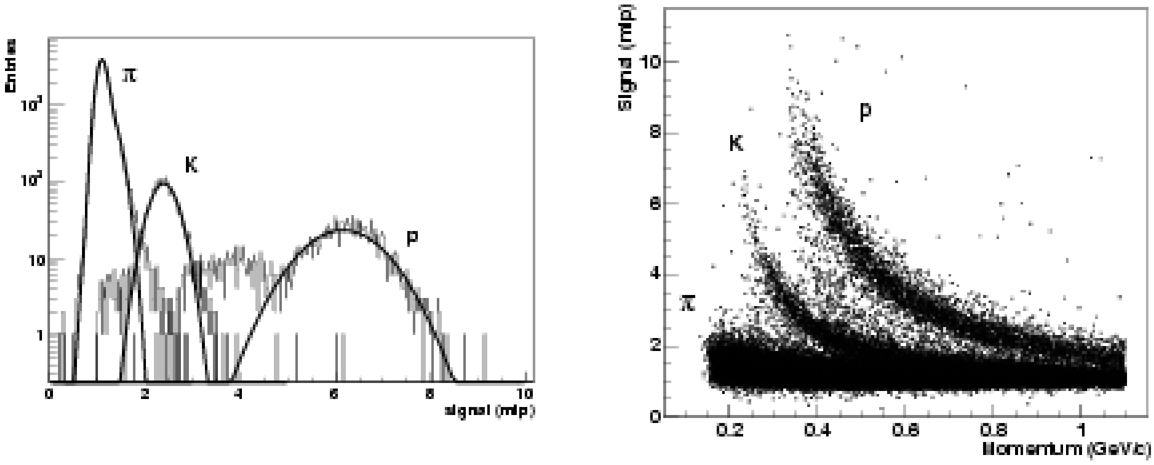

Figure 2.15: Left: Distributions of the truncated mean SDD and SSD signals in the ITS detector (mip units) obtained with the HIJING generator for pions, kaons and protons at the reconstructed momentum $400 < p < 425$ MeV/c (250 events). The curves are results of Gaussian approximations. Right: Signal-momentum correlation for the same particles as those used for the left panel. The momentum is that obtained from the TPC+ITS tracking.

low momentum particles and for those which have not been reconstructed in the TPC it is the only source of particle identification. Details on the updated version of the ITS simulation and reconstruction software can be found in [76].

The left panel in Fig. 2.15 shows the truncated mean dE/dx (considering two or three out of four dE/dx measurements) calculated for reconstructed tracks with momentum $400 < p < 425$ MeV/c in 250 HIJING events with a magnetic field $B = 0.4$ T. The right panel of the same Fig. shows the signal-momentum correlation for the same tracks (gamma conversions and other secondary particles are included). A clear distinction between different particle species can be observed. The curves in Fig. 2.15, left, are Gaussian approximation functions which are used to obtain the PID probabilities for each type of particle. In particular, the PID probability for each particle type for a given signal is the ratio g_i/G_s, where g_i is the Gaussian value for particle type i and G_s is a sum of the Gaussian values for all particle types.

Figure 2.16 shows the momentum dependence of the PID efficiency ε and contamination C for π, K, and p, defined as follows:

$$\varepsilon = \frac{N^{i}_{id}}{N}, \qquad C = \frac{N^{\bar{i}}_{id}}{N^{i+\bar{i}}_{id}}, \tag{2.9}$$

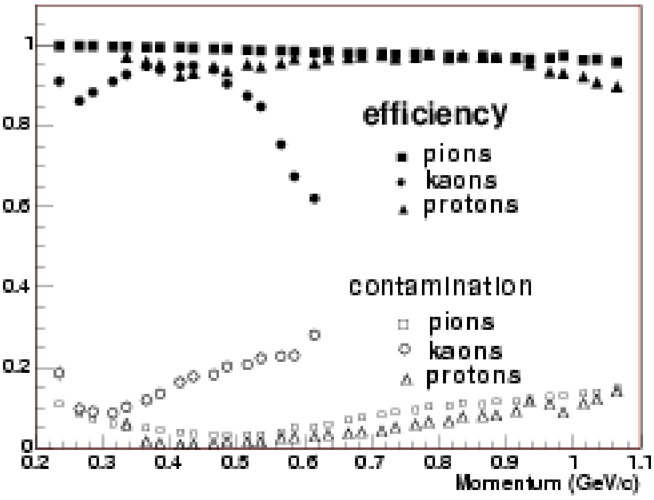

Figure 2.16: Momentum dependence of the PID efficiencies and contaminations for pions, kaons, and protons (250 HIJING events) in the ITS.

where N_{id} is the number of identified particles (the superscript "t" stands for correctly identified, "w" for uncorrectly identified, and "t+w" is the whole identified particle sample), and N is the total number of particles to which the PID procedure has been applied. The identity of the particle has been assigned according to the maximum probability among the g_i/G_ss. As one can see, the level of the efficiency for pions is $\sim 100\%$ for the whole momentum interval, and is very high even for kaons and protons for which it stays above the 90% in the momentum regions $0.35 < p < 0.50$ GeV/c and $0.35 < p < 0.90$ GeV/c. On the other hand, the contamination for pions is at the level of $\sim 10\%$, while for kaons and protons it remains $\sim 10 \div 20\%$ and $\sim 2 \div 10\%$ respectively, in the same momentum regions defined for the efficiency. The strong decrease of the kaon efficiency at lower momenta is mainly due to reconstruction problems, which affect the proton efficiency as well. This effect is also visible in the additional contamination of protons by kaons, and of kaons by pions in the range $p < 0.3$ GeV/c. The main contamination to pions comes, in this region, from electrons and muons that cannot be identified via dE/dx measurements. Moreover, at $p > 0.5$ GeV/c, the pions and kaons bands overlap (see the right panel of Fig. 2.15), but the pions are still identified with a high efficiency because they are the most abundantly produced type of particle. An improved procedure meant to increase the efficiency is currently under study [76].

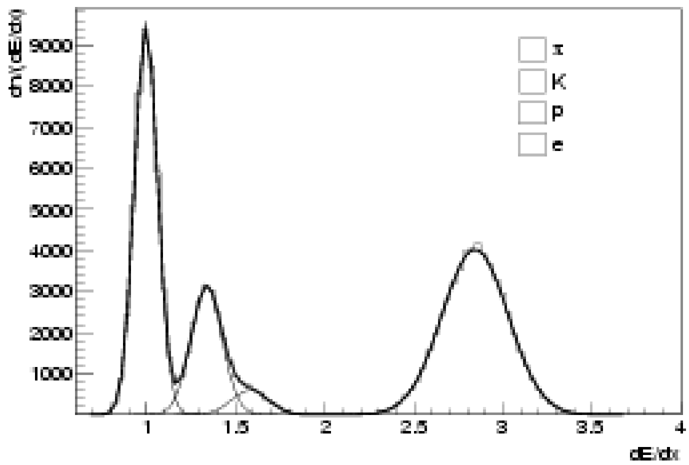

Figure 2.17: Monte Carlo simulated dE/dx distributions for electrons, pions, kaons and protons with $p = 0.5$ GeV/c in the TPC. The solid line indicates the result of the fit to a sum of four Gaussians. The shaded areas correspond to the contributions from different particle species.

TPC

The TPC detector identifies particles combining energy loss measurements and momentum information. While traversing a medium (in particular a gas), a particle ionizes it, and as a consequence, loses energy according to its velocity β, as the Bethe-Bloch formula states:

$$\langle dE/dx \rangle = (C_1/\beta^2)\left(\ln(C_2\beta^2\gamma^2) - \beta^2 + C_3\right),$$

where dE/dx is the amount of ionization per path length, $\gamma = 1/\sqrt{1-\beta^2}$, and C_1, C_2 and C_3 are some detector specific constants. As already shown in the right panel of Fig. 2.11, the mean value of the energy loss at a given momentum is Gaussian with the standard deviation (and, consequently, the resolution) determined by the detector properties and the quality of the reconstructed track. In particular, in the case of central Pb+Pb collisions, the resolution is of the order of $\sim$ 6.5%, decreasing to $\sim$ 5.5% for peripheral events.

Figure 2.17 shows a Monte Carlo dE/dx distribution simulated assuming a resolution of 6.5%. Fitting the sum of four (one for each type of particle) Gaussian functions to this distribution allows one to extract contributions from the individual particle types. The separation power between particle types A and B is defined as the distance of the mean

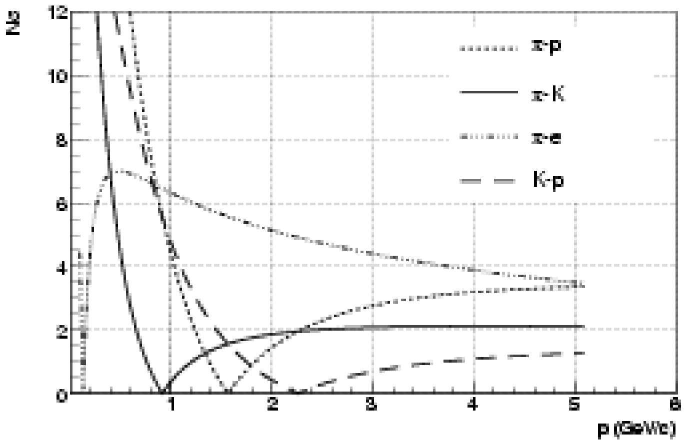

Figure 2.18: Momentum dependence of the $\langle dE/dx \rangle$ separation in the TPC for the most important particle combinations in units of energy loss resolution, assuming $\sigma = 6.5\%$.

energy loss values in units of relative resolution, that is:

$$N\sigma_{\mathrm{A,B}} = \frac{\langle dE/dx \rangle_{\mathrm{A}} - \langle dE/dx \rangle_{\mathrm{B}}}{(\sigma_{\mathrm{A}} + \sigma_{\mathrm{B}})/2}.$$

It is shown in Fig. 2.18 as a function of the particle momentum, for π/K, K/p, π/p and π/e separations. At the momentum ranges where the separation power becomes too small, then the PID information from other detecting systems is required.

After having determined the resolution and the mean ionization at a given momentum, the probability to be a particle of a given identity can be calculated using a Bayesian approach.

TRD

The particle identification role of the TRD detector is mainly to supplement the TPC electron/pion identification at momenta $p > 1$ GeV/c. In addition to this, the TRD will improve the identification of other charged particles thanks to dE/dx measurements. The PID procedure adopted by the TRD detector for electron/pion separation is the likelihood method, using the integrated energy deposit as detector signal. Figure 2.19 shows the pion efficiency as a function of the electron efficiency. As one can see, for 90% electron efficiency (which is a baseline value), a pion efficency down to 1% (pion suppression by a factor 100) can be achieved.

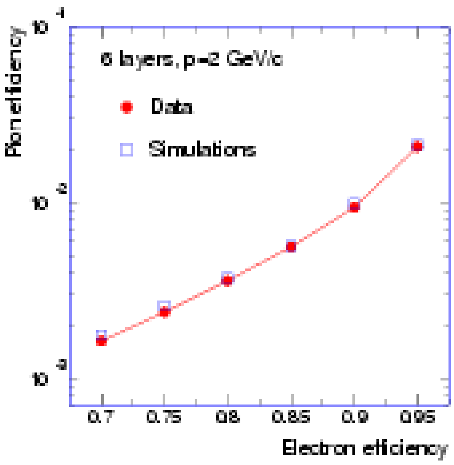

Figure 2.19: Pion efficiency as a function of electron efficiency for momentum $p = 2$ GeV/c in the TRD. The values corresponding to measured data are compared to simulations. The "six layers" label refers to the number of layers used in the likelihood method applied (see [76] for details).

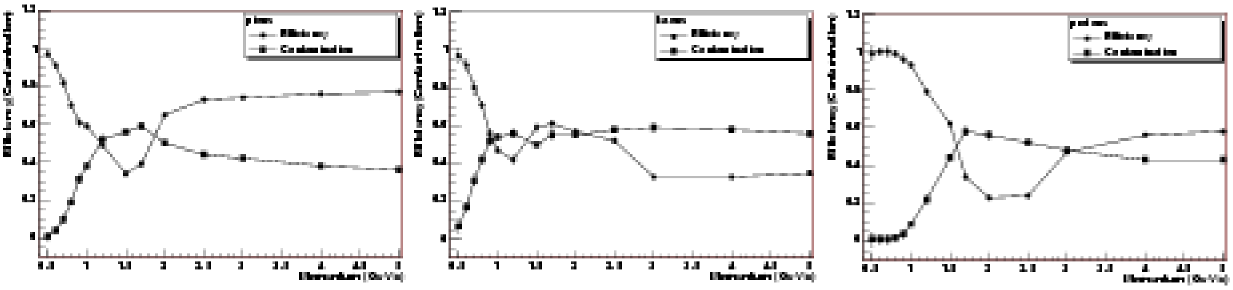

Figure 2.20: PID efficiencies and contaminations as a function of momentum for pions, kaons and protons as obtained by the TRD.

The TRD detector can also provide hadron identification via dE/dx measurements, in a way similar to that implemented by the ITS and TPC detectors. In the case of hadrons, the PID algorithm is quite different from that applied for electrons, using a combined PID probability over the six layers of which the TRD is made up of. In Figure 2.20 the efficiencies and contaminations for the TRD algorithm for π, K, and p are shown (efficiency and contamination are defined in the same way as those for the ITS detector, see Eq. 2.9).

TOF

In this section, the particle identification procedure applied by the TOF detector will be described. The details of the algorithm for the matching of the reconstructed tracks with the time signals measured in the Time Of Flight detector will be provided, as well as an exhaustive description of the PID performance of the detector. The considerable attention which will be paid to the TOF reconstruction and PID is due to the fact that the results which are going to be presented herein derive from an intensive software development which has gone on during these years.

Monte Carlo Sample and Detector Simulation

The Monte Carlo event sample has been generated with the HIJING 1.36 generator program [78]. It consists of 200 central Pb+Pb collisions with impact parameter b in the range $0 < b < 5$ fm. The results concerning more peripheral collisions as well as on p+p events can be found in [76].

Particle tracking, signal generation and detector response have been simulated with GEANT3 [83]. The geometry of the TOF detector used in the simulation is the same as that described in [71], except for the fact that in the five TOF azimuthal sectors covering the region $220° \leq \varphi \leq 320°$, the central modules have been removed to minimize the amount of material in front of the HMPID detector.

Particle signals at the GEANT level have been digitized according to a Gaussian time response. Border effects, like the sharing of the particle signal between neighbouring pads and the dependence of the MRPC time resolution on the impact point of the particle within a pad, have been parametrized according to test beam results and have been included in the simulations as described in [84]. The overall TOF time resolution assumed in this simulation ($\sigma_{\rm TOF} = 80$ ps) is the (quadratic) sum of different uncertainty contributions, among which the detector intrinsic resolution ($\sigma_{\rm MRPC} = 40$ ps), the channel-to-channel calibration uncertainty ($\sigma_{\rm Cal} = 30$ ps, see Sec. 4.1), and the uncertainty on the determination of the time of the collision ($\sigma_{\rm T0} = 50$ ps, see Sec. 4.1). For more details, see [76].

Track-TOF signal matching

The starting sample for the track-TOF signal matching procedure consists of all TPC tracks which can be successfully extrapolated from the TPC outer wall (at a radius $R \sim 2.6$ m) to the TOF inner radius ($R \sim 3.7$ m). Track extrapolation to the TOF is performed by

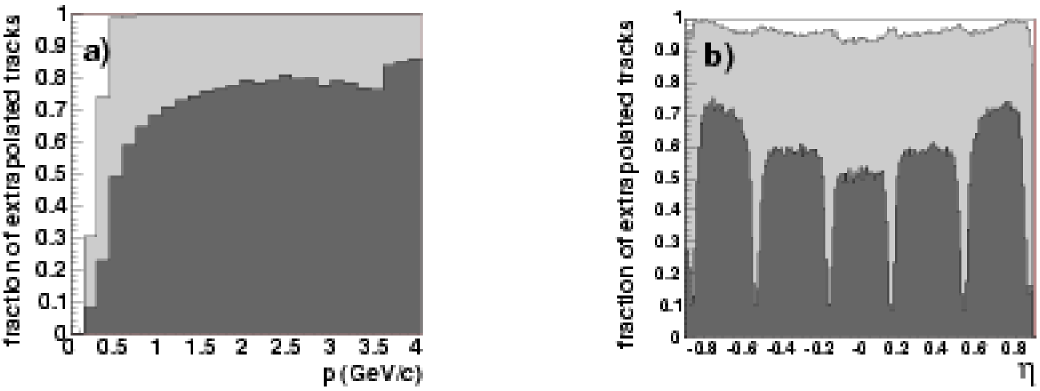

Figure 2.21: Momentum (a) and pseudorapidity (b) dependence of the fraction of TPC tracks releasing a signal on TOF which are extrapolated to the TOF inner radius by the TRD tracking algorithm (dark-shaded histograms), and by the additional propagation step (light-shaded histograms).

the reconstruction procedure in the TRD detector. By the way, as a consequence of very strict quality criteria applied during the TRD track reconstruction (in the TRD, a large amount of passive material is crossed, making the track propagation often fail), many tracks are stopped before reaching the TOF, even if they do release a signal on TOF. Since this would imply a significant loss of efficiency in the TOF PID procedure, a further extrapolation step is applied during the TOF reconstruction to those tracks stopped by the TRD. In this second step, instead of a detailed description, average values of the density and the radiation length of the material crossed by the tracks are used. In this way, the energy loss and multiple scattering occurring in the TRD are still taken into account. As can be seen in Figure 2.21, a large amount of tracks are recovered, with the $\sim$ 100% of the TPC tracks which have released a signal on TOF eventually included in the initial sample of the TOF tracking algorithm. In this way, the association efficiency increases of a factor $\sim 1.3 \div 2$ (depending on the momentum), while contamination worsens only by a factor ~ 1.1.

After extrapolation to the TOF inner radius, the tracks are sorted according to their curvature, in such a way that the highest momentum tracks are associated first. In this way, the contamination due to fake tracks is reduced. Then, a window in $[d\varphi, dz]$ is opened for each track, the width of which depends on the track parameters and their errors. Inside this window, the TOF pads which have given a signal are searched for in order to be preselected as candidates for the association. The matching procedure is then performed as follows:

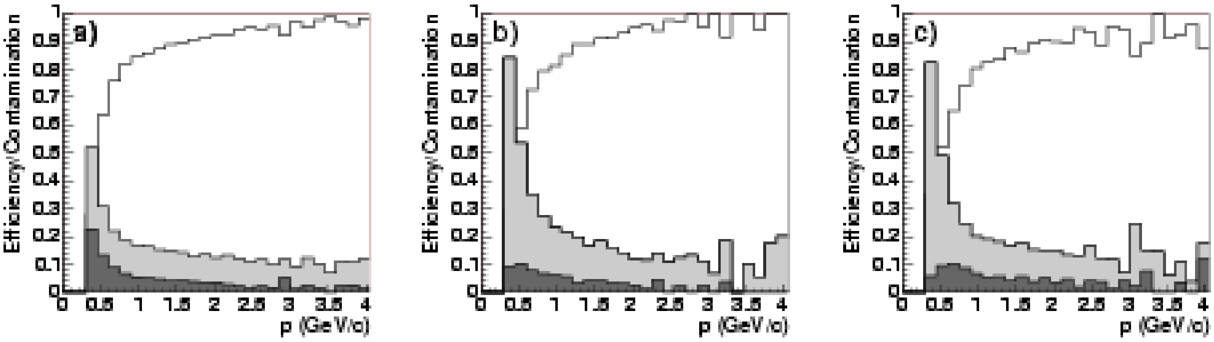

Figure 2.22: Momentum dependence of the efficiency (empty histograms) and contamination (shaded histograms) of the TOF matching procedure in Pb+Pb central events, for primary particles of different species ((a): pions, (b): kaons, (c): protons). The contamination contributions coming from tracks having and not having released a signal on TOF are splitted and shown as dark- and light-shaded histograms (respectively).

- First, each track is propagated through the TOF detector, until its extrapolation crosses one of the preselected pads. The time signal of this pad is then associated to the track.

- Second, the same procedure as before is applied to those tracks the extrapolation of which did not fall within the active area of any of the preselected TOF pads, but in this case a looser criterion is adopted. In particular, the TOF signal closest to the track trajectory is associated, provided that its distance is smaller than a predefined value, $d_{max} = 3$ cm. This value is such to optimize the ratio between the matching efficiency and contamination, and is appropriately tuned according to the type of events under study.

Once a TOF signal is associated to a track, it is then flagged in order to prevent any further association to other tracks, to avoid ambiguous track-time assignments.

The performance of the association algorithm is shown in Figure 2.22 for primary pions, kaons and protons in terms of the momentum dependence of the efficiency ε^{m} and contamination C^{m}defined as

$$\varepsilon^{m} = \frac{N_{m,t}}{N_{reco,TOF}}, \qquad C^{m} = \frac{N_{m,f}}{N_{m,t} + N_{m,f}}.$$

Here, $N_{reco,TOF}$ is the number of TPC reconstructed tracks which have released a signal on

TOF, and $N_{m,t}$ and $N_{m,w}$ are the number of tracks associated with the correct TOF signal and with a signal coming from a different particle, respectively. As one can see, for all the three particle species the matching efficiency increases with increasing momentum, as a consequence of a decreasing multiple scattering effect. For what concerns contamination, two different contributions can be identified, as shown in Fig. 2.22. The main source of mis-association is due to the tracks which did not reach the TOF because of interactions with the materials (or, in the case of kaons, because of decays), but which, in any case, have been extrapolated to the TOF sensitive volume. For these tracks, the subsequent association is then done with an uncorrelated TOF signal. The other contamination component derives from tracks which, in fact, have reached the TOF and have released a signal, but are then associated to a signal coming from another particle, because an incorrect extrapolation was performed. It is worth to say that when a track is wrongly associated to a signal generated by one of its secondaries (which corresponds to the $\sim 10\%$ of the cases contributing to contamination), nevertheless the TOF PID procedure will identify it in a correct way, since the measured time and the calculated time used for the PID procedure are still correlated.

Figure 2.23 shows the performance of the TOF matching algorithm in terms of the fraction of primary pions, kaons and protons generated in the range $|\theta - 90°| < 45°$ which have been associated with the correct (light-shaded histograms) or wrong (dark-shaded histograms) TOF signal. As a reference, the fraction of primaries which reach the TOF sensitive volume and release a hit on the detector (empty histogram) is also shown. A loss in the TOF acceptance can be observed, as a consequence of the TOF dead space ($\sim 15\%$ of the total acceptance), of the interactions of particles with the material in front of the TOF (mostly the TRD) and of particle decays (especially for kaons). To be noted that the momentum threshold for particles to reach the TOF is strictly related to the magnetic field: for $B = 0.5$ T, then $p_{min} \sim 300, 350, 450$ MeV/c for pions, kaons and protons respectively.

Results concerning the performance of the algorithm in case of lower track densities (dN_{ch}/dy) and of p+p collisions are reported in [76].

Particle Identification

After the track-TOF signal matching algorithm has been applied, the TOF particle identification procedure is performed to all the tracks that have been associated to a signal on the TOF system. Figure 2.24 is a representation of the TOF PID capabilities, showing, for all the reconstructed tracks matched with a signal on TOF, the correlation between

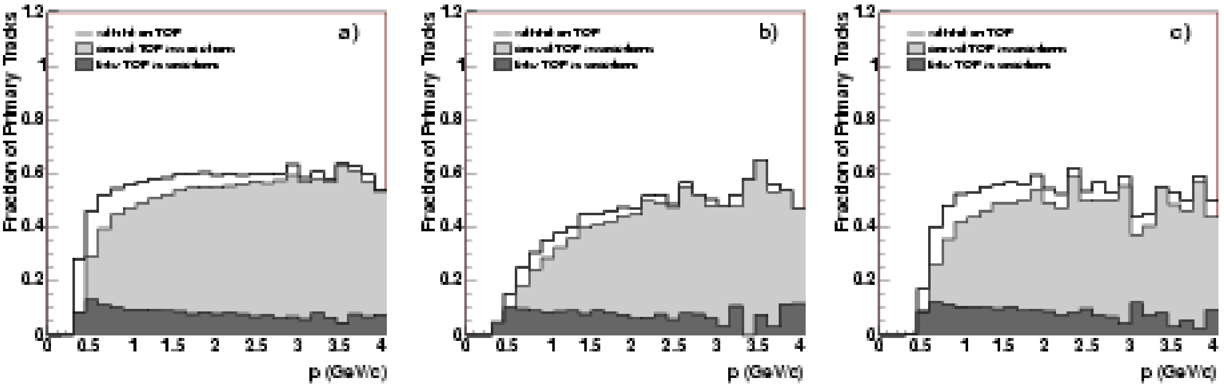

Figure 2.23: Fractions of primary pions (a), kaons (b), protons (c) generated in the angular region $|\theta - 90°| < 45°$, associated to a correct (light-shaded histograms) and incorrect (dark-shaded histograms) signal on TOF, in central Pb+Pb collisions. The empy histograms indicate the fraction of primary particles which reach the TOF sensitive volume and produce a hit on the detector.

the track momentum and the mass:

$$M = \frac{p}{\beta\gamma} = p\sqrt{\frac{\left(ct^{\mathrm{TOF}}\right)^2}{l^2} - 1} \tag{2.10}$$

calculated from the measured time-of-flight t^{TOF}, the reconstructed track length l, and the track momentum p.

The TOF particle identification procedure relies on the Bayesian approach. The measured time-of-flight t^{TOF} is chosen as the PID discriminating variable, and the Gaussian

$$g_i\left(t^{\mathrm{TOF}}\right) \sim \frac{1}{\sigma}\exp\left\{-\left(t^{\mathrm{TOF}} - t_i^{\mathrm{exp}}\right)^2/2\sigma^2\right\}$$

is used as the TOF "detector response function" for different mass hypotheses m_i (i = e, μ, π, K, p)[3]. Besides the measured time-of-flight, the response function g_i depends on other two parameters, the expected time-of-flight t_i^{exp} for the i-th mass hypothesis, and the overall time resolution σ[4].

[3] In the case of Pb+Pb collisions, particle identification has been applied only for pions, kaons and protons, since in these collisions an exceedingly high background is expected for electrons.

[4] The overall time-of-flight resolution σ takes into account both the time resolution of the TOF system σ_{TOF} and the uncertainty σ_{reco} related to the reconstructed momentum and track length:

$$\sigma = \sqrt{\sigma^2_{\mathrm{TOF}} + \sigma^2_{\mathrm{reco}}}.$$

To be noted that $\sigma_{\mathrm{reco}} \sim 30$ ps depends on the track momentum and track length [85].

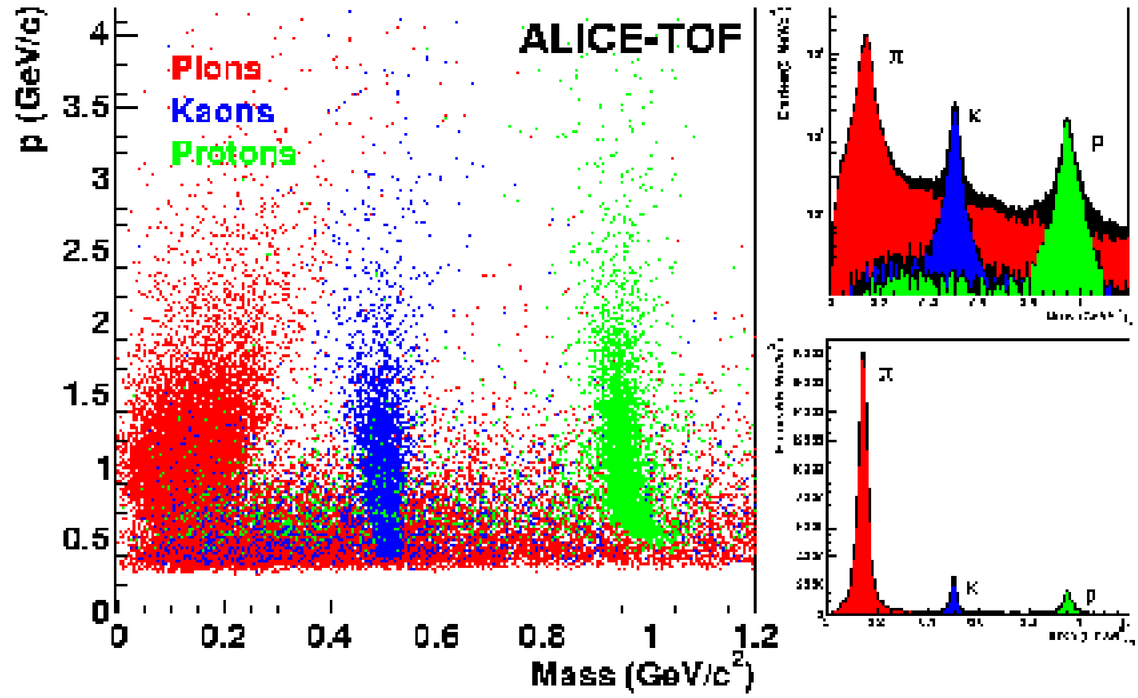

Figure 2.24: Mass separation as a function of momentum as obtained with the Time Of Flight detector in Pb+Pb central collisions.

The expected time-of-flight is calculated during track reconstruction summing up at each tracking step the time-of-flight increment:

$$\Delta t_k = \frac{\sqrt{p_k^2 + m_i^2}}{p_k} \Delta l_k, \tag{2.11}$$

p_k being the local estimate of the track momentum, and Δl_k the track length increment along the trajectory. For more details on the calculation of t_i^{exp} see [85].

On the basis of g_i, the conditional probability $P_i(t_i^{TOF})$ to be a particle of type i is then assigned to each track, weighting g_i by the *a priori* probability C_i for a track to be an i-particle[5]:

$$P_i(t^{TOF}) = \frac{C_i g_i(t^{TOF})}{C_e g_e(t^{TOF}) + C_\mu g_\mu(t^{TOF}) + C_\pi g_\pi(t^{TOF}) + C_K g_K(t^{TOF}) + C_p g_p(t^{TOF})},$$

[5]For the results presented here, the probabilities $C_\pi = 0.85$, $C_K = 0.10$, $C_p = 0.05$, $C_{e,\mu} = 0.01$ have been assumed, which are close to the standard particle yield levels of the HIJING Monte Carlo generator.

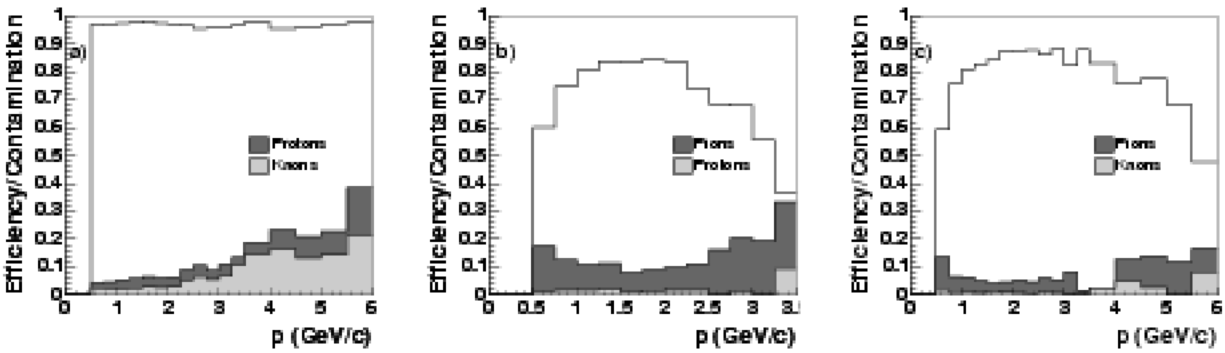

Figure 2.25: Momentum dependence of the efficiency (empty histograms) and contamination (shaded histograms) of the TOF PID procedure in Pb+Pb central events, for primary particles of different species ((a): pions, (b): kaons, (c): protons). The dark/light-shaded histograms are aimed at distinguishing the contamination to each particle specie coming from the others.

with i = e, μ, π, K, p. Eventually, the identity of the track is defined by the highest among the P_i's probabilities.

The performance of the TOF PID procedure can be described in terms of efficiency $\varepsilon^{\rm PID}$ and contamination $C^{\rm PID}$, defined as:

$$\varepsilon^{\rm PID}(i) = \frac{N^{+}_{\rm id}(i)}{N(i)}, \qquad C^{\rm PID}(i) = \frac{N^{-}_{\rm id}(i)}{N^{+}_{\rm id}(i) + N^{-}_{\rm id}(i)}, \tag{2.12}$$

$N(i)$ being the number of particles of type i ($i = \pi$, K, p) associated with a signal on the TOF system, $N^{+}_{\rm id}(i)$ the number of i-particles correctly identified, and $N^{-}_{\rm id}(i)$ the number of non-i-particles mis-identified as particles of type i (see Eq. 2.9). As can be seen from Fig. 2.25, a very high ($> 95\%$) identification efficiency can be obtained for pions, almost constant over the whole momentum range $0.5 < p < 6$ GeV/c, while kaons and protons show a slightly worse and momentum-dependent performance (at most 85%). At low momenta, the particle identification for kaons and protons suffers from track-TOF signal mis-associations (and decays, for kaons), while at high momenta the results are affected by the decrease of the K/π and K/p separation power (pions are less sensitive to these effects, since they are the most abundant particle type). On the other hand, the PID contamination varies from a few percents to $\sim 30\%$ and to $\sim 15\%$ for pions and protons (respectively) in the momentum range $0.5 < p < 6$ GeV/c, while for kaons, it ranges from 20% up to 10% (mostly from pions, as in the case of proton contamination), for momenta $0.5 < p < 3$ GeV/c. Analogously to what happens for efficiency, the main

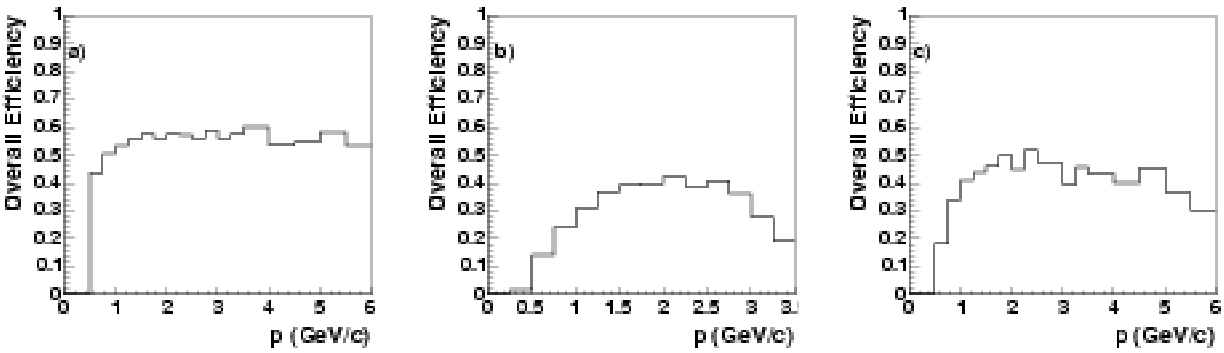

Figure 2.26: Momentum dependence of the overall efficiency of the TOF PID procedure for primary particles of different species generated in the region $|\theta - 90°| < 45°$ ((a): pions, (b): kaons, (c): protons).

contribution to contamination in the low momentum region comes from track-TOF signal mis-associations, while at high momenta the time-of-flight separation power plays a crucial role.

Figure 2.26 shows the corresponding overall TOF PID efficiencies with respect to primary tracks generated in the $|\theta - 90°| < 45°$ region. Here, the track reconstruction efficiency, the effect of the TOF dead zones, the losses due to particle decays and interactions affect the PID efficiency itself.

It should be pointed out that the results presented here, especially for what concerns PID contamination, are strongly influenced by the relative particle concentrations adopted, and may vary significantly at LHC. In particular, if the production rates of pions, kaons and protons become comparable at momenta ≥ 1.5 GeV/c, as currently suggested by RHIC results [86], then a substantial improvement in the kaon contamination will be expected.

Results concerning the dependence of the TOF PID procedure on the time resolution of the TOF system are reported in [76], as well as those concerning the track-density and centrality dependence.

HMPID

Hadron identification in the high momentum range ($1 < p_T < 3$ GeV/c for π and K, and $1 < p_T < 5$ GeV/c for p) will be provided in ALICE by the HMPID detector.

The identification in the HMPID starts from tracks extrapolated from the central detectors (ITS, TPC, TRD, TOF) and consists in an association between a track and a mip cluster (see [87] for details). During reconstruction, the inclination angle θ_C with which each track impacts on the HMPID detector has to be determined with high precision, since it is crucial for the reconstruction of the Cherenkov ring, and, as a consequence, for the particle identification itself. The efficiency and contamination for the HMPID reconstruction are shown in Fig. 2.27 as a function of momentum. The loss of efficiency at high momenta is mainly due to multiple scattering effects.

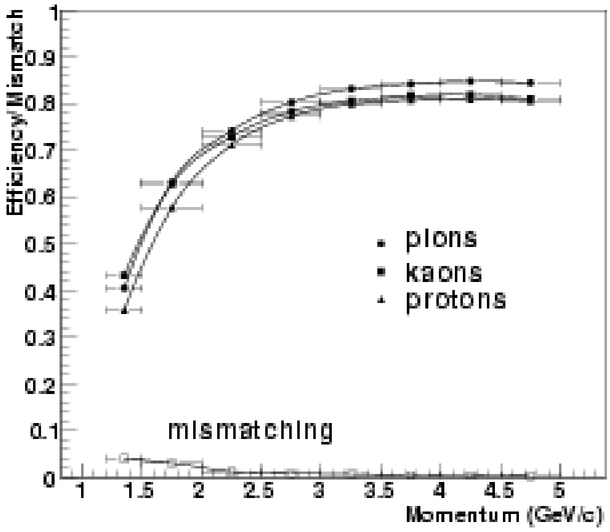

Figure 2.27: Track-mip cluster matching efficiency (full quares) and probability of mismatching (open squares) as a function of momentum for pions, kaons, and protons in the HMPID.

After having reconstructed the Cherenkov pattern using an improved version of the Hough Transformation Method (HTM) [88], the probability that a given reconstructed Cherenkov angle θ_C belongs to the probability density function of the i-particle ($i = \pi$, K, p), falling in the range $[\theta, \theta + \mathrm{d}\theta]$, is

$$P(\theta_C)\mathrm{d}\theta = \mathrm{Gauss}(\theta_C, \sigma_{\theta_{C,i}})\mathrm{d}\theta,$$

where $\theta_{C,i}$ can be obtained from the response function of the detector. Then, the probability that a given particle with θ_C is of type $i = \pi$, K, p is:

$$P_i = \frac{\mathrm{Gauss}(\theta_C, \sigma_{\theta_{C,i}})}{\sum_{i=\pi,\mathrm{K},\mathrm{p}} \mathrm{Gauss}(\theta_C, \sigma_{\theta_{C,i}})}.$$

The reconstructed Cherenkov angle as a function of the track momentum is shown in Fig. 2.28, where the bands corresponding to pions (upper), kaons (middle) and protons (lower) can be observed. The efficiency ε and contamination C of the HMPID particle identification procedure are shown in Fig. 2.29 following the definitions:

$$\varepsilon(i) = \frac{N_i^{\mathrm{found}}}{N_i^{\mathrm{tot}}}, \qquad C(i) = \frac{N_j^{\mathrm{found}} + N_k^{\mathrm{found}}}{N_i^{\mathrm{found}} + N_j^{\mathrm{found}} + N_k^{\mathrm{found}}}, \qquad i \neq j \neq k \; (i = \pi, \mathrm{K}, \mathrm{p}),$$

where N_i^{found} is the number of reconstructed rings with Cherenkov angle in a selected range, while N_i^{tot} is the number of total simulated rings, for i-type particle. For more details, see [76].

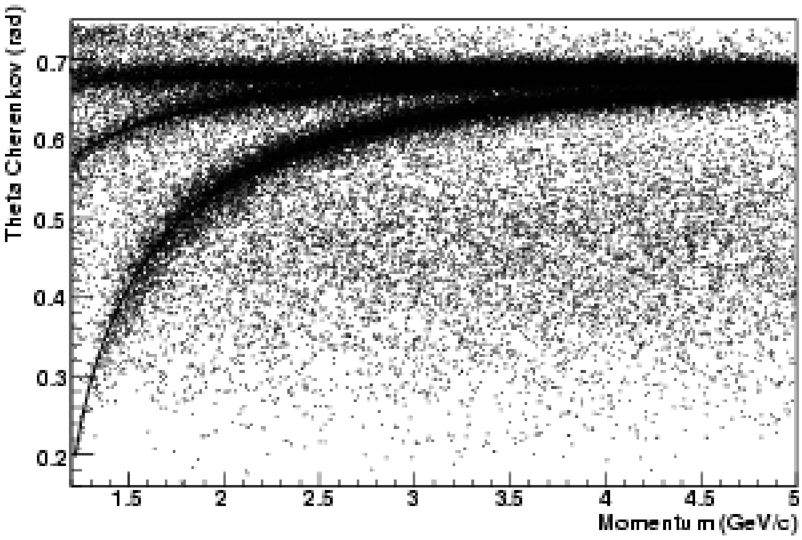

Figure 2.28: Reconstructed Cherenkov angle in the HMPID detector as a function of the track momentum. Equal concentrations for pions, kaons, and protons have been set (HIJING events, $dN_{ch}/dy = 6000$). Solid lines indicate the predicted curves for pions (upper), kaons (middle), and protons (lower).

2.2.3 Combined Particle Identification

Since a combined particle identification approach implies that PID information of different nature, coming from different detectors, have to be dealt with at the same time, the particle identification procedure should be as automatic as possible. Moreover, it should be able to combine signals distributed according to quite different probability density functions. The Bayesian approach is able to satisfy these requirements.

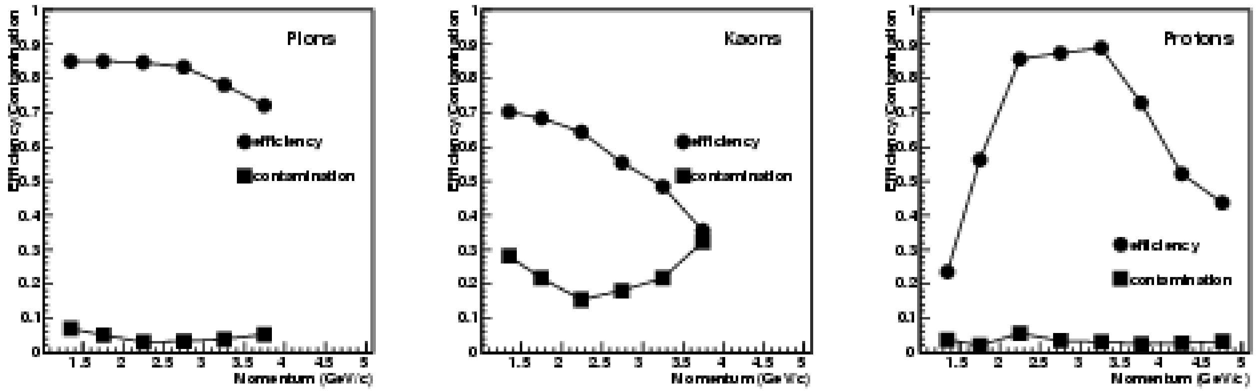

Figure 2.29: PID efficiency and contamination for pions, kaons and protons as a function of momentum in the HMPID.

Bayesian PID with a Single Detector

Let $r(s|i)$ be a conditional probability density function to observe in some detector a PID signal s if a i-type particle is detected ($i = e, \mu, \pi, K, p...$). Then, the probability $w(s|i)$ (often called PID weight) to be a particle of type i when a signal s is observed depends on $r(s|i)$, but also on how often this type of particle is observed in the expertiment, a sort of *a priori* probability C_i to find this particle. So, the Bayes relation can be written as:

$$w(i|s) = \frac{r(s|i)C_i}{\sum_{k=e,\mu,\pi...} r(s|k)C_k}. \tag{2.13}$$

If C_i and $r(s|i)$ are not correlated (which is a reasonable hypothesis), then the $r(s|i)$'s reflect only the detector properties (and for this reason they are called "detector response functions") and do not depend on any external conditions (either event or track selections). On the contrary, the "relative concentrations" C_i's do not depend on the detector properties, but reflect the external conditions.

The detector PID procedure first requires the determination of the detector response function, according to which a $r(s|i)$ value is then assigned to each track. The $r(s|i)$ function is usually parametrized with sufficient precision using available experimental data.

Then, the concentrations C_i's are estimated from a subset of events and tracks selected in a specific physics analysis. In the simplest approach, the C_i's can be assumed equal, but they can be determined more precisely using PID information coming from different detectors (for tracks identified simultaneously by these detectors, see [76] for more details). The absolute normalization of the C_i's is not important.

Finally, an array os probabilities $w(i|s)$'s can be calculated for each track within the selected subset.

Bayesian PID Combined over Several Detectors

The Bayesian approach can be used to calculate the combined PID over several detectors which all perform particle identification.

Let's consider the whole system of N detectors as a single "super-detector". Then the combined PID weights $W(i|\bar{s})$'s can be written as

$$W(i|\bar{s}) = \frac{R(\bar{s}|i)C_i}{\sum_{k=e,\mu,\pi\ldots} R(\bar{s}|k)C_k}$$

which is the analogous of Eq. 2.13. In this case, $\bar{s} = s_1, s_2, \ldots, s_N$ is a vector of PID signals detected by each of the N detectors, C_i's are the same *a priori* probabilities to be a particle of type i defined before, and $R(\bar{s}|i)$ is the combined response function of the whole system of detectors.

In particular, if the PID measurements s_j's are uncorrelated (as it is the case for the ALICE experiment), then the combined response function is the product of the single response functions:

$$R(\bar{s}|i)C_i = \prod_{j=1}^{N} r(s_j|i). \tag{2.14}$$

So, the PID weights combined over the whole system of detectors are given by the formula:

$$W(i|\bar{s}) = \frac{C_i \prod_{j=1}^{N} r(s_j|i)}{\sum_{k=e,\mu,\pi} C_k \prod_{j=1}^{N} r(s_j|k)}. \tag{2.15}$$

From the form of Eq. 2.15 it is possible to infer that if for a certain particle momentum one (or several) of the detectors is not able to perform particle identification (that is to say, the $r(s|i)$'s are equal for all the particle types), then its contribution cancels out. On the contrary, when several detectors are able to separate particle types, their contributions accumulate, providing an improved combined PID. Moreover, since the single-detector response functions $r(s|i)$'s can be obtained in advance during the calibration step and the combined response is given by Eq. 2.14, the calculation of $R(\bar{s}|i)$ can be done track-by-track "once and forever" by the reconstruction software, and the results can be stored.

The final PID decision, depending on the *a priori* probabilities C_i's which, in turn, reflect the event and track selection, is then postponed until the physics analysis of the data.

In ALICE, the PID procedure requires first the determination of the single-detector response functions $r(s|i)$ by the calibration software. Then, during reconstruction, for each reconstructed track, the combined PID response $R(\bar{s}|i)$ is calculated, and the effects of possible mis-measurements can be accounted for. The results are properly stored, and will then be used during physics analysis of the data. Finally, for each kind of physics analysis, the analysis software estimates the *a priori* probabilities C_i's according to the event and track selection done, and calculates the PID weights $W(i|\bar{s})$'s.

There are several advantages in chosing this approach to perform a combined PID. First, it takes into account that for different physics analyses, different PID procedures have to be applied (and this can be seen in the dependence of the C_i's from the event and track selection. Then, it allows to combine signals from detectors with quite different shapes of the PID response functions. Moreover, it is fully automatic, without requiring any multidimentional graphical cuts.

Combined PID in ALICE: Results

Defining the PID efficiency and contamination in the same way as in Eqs. 2.12, Fig. 2.30 shows the results of identifying charged kaons using the ITS, TPC and TOF as stand-alone detectors, as well as the performance of the combined PID procedure for central Pb+Pb events at $\sqrt{s_{NN}} = 5.5$ TeV. Only tracks reconstructed simultaneously in all the detectors have been used for the analysis. The values $C_e = 0$, $C_\mu = 0$, $C_\pi = 0.70$, $C_K = 0.15$, and $C_p = 0.15$, have been set.

As can be seen, combining the PID information from different detectors makes the PID efficiency dependence on the particle momentum significantly weaker. Moreover, the efficiency/contamination stays always higher/lower (or at least equal) with respect to the results obtained by any stand-alone detector PID procedure.

The inclusion of the TRD and HMPID detectors in the combined PID procedure is currently under study.

Since the choice of the C_i particle concentrations is arbitrary, the question on how much the algortihm is stable with respect to variations of the C_i's could arise. Anyway, detailed simulations have shown that the results of the combined PID over all the ALICE central detectors are stable within a few percents with respect to variations of the C_i's up to at least particle momentum of 3 GeV/c.

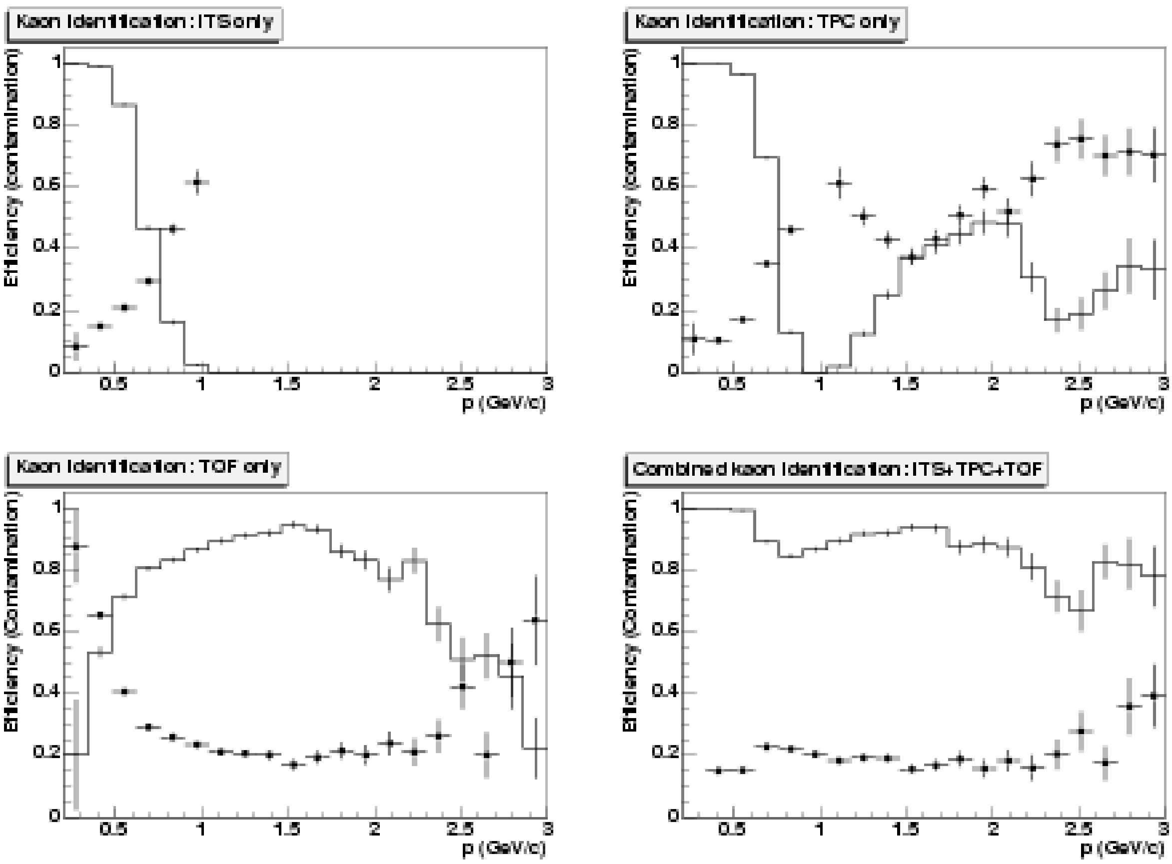

Figure 2.30: Momentum dependence of the single-detector efficiencies (solid line histograms) and contaminations (points with error bars) of the charged kaon identification with the ITS (upper left), TPC (upper right) and TOF (lower left). The combined PID performance in terms of efficiency and contamination as a function of momentum is also shown (lower right).

Chapter 3

Event By Event Physics in ALICE

3.1 ALICE Physics Program

The ALICE physics program will span over a wide number of observables in order to study the properties of the QCD matter and of the QGP state that will be likely formed during the very high-energy, heavy-ion collisions. Some of these observables are needed to characterize the global features of the state created during the collisions, in order to define some constraints for the theoretical models which should describe the evolution of the system (e.g. size, lifetime, density...). In this way, a specific QGP signal, or, at least, some indications of a new physics can be traced. Moreover, global event features can help to determine the initial geometry of the collision and to study how the initial available centre-of-mass energy is redistributed within the accessible phase-space. On the other hand, event characterization comes, for example, from studies on the centrality of the event, on charged-particle multiplicity and pseudo-rapidity distributions.

Observables more specifically related to the dynamic evolution of the hadronic phase, are for example, particle ratios and p_T distributions. Interferometry (HBT analysis) allows measurements of the freeze-out radius of the hadronic fireball and of the expansion time in the mixed phase. Anisotropic flow can help in understanding the dynamics of the collision. Open charm production will probe the parton kinematics at the very early stages of the collisions, while quarkonia studies will allow a very detailed study of both suppression phenomena (due to deconfinement, both for charm and beauty states) and enhancement (due to recombination, only for charmonium). The study of direct *prompt* photons at high p_T will be important to investigate hard processes in the dense medium without any final-state modification, while at low p_T, *thermal* photons trace the thermal evolution of the system and, in particular, of the hot and early phase of the reaction (lepton pair measurements will serve the same aim as direct photons). The energy loss experienced by fast partons in the medium (the so-called *jet quenching*) will provide information about the hot and dense medium created during the collision. Strangeness production is sensitive to the large s-quark production rate expected as a consequence of (partial) chiral symmetry restoration.

Besides all these observables which will be extensively studied by the ALICE experiment, event-by-event (E-by-E) physics is crucial to understand the physics of bulk properties of matter, as well as high p_T particles and jets. In particular, the capability of the ALICE detector will concentrate on the measurement of temperature and $\langle p_T \rangle$ fluctuations, fluctuations of conserved quantities, such as the net charge, fluctuations in azimuthal anisotropy and in space-time parameters (coming from correlation measurements). Moreover, it will study the disoriented chiral condensate (DCC) as a cause of fluctuations in the neutral to charged pion ratio, and the importance of jet and mini-jet production in fluctuation measurements and long-range dynamical correlations. Obviously, since the statistical uncertainty on a single event measurement is inversely proportional to the square root of the number of particles produced ($\sqrt{N}$), a large phase-space acceptance of the experiment as well as an extremely high multiplicity of produced particles os required. If in an "average collision" the collision energy is close to the critical energy at which the QGP is created, the E-by-E analysis can be used to separate plasma from non-plasma events [89]. A large multiplicity gives the possibility to:

- construct single-event spectra (and study the first momentum, as well as higher momenta of the distributions);

- determine single-event thermodynamical quantities, such as temperature, for a single event;

- use statistics tools as the Central Limit Theorem to study fluctuations of single-event properties in a model-independent way;

- select event sub-samples on a single-event basis for a subsequent "semi-inclusive" analysis.

ALICE, thanks to its extremely high (especially with respect to past experiments) particle multiplicity per event, to its unique capability to track the majority of the particles produced in a heavy-ion collision and to its highly performing particle identification system will be one of the most suitable experiments for event-by-event analysis.

3.2 Event-by-Event Fluctuations in Heavy-Ion Collisions

Fluctuations affect any physical quantity which can be measured in an experiment. In general, the nature, the entity and the origin of these fluctuations strongly depend on the system under study, and may carry important information about it. Moreover, analysis of fluctuations on an event-by-event basis can offer the opportunity to observe a very different physics than averaging over a large statistical sample of events. The E-by-E approach in the analysis of Hanbury-Brown-Twiss correlations, for example, is a common tool in nuclear physics to get information on the geometry of the system [55, 90]. On the other hand, relics of the early instants of the Universe are looked for via fluctuations in the cosmic microwave background radiation by experiments like WMAP [91] and PLANCK [92].

The study of event-by-event fluctuations in ultra-relativistic heavy-ion collisions has only recently developed. In particular, there are different classes of fluctuations which can be identified. First, there are *quantum* fluctuations, which occur when the specific observable does not commute with the Langrangian describing the system (such as the temporary change in the amount of energy in a point in space arising from Heisenberg's uncertainty principle, and from which a particle-antiparticle pair can originate). These are, in fact, of relatively poor importance for high-energy physics. Then, there are *statistical* or *trivial* fluctuations. These are due to the finiteness of the number of particles produced and observed, and used to define a particular observable in a given event (such as the mean transverse momentum and the ratios of multiplicities of the different particles produced). Finally, *dynamical* fluctuations are related to the properties of the system and, more specifically, to its dynamical evolution. Moreover, among these latter, a further distinction can be done, between those fluctuations which do not change from event to event (such as two-particle correlations), and those which occur only on an event-by-event basis, the so-called E-by-E fluctuations. Examples of these are fluctuations in the ratio of charged to neutral multiplicities due to the creation of regions of DCC, or the fluctuations in the anisotropic flow due to the presence of regions with "unusual" soft/hard equations of state.

Dynamical fluctuations are closely related to phase transitions, and for this reason they have been proposed as a powerful tool in high energy physics. They would shed light on the properties of the system created in the collision, and above all they would give evidence for the existence of a QGP phase transition, thus allowing to understand the QCD phase diagram itself.

As said in Chapter 1, according to QCD with two massless quarks, the phase transition at small baryon density is supposed to be of second order, and to become of first order above a certain baryon density, corresponding to the tricritical point. In the more realistic scenario with small u and d quark masses, the second order transition at low baryon chemical potential changes into a cross-over, still remaining a first order transition at large baryon chemical potential. The tricritical point then turns into a critical one, and this has to be searched for in ultra-relativistic heavy-ion collisions. Since the critical point is a genuine thermodynamic singularity at which susceptibilities diverge, the resulting signatures of freeze-out near it all share the common property of being non-monotonic as a function of an experimentally varied parameter, such as the collision energy, centrality rapidity, or ion size. Being sensitive to the nature of the transition, E-by-E fluctuations can help to understand the nature of the QCD transition. In particular, large fluctuations in energy density due to QGP droplet formation are expected to occur if the transition is of first order. Second order phase transitions, on the other hand, may lead to divergence in the specific heat, also increasing the fluctuations in energy density due to long range correlations in the system [93]. They manifest as fluctuations in mean transverse momentum if matter freezes out at the critical temperature T_C [94, 95]. Moreover, the system freeze-out near the (tri)critical point would also lead to changes in the fluctuation pattern [93].

Anyway, E-by-E fluctuations depend not only on the type and order of the phase transition, but also on the speed at which the collision zone goes through the transition, the degree of equilibrium, the subsequent hadronization process, the amount of rescatterings between hadronization and freeze-out, and so on. It may even be that any sign of the transition is smeared out and wiped out before freeze-out as a consequence, for example, of hadronic rescattering and resonance decays.

In the following sections, an overview of the most important sources of fluctuations of E-by-E fluctuations which can originate in high-energy nucleus-nucleus collisions will be provided.

3.2.1 Non Dynamical Fluctuations

There are some major types of non dynamical fluctuations which have to be dealt with in heavy ion collisions.

The relative fluctuation ω_X in an observable X can be expressed as:

$$\omega_X = \frac{\sigma_X^2}{\langle X \rangle},$$

where σ_X^2 is the variance of the distribution and $\langle X \rangle$ stands for its mean value. The value ω_X that can be extracted from experimental data is the sum of different contributions, originating from statistical, trivial, and dynamical sources. Apart from the already mentioned statistical contribution arising from the finite particle multiplicities (see Sec. 3.2), there are other known sources which have to be taken into account and properly subtracted. Among these, the limited detector acceptance influences the observed fluctuation pattern, as well as geometrical volume fluctuations, and fluctuations coming from the initial reactions when no further rescatterings occur.

Geometrical fluctuations are due to the unavoidable uncertainty on the centrality of the collision, and for this reason they are called volume fluctuations. In particular, these fluctuations induce a positive correlation in particle production which does not depend on the intrinsic dynamical properties of the collision. Anyway, the effects of volume fluctuations can be removed when trying to study dynamical fluctuations, defining proper variables closely related to the quantities one is interested in. As an example, systematic and quantitative studies on mean transverse momentum fluctuations are usually performed using the Φ measure[1] [96].

Moreover, fluctuations in the number of primary collisions and effects of rescattering of secondaries contribute to the observed experimental value of ω_X. Anyway, it is not yet clear whether rescatterings increase relative fluctuations through greater production of multiplicity, transverse momenta, etc., or decrease fluctuations by involving a greater

[1] The Φ measure has the peculiar characteristic of being independent of the particle multiplicity. Defining for every particle i:

$$z_i = x_i - \bar{x},$$

where x is the physical quantity under study (for example the transverse momentum) and the overline denotes the average value of x over a single particle inclusive distribution, then for every event the quantity:

$$Z = \sum_{i=1}^{N} z_i$$

can be obtained, where N is the number of particles in the event. Then the Φ variable is defined as:

$$\Phi_x = \sqrt{\frac{\langle Z^2 \rangle}{\langle N \rangle}} - \sqrt{\overline{z^2}},$$

where the averages denoted by angular brackets are made over the events.

number of degrees of freedom. With respect to this, two limiting cases have been studied for example in [97]: first, the participant or "wounded nucleon model" (WNM) [98], in which one assumes that the particle production occurs in the individual participant nucleons and the rescattering of secondaries is ignored; second, the thermal limit approach in which scatterings bring the system into local thermal equilibrium. To be noted that the degree of thermalization in a collision can depend on the centrality of the collision itself (as volume or impact parameter fluctuations do) [99].

Finally, other expected sources of fluctuations are resonance decays, Bose-Einstein correlations and QCD color fluctuations.

3.2.2 Transverse Energy

In nucleus-nucleus collisions, the transverse energy E_T (see Sec. 1.3.1) is an extensive variable which provides a direct measure of the "violence" of the collision, since it depends on the number of participating nucleons. E_T is produced by redirection of the longitudianl energy into transverse motion through interactions in which particles undergo multiple scatterings and approach thermalization. E_T is also related to the energy reached in the collision, and since the energy density is a crucial parameter for the QGP phase transition, the study of E_T and its fluctuations is extremely important. Since the cross-section for a specific E_T value is strongly affected by the geometric probability of a given impact parameter, fluctuations in E_T are expected to be affected by those in the impact parameter.

Figure 3.1 shows the results obtained by WA98 experiment on E_T fluctuation analysis. The solid curve superimposed to the E_T distribution in the left panel shows a Guassian fit to the distribution. The fluctuations in E_T are shown in the right panel of Fig. 3.1 as a function of centrality. In particular, it is possible to observe an increase in the relative fluctuations of E_T going from central to peripheral collisions.

3.2.3 Mean Transverse Momentum and Energy Fluctuations

The mean transverse momentum fluctuation measurement has been one of the first proposed analyses to establish the existence of the QGP and investigate its properties. This is primarily due to the fact that a transverse motion is generated during the collision (being sensitive to its dynamics). Moreover, near the (tri)critical point in the QCD phase diagram, the E-by-E fluctuation pattern in transverse momentum should change significantly. For this reason, measuring deviations of the event-by-event average p_T of

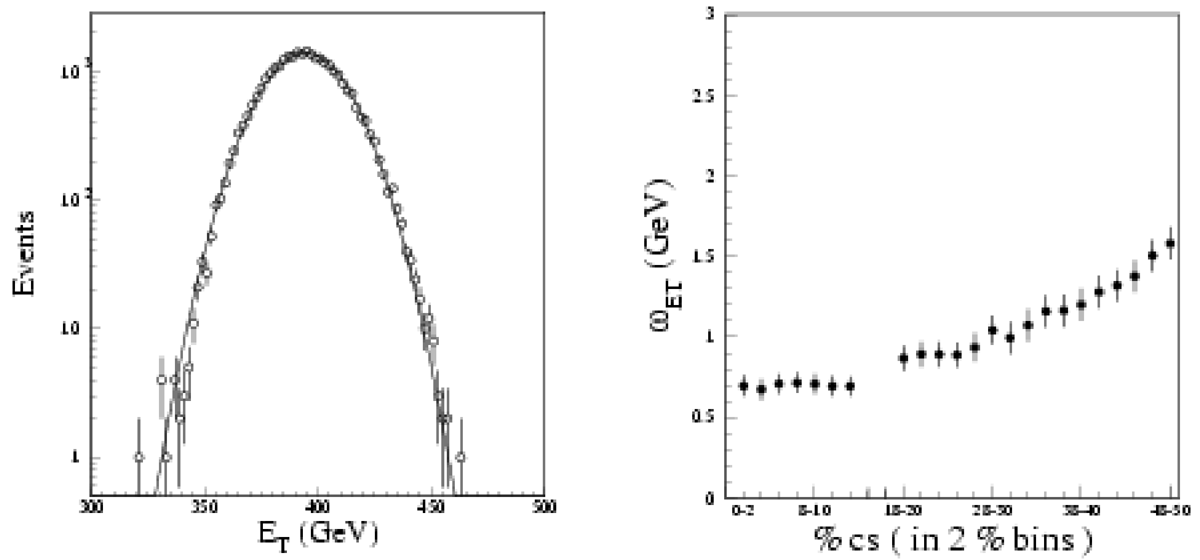

Figure 3.1: Left: Transverse energy distribution for the top 2% of the minimum bias cross-section events (corresponding to the most central events). Right: Centrality dependence (expressed as cross-section percentage) of the relative fluctuations in total transverse energy E_T. The results have been obtained by the WA98 experiment [100].

produced charged particles from the expectation for statistically independent particle emission would be very important and meaningful.

In particular, E-by-E fluctuations of $\langle p_T \rangle$ are sensitive to models describing nuclear collisions. For example, models considering them just as the superposition of independent p+p collisions predict much larger fluctuations compared to models including significant re-scattering from secondaries. In addition to this, the strength of the fluctuations should be directly related to fundamental properties of the system, such as the specific heat and the matter compressibility. A detailed dicussion of transverse momentum fluctuations can be found in [93]. To be noted that also the formation of the DCC could result in $\langle p_T \rangle$ fluctuations.

Figure 3.2 shows the results of the study of the PHENIX experiment on mean transverse momentum fluctuations. The statistical contributions have been subtracted thanks to the use of a "mixed event" constructed as a reference sample (see [101] for a description of the technique). The comparison of the data with mixed events is shown also in terms of residuals of the difference between the data and the mixed event distributions in units of standard deviations of the individual data points (see [102] for more details). As found by

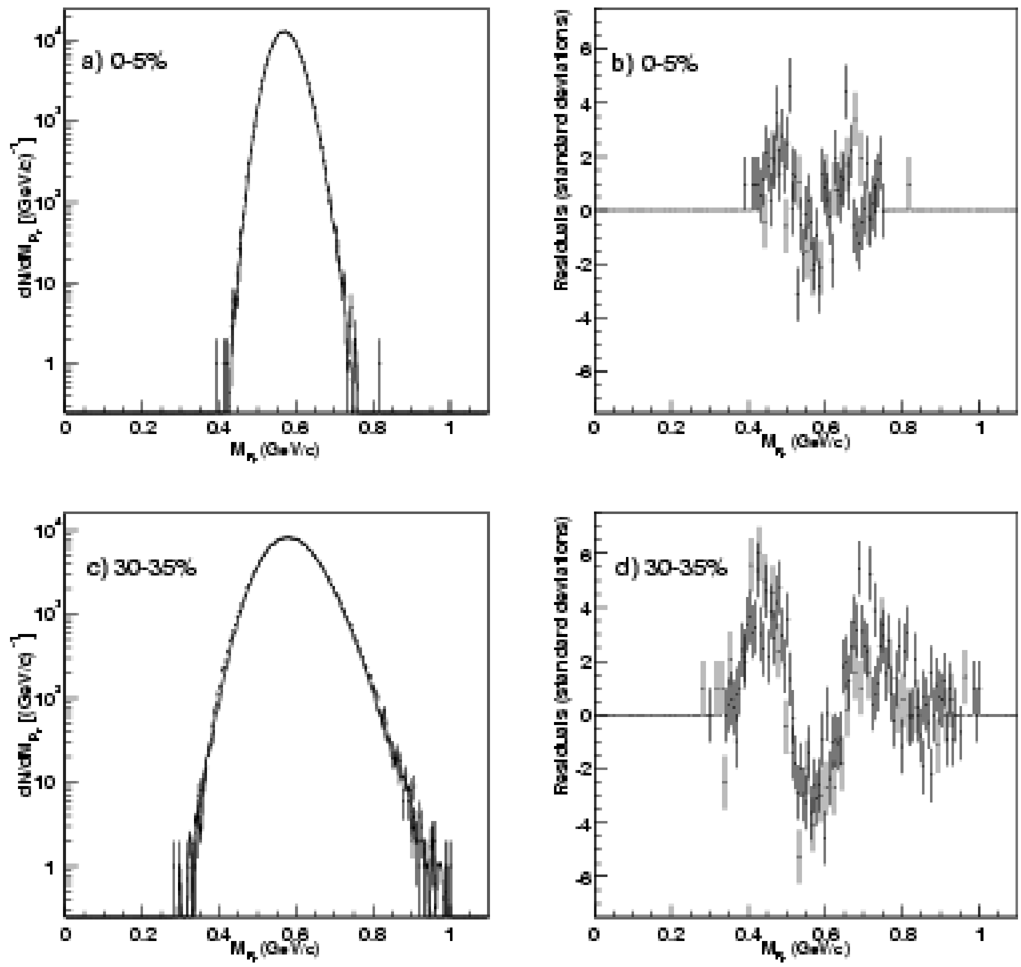

Figure 3.2: Comparison between the data and mixed event $\langle p_T \rangle$ distributions for the representative 0–5% and 30–35% centrality classes, as obtained by PHENIX in Au+Au collisions ($\sqrt{s_{NN}}$ = 200 GeV/c) at RHIC. Panels (a) and (c) show direct comparisons of the data (points) and normalized mixed events (solid line) $\langle p_T \rangle$ distributions. Plots (b) and (d) show the residuals between the data and the mixed events in units of standard deviations of the data points form the mixed event points [102].

the PHENIX Collaboration, a large contribution to the observed non-random fluctuations is due to the correlation of high p_T particles (HBT correlations), probably related to jet production [103].

Along with mean transverse energy, the PHENIX experiment has recently carried on an analysis on mean transverse energy fluctuations $\langle E_T \rangle$. Figure 3.3 shows the mean transverse energy distributions obtained for different centralities. The fluctuations in the

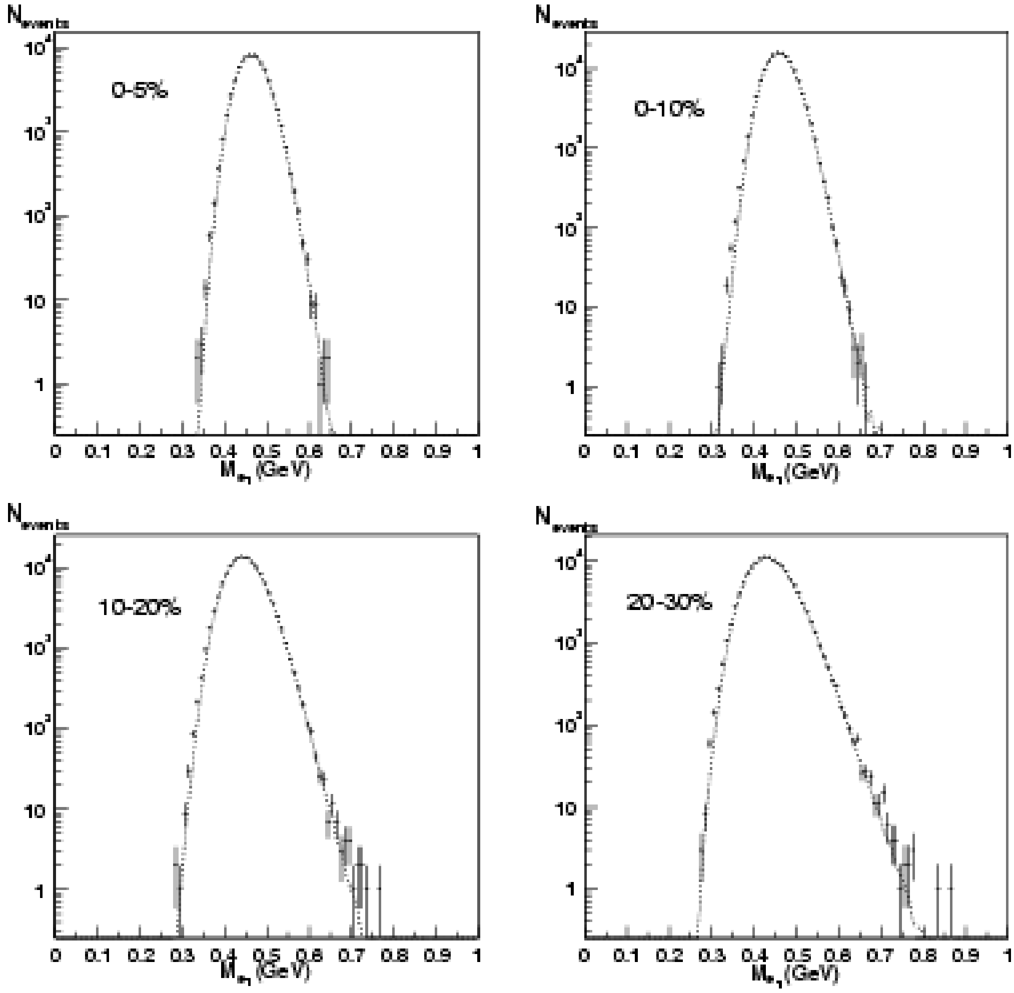

Figure 3.3: Mean transverse energy distribution measured at RHIC in Au+Au collisions ($\sqrt{s_{NN}}$ = 130 GeV/c) by PHENIX, for the four centrality classes 0–5%, 0–10%, 10–20% and 20–30%. The curves are the random baseline mixed event distributions used to evaluate the statistical fluctuation contribution [104].

$\langle E_T \rangle$ distributions reveal a non-statistical contribution much of which, however, can be accounted for by merged clusters (the reconstruction of which was used in the analysis), and to low energy background (low energy electrons and muons) [104].

3.2.4 Multiplicity Fluctuations

Multiplicity fluctuations are an important quantity to characterize the evolving system in a heavy-ion collision since they can provide a distinct signal of the QGP phase transition.

They depend on the type and order of the transition, on the speed with which the collision zone goes through the transition, on the degree of equilibrium, the subsequent hadronization process, the number of rescatterings between the hadronization and freeze-out stages and so on.

In the case of multiplicity fluctuations, predictions vary from a possible enhancement related to the production of QGP droplets and to nucleation processes in case of a first order transition, to a strong suppression as a consequence of a rapid freeze-out immediately after the phase transition.

Multiplicity fluctuations are to a large extent affected by statistical and geometrical fluctuations. The dependence on the centrality of the collision of multiplicity fluctuations has been studied for example by the NA49 Collaboration [105] in terms of the scaled variance of the distribution defined as $var(N)/\langle N\rangle$. Here $var(N)$ represents the variance of the multiplicity distribution in a given centrality bin, and $\langle N\rangle$ is the mean of the distribution. Figure 3.4 shows the analogous results of the recent analysis on multiplicity fluctuations in terms of $var(N)/\langle N\rangle$ as measured by the PHENIX experiment [106].

As can be seen, a non-monotonic behaviour is found. Moreover, positively and negatively charged multiplicities are very similar, while the corresponding values when considering all the charged particles are larger. This is probably a consequence of charge conservation.

3.2.5 Net Charge Fluctuations

Recent theoretical studies have revealed that a drastic decrease in the event-by-event fluctuations of the net charge should occur in local phase-space regions as a signature of the plasma state [107, 108, 109]. These fluctuations should not be related to the transition itself, but rather with the charge distribution in the plasma phase. The idea which lies under this prediction states that the charge carriers in the plasma should carry less charge than the carriers in ordinary hadronic matter. As a result, the charge would be even more uniformly distributed in a plasma. It is not still clear, however, how the original distribution may survive the transition back to ordinary matter.

Net charge fluctuations are influenced by hadronic resonance decays, which occur independently on deconfinement. As a matter of fact, in the absence of a QGP, deviations from statistical behaviour can be used to investigate the abundance of, for example, the ρ and ω mesons. Anyway, since charge is a conserved quantity, then fluctuations will be further reduced. To be noted that the net charge fluctuations, because of resonance decays into correlated pairs of one positive and one negative particle, and because of

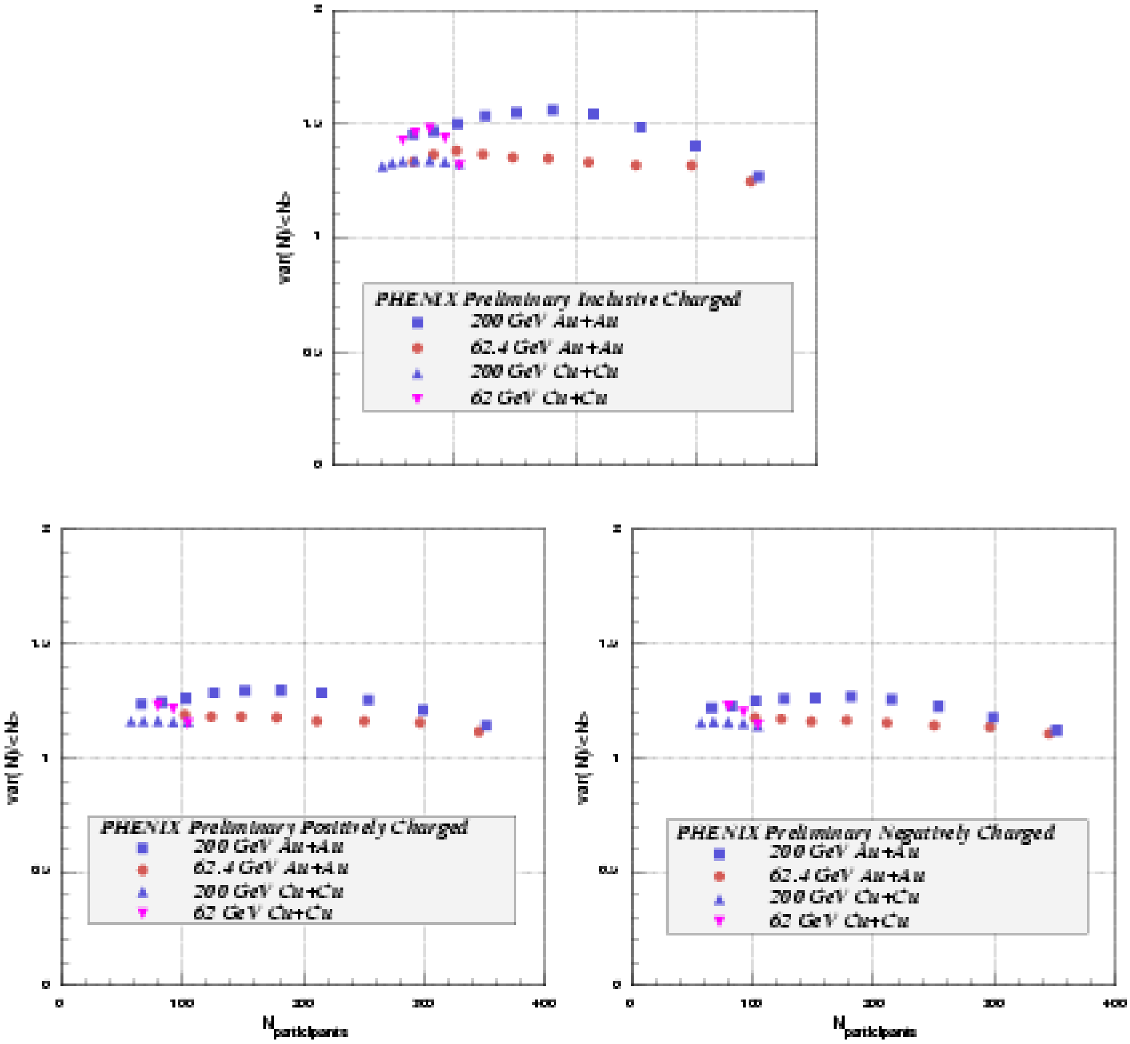

Figure 3.4: Inclusive (top), negatively charged (bottom, left) and positively charged (bottom, right) particle multiplicities in terms of the scaled variance as a function of centrality in heavy-ion interactions, as measured by the PHENIX experiment at RHIC [106]. The error bars include statistical and systematic errors.

charge conservation law, will decrease as the experimental acceptance increases.

Net charge fluctuations are usually studied considering the variables $R = n_+/n_-$ (the ratio between positive and negative particles) and $Q = n_+ - n_-$, the net charge. Figure 3.5

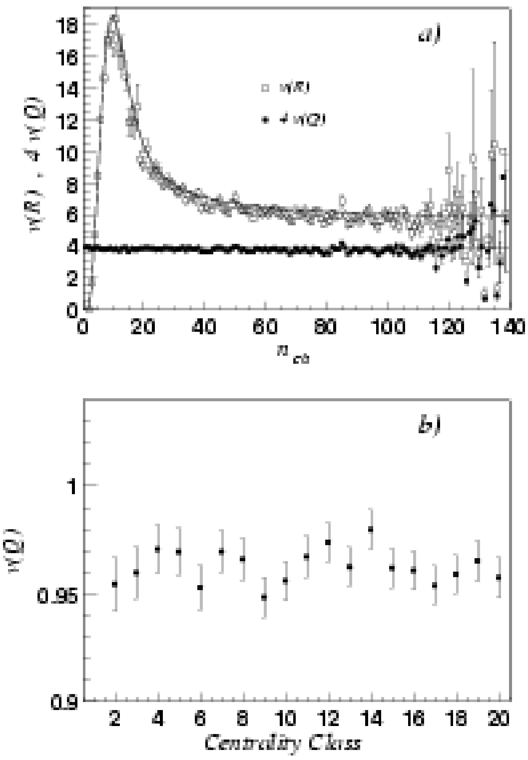

Figure 3.5: The normalized variances $v(Q)$ and $v(R)$ as a function of $n_{\rm ch}$ (top), and the variance $v(Q)$ as a function of the centrality classes obtained by PHENIX at RHIC in Au+Au collisions ($\sqrt{s_{NN}} = 130$ GeV/c). Each centrality class corresponds to 5% of the events the full sample of which covers 92% of the inelastic cross-section, such that class 20 is the most central one. See [110] for more details.

shows the normalized variance $v(X)$ $(X = R, Q)$, defined as:

$$v(X) = \frac{V(X)}{n_{\rm ch}}$$

where $V(X)$ is the variance of the variable X and $n_{\rm ch} = n_+ + n_-$, as measured in the PHENIX experiment at RHIC. The quantity $v(Q)$ has been multiplied by a factor 4 to compensate for the asymptotic difference between $v(R)$ and $v(Q)$. In a stochastic scenario, $v(Q)$ should be equal to unity, while $v(R)$ should asymptotically reach 4, as $n_{\rm ch}$ increases. A small excess of positively charged particles can be observed growing proportionally with $n_{\rm ch}$.

The STAR collaboration has also studied E-by-E net charge fluctuations considering

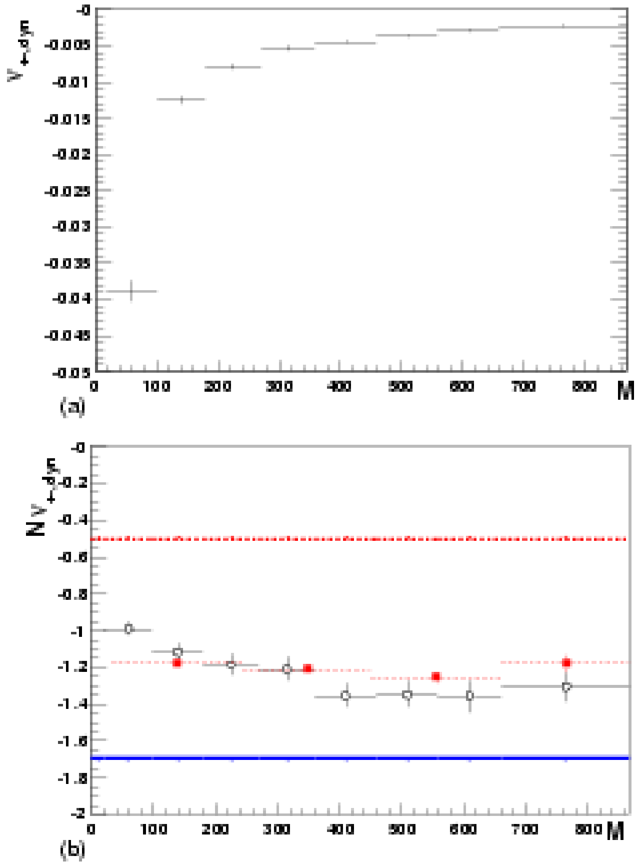

Figure 3.6: Top: Dynamical net charge fluctuations $\nu_{+-,dyn}$ measured in the pseudorapidity range $|\eta| < 0.5$ as a function of the total charged particle multiplicity M in $|\eta| < 0.75$, for STAR Au+Au collisions at $\sqrt{s_{NN}} = 130$ GeV. Bottom: Dynamical net charged fluctuations scaled by the average number of charged particles N in an event with a given total multiplicity M, $N\nu_{+-,dyn}$ (open circles), measured in the rapidity range $|\eta| < 0.5$ as a function of the same relative particle multiplicity M in $|\eta| < 0.75$. The dotted line corresponds to the charge conservation value, while the solid line refers to a resonance gas, and the solid squares represent the results of HIJING calculations. See [111] for more details.

the so-called dynamical net charge variance defined as:

$$\nu_{+-,dyn} = \frac{\langle N_+(N_+-1)\rangle}{\langle N_+\rangle^2} + \frac{\langle N_-(N_--1)\rangle}{\langle N_-\rangle^2} - 2\frac{\langle N_+N_-\rangle}{\langle N_+\rangle\langle N_-\rangle},$$

where the notation $\langle N\rangle$ is used to express an event average and N_+ and N_- refer to the multiplicities of positively and negatively charged particles, respectively. Details on the properties of $\nu_{+-,dyn}$ can be found in [111]. The top panel of Figure 3.6 shows the values of $\nu_{+-,dyn}$ measured in the pseudorapidity range $|\eta| < 0.5$, obtained for Au+Au collisions at $\sqrt{s_{NN}} = 130$ GeV as a function of the total multiplicity measured in $|\eta| < 0.75$. The negative value of $\nu_{+-,dyn}$ indicates that positive and negative particles are correlated in the collisions. Moreover, the dynamical net charge variance decreases monotonically with increasing collision centrality, which can be understood from the fact that more central Au+Au collisions involve an increasing number of "subcollisions", with the resulting decrease of two-particle correlations and the reduction of $\nu_{+-,dyn}$.

The bottom panel of Fig. 3.6 shows the dynamical net charge variance scaled by the average number of charged particles in an event with a given multiplicity M, which should be independent of collision centrality if no significant variation in the mechanism of the particle production arises when changing the collision centrality. This, in fact, is not observed, suggesting that there could be rescattering effects or other dynamical effects related to centrality, which have to be further investigated.

3.2.6 Particle Ratio Fluctuations

Early theoretical investigations [17] have suggested that if the free enthalpy difference between the plasma and the hadronic phase was high, marked overheating-supercooling fluctuations may occur at about the critical temperature T_C. These fluctuations would then manifest in a broadening of the event-by-event kaon to pion total yield ratio. Moreover, it is claimed that near the QCD phase boundary, and especially near the (tri)critical point, the pattern of E-by-E particle ratio fluctuations should change.

Since it is suggested that strangeness fluctuations, especially in the K/π ratio, should be sensitive to the QGP phase transition, a lot of attention has been put on particle ratio fluctuations studies. This observable has the intrinsic advantage of not being influenced by volume and impact parameter fluctuations, since by simply increasing/decreasing the volume or centrality the average number of both types of particles scales up/down by the same amount, and cancels out in the ratio.

Figure 3.7 shows the distributions of the K/π and p/π ratios obtained from the NA49 experiment for the 3.5% most central Pb+Pb collisions at $\sqrt{s_{NN}} = 20, 40$ and 160 GeV. Here, the relative width of the distribution $\sigma = \text{rms/mean} \times 100\%$ is the sum of four main contributions: the statistical fluctuations due to the finite particle multiplicities, the experimental resolution which affects particle identification, the effects of the event-by-event fitting procedure, and the genuine dynamical fluctuations. After estimating the contributions due to statistics and to the detector resolution (with the mixed event

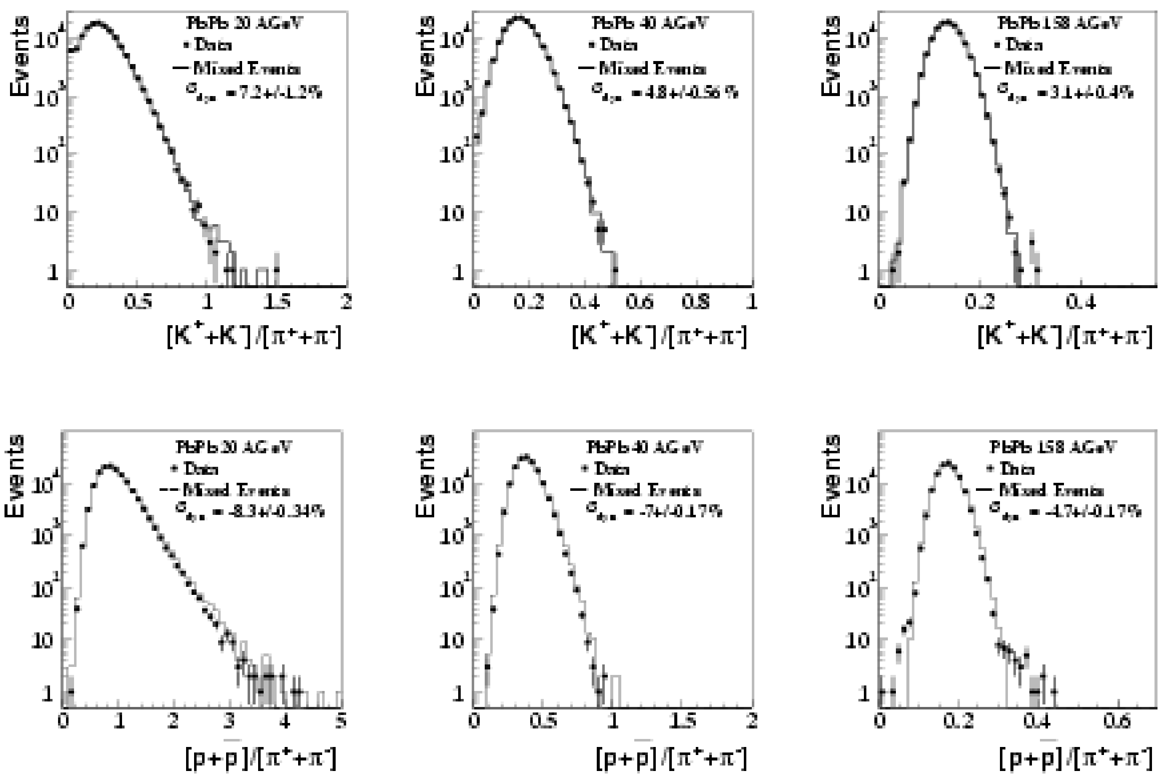

Figure 3.7: K/π (top) and p/π (bottom) ratio distributions for the 3.5% most central Pb+Pb collisions at $\sqrt{s_{NN}}$ = 20, 40 160 GeV obtained by the NA49 experiment [113]. Superimposed to the points corresponding to values from data, the histograms show the mixed event results.

technique [101]), the remaining dynamical width is calculated. The observed fluctuations in K/π ratios are positive and decrease with beam energy, as shown in Figure 3.8. On the contrary, in the case of p/π ratios, the dynamical fluctuations are negative, which can be a ccounted for by resonace decays into pions and protons. The comparison with the UrQMD model [114], where no fluctuations due to a phase transition are considered, leads to the conclusion that, in fact, for p/π ratios, negative fluctuations are due to resonance decays. On the contrary, for K/π ratios, the UrQMD does not reproduce the energy dependence of the signal, and in this case the finite fluctuation signal is likely to be due to correlated particle production as a consequence of conservation laws.

Figure 3.9 shows the results obtained by the STAR experiment on K/π ratio measurements for Au+Au collisions at $\sqrt{s_{NN}}$ = 200 GeV. The approach used was the same as that adopted by the NA49 experiment for the results presented in Figs. 3.7 and 3.8. The dynamical fluctuations in K/π for top 5% central Au+Au collisions measured by

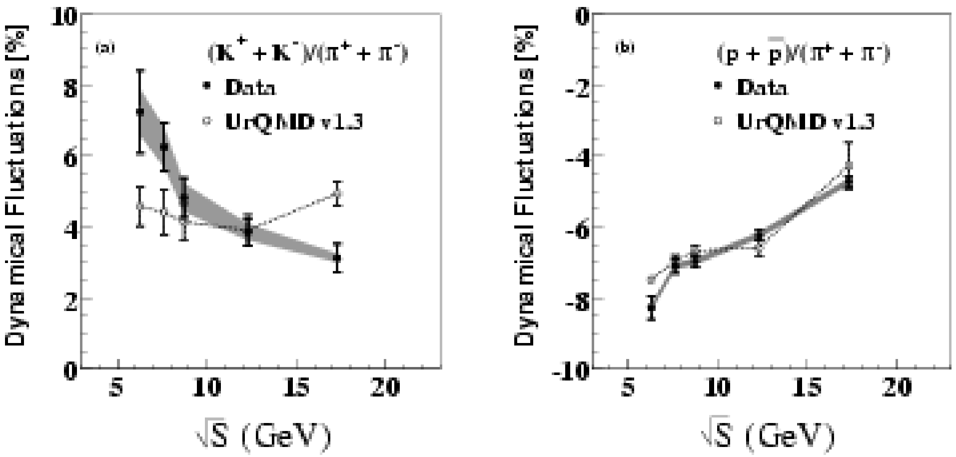

Figure 3.8: Energy dependence of the event-by-event fluctuation signal of the K/π ratio (left panel) and p/π ratio (right panel), as measured by NA49 at the SPS. The grey bands refer to the systematic errors of the measurement [113].

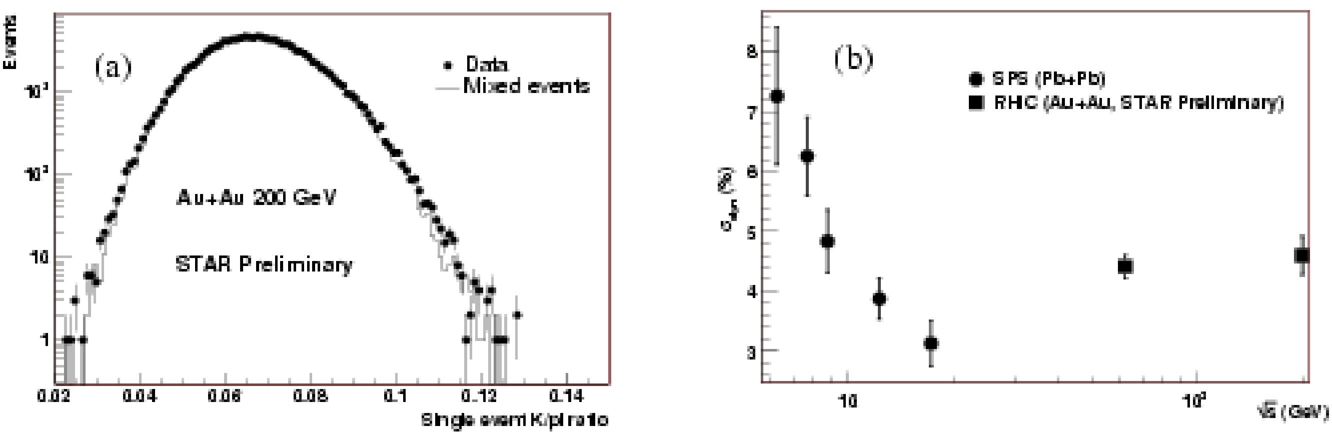

Figure 3.9: Left: Distribution of K/π ratio from data (points) and mixed events (histogram) for the most central events (with 5% centrality) in Au+Au collisions at $\sqrt{s_{NN}} = 200$ GeV [116]. Right: Energy dependence of the dynamical fluctuations σ_{dyn} as obtained by STAR compared with those obtained by the NA49 experiment [115].

STAR are $\sim 4.6\%$ and they appear to be constant as the collision energy changes. Other studies concerning the dependence on centrality of the particle ratio dynamical variance

$\nu_{K/\pi,dyn}$[2] have shown that it is positive, and decreases while collision centrality increases (see Fig. 3.10).

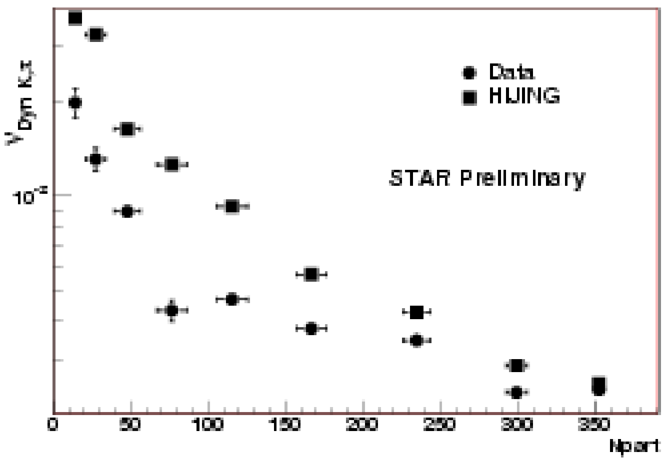

Figure 3.10: Centrality dependence of $\nu_{K/\pi,dyn}$ for Au+Au collisions at $\sqrt{s_{NN}} = 200$ GeV [116] as measured by STAR at RHIC.

3.2.7 Temperature Fluctuations

One of the main parameters in describing heavy-ion collisions is temperature. Since the matter produced at the very early stages of the collision is thought to reach at least local thermodynamic equilibrium, trying to understand whether a unique temperature can trace the freeze-out, or if temperature fluctuations occur from event to event is of extreme interest.

The relation between the temperature and the thermodynamics of the system can be found in the total heat capacity of the system itself, C_V [117], defined by:

$$\frac{1}{C_V} = \frac{(\Delta T)^2}{T^2}.$$

Since C_V is an extensive quantity, then $\Delta T \sim 1/\sqrt{N}$, where N is the number of particles in the system. The role of the heat capacity when studying the thermodynamics of a

[2]The particle ratio dynamical fluctuation is defined, in analogy with the net charge dynamical fluctuation, as:

$$\nu_{K/\pi,dyn} = \frac{\langle K(K-1)\rangle}{\langle K\rangle^2} + \frac{\langle \pi - (\pi - 1)\rangle}{\langle \pi\rangle^2} - 2\frac{\langle K\pi\rangle}{\langle K\rangle\langle \pi\rangle}.$$

system reveals in its irregular behaviour when, for example, a phase transition occurs, depending not only on the existence of such a phase transition, but also on its nature. If the specific heat c_V, defined as $c_V = C_V/N$, diverges, the coefficient $1/\sqrt{N}$ vanishes, and temperature fluctuations are suppressed. For freeze-out in the crossover (second order) region, or in the hadronic phase just below the first order transition, c_V is finite. As the (tri)critical point is approached, c_V diverges and the fluctuations decrease.

Experimentally, temperature fluctuations can be found via event-by-event p_T spectra analyses. In particular, one can study the particle p_T distributions using the relation:

$$\frac{1}{p_T}\frac{dN}{dp_T} \propto \exp\left(-\frac{m_T}{T}\right) \tag{3.1}$$

where m_T is the transverse mass as defined in Sec. 1.3.1, and T is the *effective* temperature which relates the freeze-out temperature to the transverse flow velocity (see Eq. 1.5). Analogously, in terms of m_T one can write:

$$P_{(T)}(m_T) \sim m_T \exp\left(-\frac{m_T}{T}\right).$$

Moreover, the temperature variance can be measured through the average transverse mass of the event, defined as:

$$\mu_T = \frac{1}{N}\sum_{i=1}^{N} m_T^i,$$

where N stands for the event multiplicity, and the sum runs over the event particles. If the p_T spectra follows the exponential form of Eq. 3.1, then μ_T is related to the event temperature according to the formula:

$$\mu_T = \int_m^\infty dm_T m_T P_{(T)}(m_T) = \frac{2T^2 + 2Tm + m^2}{T + m}.$$

Inverting this, the temperature can be derived from the measurement of μ_T, and its variance $V(T) = \langle T^2\rangle - \langle T\rangle^2$ can be obtained.

The shortcoming of the approach described above is that μ_T is subject to pure statistical fluctuations. This does not happen when considering the so called Φ-measure [96], which has the advantages of not being influenced by trivial geometrical fluctuations, of being independent of centrality, and of being equal to zero when inter-particle correlations are absent (see [118, 119] for an analytical treatment of $\Phi(p_T)$). The NA49 Collaboration has recently carried on some studies on $\Phi(p_T)$, finding physical values very similar for p+p and Pb+Pb collisions at the same energy $\sqrt{s_{NN}} = 158$ GeV [120]. Nevertheless, since the origin of transverse momentum fluctuations should be different in the two cases, the results obtained are still under study.

3.3 Event-by-Event Fluctuations in ALICE

In the following Section, the results from an analysis of the ALICE experiment perfomance concerning event-by-event studies will be presented as the core of this PhD thesis.

First, a brief description of the Monte Carlo event sample used will be provided. Then, the performance of the detector in terms of particle identification (PID) will be discussed. Finally, the event-by-event fluctuations in identified particle transverse momentum spectra and particle ratios for the ALICE experiment will be illustrated.

3.3.1 Monte Carlo Event Sample and Detector Simulation

The Monte Carlo event sample used for this analysis consists of about 300 Pb+Pb central collisions at $\sqrt{s_{NN}} = 5.5$ TeV generated with the HIJING 1.36 Monte Carlo generator [78]. The impact parameter has been chosen to be in the range $0 < b < 5$ fm, which corresponds to the 10% of the total inelastic cross-section for Pb+Pb collisions ($\sigma^{\mathbf{tot}}_{\mathbf{inel,Pb+Pb}} = 8$ barn) at LHC. The magnetic field has been set to $B = 0.5$ T. GEANT3 [83] has been used to track the particles in the collisions, and to simulate the detector signals and responses. Vertex reconstruction, particle tracking, and particle identification have been performed as described in Sec 2.2.

The number of generated primaries per event for the three different particle species of interest in this analysis, i.e. pions, kaons and protons, is reported in Table 3.1. A trans-

Particle Species	Number of Primaries
π	7690
K	745
p	385

Table 3.1: Mean number of primaries per event generated in the pseudorapidity range $-0.9 < \eta < 0.9$, with transverse momentum $0 < p_T < 4$ GeV/c. The values refer to the sample of 300 HIJING central Pb+Pb events used for the results presented in this thesis.

verse momentum cut has been applied, resulting in the selection of the particles with $0 < p_T < 4$ GeV/c. The upper p_T value has been chosen in agreement with the transverse momentum range of interest for the event-by-event temperature fluctuation analysis carried out (see Sec. 3.3.3). The acceptance of the detectors taken into account for particle identification (which is the first step of this analysis) has influenced the particle selection in such a way that for the primaries taken into account $-0.9 < \eta < 0.9$, corresponding to the central region of the experiment.

3.3.2 Particle Identification in the reference Event Sample

In order to study event-by-event fluctuations in ALICE in terms of temperature and particle ratios, first a Particle IDentification (PID) analysis has been performed. In particular, the concern has been turned on the PID capabilities of the central tracking detectors ITS and TPC, and of the Time Of Flight detector. The charged hadron identification algorithms applied by these d etectors have already been described in Sec. 2.2.2, while the combined PID approach has been presented in Sec. 2.2.3. In the following sections, the perfomance of the ITS, TPC and TOF particle identification applied to the high-centrality Pb+Pb event sample, specifically generated for the E-by-E analysis of this thesis will be discussed. The results of the combined PID (ITS+TPC, ITS+TPC+TOF) will be provided as well.

The efficiency and the contamination of the particle identification procedures will be expressed according to the definition given in Eq. 2.9. Moreover, the so-called overall efficiency calculated with respect to the generated primary particles will be presented.

ITS

As already stated in Sec. 2.2.2, the ITS detector is able to identify particles via dE/dx measurements in the low transverse momentum region. Figure 3.11 shows the efficiency and contamination for the ITS particle identification algorithm applied to the event sample used for this analysis. The results are shown for particles with transverse momentum greater than 0.25 MeV/c. The upper p_T limit has been set at 4 GeV/c, $\sim$ 1 GeV/c and $\sim$ 1.5 GeV/c for pions, kaons and protons, respectively. The choice has been driven by the limited particle separation power of the ITS detector in the high momentum region (see Fig. 2.15), which reflects in the decreasing kaon and proton efficiency drop when approaching $p_T \sim 1$ GeV/c. Nevertheless, for $0.15 < p_T < 0.5$ GeV/c for kaons, and $0.15 < p_T < 1$ GeV/c for protons, the efficiency approaches 90%. In particular, a slightly lower efficiency can be observed in the case of protons at very low transverse momenta, mainly due to reconstruction inefficiency. On the other hand, being the most abundant produced particles, pions can be identified by the ITS up to $p_T \sim 4$ GeV/c with an efficiency $\sim$99% in the whole transverse momentum range.

As regards contamination, for pions it stays well below the 40% up to $\sim$ 1.5 GeV/c, where it levels at this vealue. For kaons and protons, a rapid rising can be seen start-

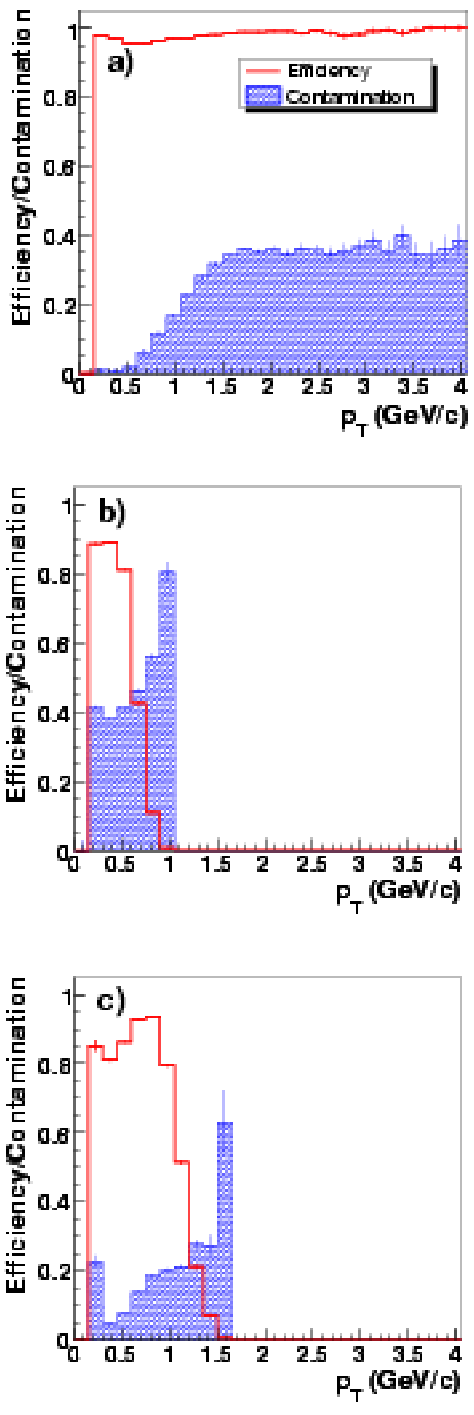

Figure 3.11: Efficiency and contamination for the ITS particle identification procedure applied to $\sim$ 300 HIJING central events for the three particle species: pions (a), kaons (b) and protons (c).

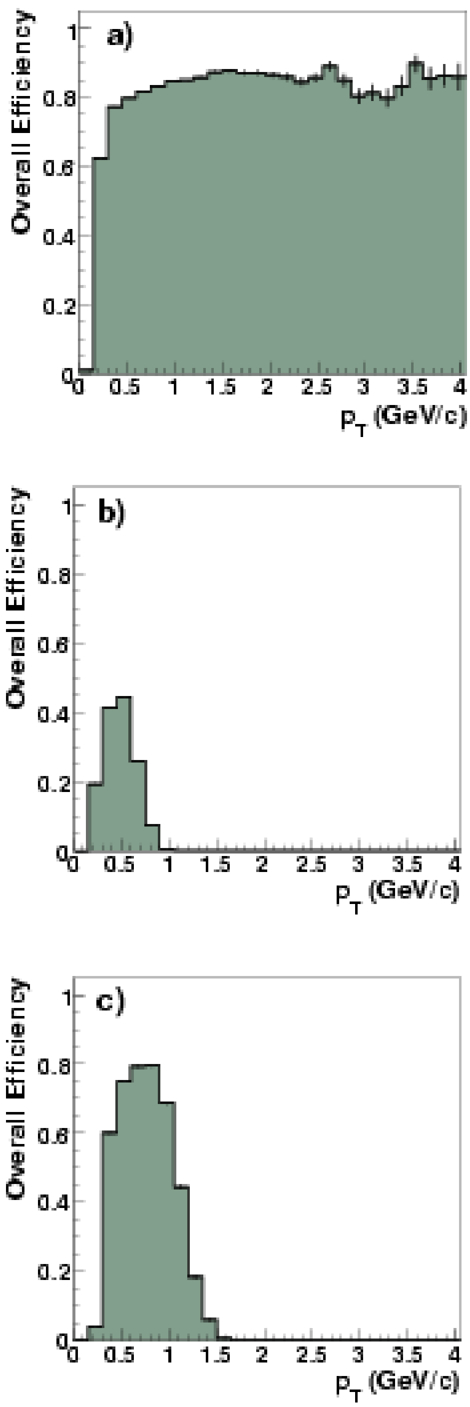

Figure 3.12: Overall efficiency for the ITS particle identification procedure applied to $\sim$ 300 HIJING central events for the three particle species: pions (a), kaons (b) and protons (c).

ing from 0.65 GeV/c and 1.5 GeV/c respectively. Again, reconstruction defects and the limited separation power at high momenta are the main causes for the observed contamination values.

Figure 3.12 shows the overall efficiency calculated with respect to the generated primaries for the ITS particle identification, for the same event sample. As said in Sec. 2.2.2, the particle identification overall efficiency is the sum of different factors which affect the PID results, mainly the reconstruction efficiency, the effects of dead zones and of particle decays and interactions. For this reason, the overall efficiency is always much lower than the algorithmic efficiency defined in Eq. 2.9. Table 3.2 gives the overall efficiency for the ITS particle identification integrated, for each particle type, over the corresponding momentum range. The very low kaon overall efficiency can be explained considering the high amount of decay processes they undergo.

Particle species	p_T range (GeV/c)	Overall Efficiency
π	$0.15 < p_T < 4$	74%
K	$0.15 < p_T < 1.05$	30%
p	$0.15 < p_T < 1.65$	60%

Table 3.2: ITS particle identification overall efficiency for π, K, and p integrated over the corresponding transverse momentum range.

TPC

The TPC particle identification capability spans over a slightly wider transverse momentum range than that of the ITS detector. Figure 3.13 shows the efficiency and contamination results of the TPC PID algorithm when applied to the generated 300 HIJING central event sample. The transverse momentum cut chosen in this case has been the same for all the three particle species, that is $0.15 < p_T < 4$ GeV/c. As it can be seen from Fig. 3.13, as in the case of the ITS, pions are identified with an efficiency very close to 100%, while in the case of kaons and protons the efficiency sharply decreases starting from $p_T = 0.5$ GeV/c for kaons, and $p_T = 0.75$ GeV/c for protons. At the same time, the contamination level for pions slowly rises from $\sim 10\%$ and then levels at about 35%, while it stays very high for kaons and protons, ranging from $\sim 30\%$ to $\sim 85\%$ for kaons, and from $\sim 10\%$ up to $\sim 85\%$ for protons, with a strong dependence on p_T. The results show that particle identification (apart from the obvious and in a sense "trivial" case of

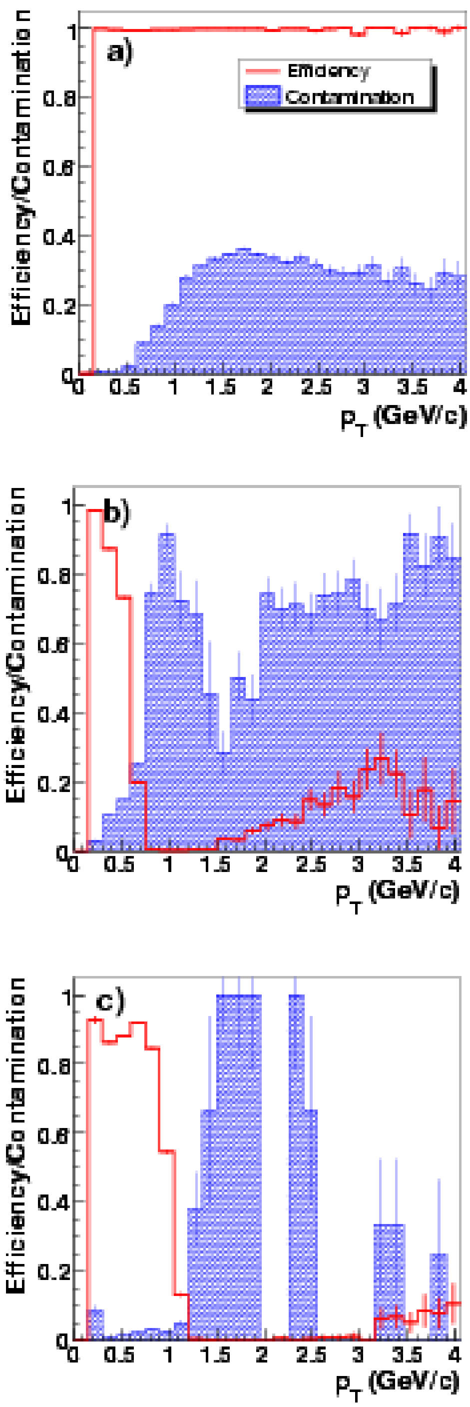

Figure 3.13: Efficiency and contamination for the TPC particle identification procedure applied to ~ 300 HIJING central events for the three particle species: pions (a), kaons (b) and protons (c).

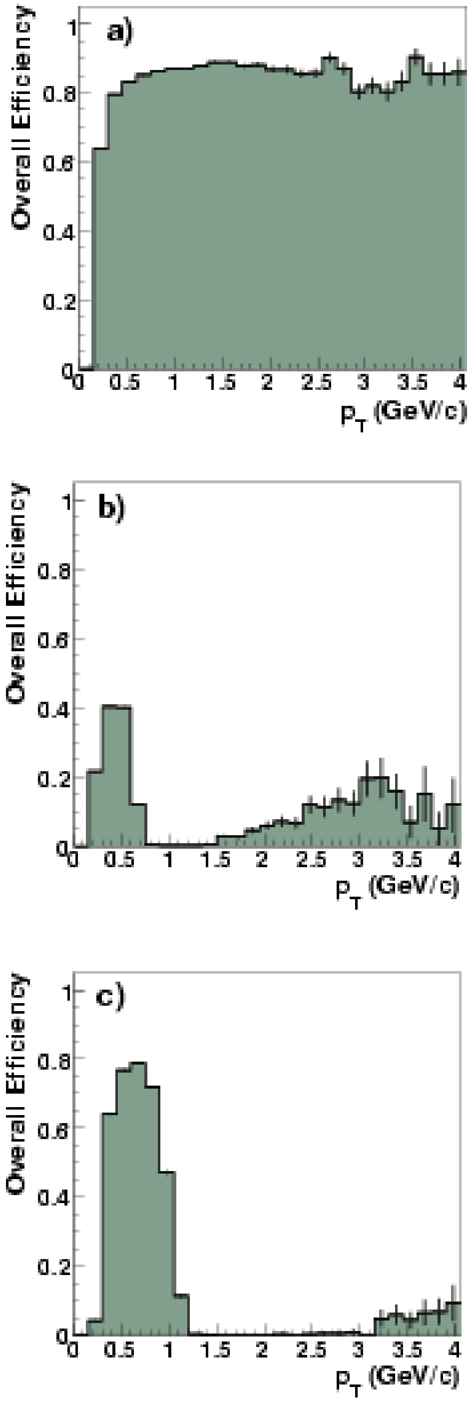

Figure 3.14: Overall efficiency for the TPC particle identification procedure applied to $\sim$ 300 HIJING central events for the three particle species: pions (a), kaons (b) and protons (c).

pions) can not be performed at intermediate and relatively high momenta just using the TPC (or the ITS) detector, although in the relativistic region the TPC is able to provide again a useful PID information [76].

Figure 3.14 shows the overall π, K, and p efficiencies with respect to the generated primaries for the TPC PID procedure. The values of the overall efficiencies integrated over the whole transverse momentum range are reported in Table 3.3.

Particle species	p_T range (GeV/c)	Overall Efficiency
π	$0.15 < p_T < 4$	76%
K	$0.15 < p_T < 4$	24%
p	$0.15 < p_T < 4$	53%

Table 3.3: TPC particle identification overall efficiency for π, K, and p integrated over the corresponding transverse momentum range.

ITS and TPC Combined PID

Figure 3.15 shows the results of combining the particle identification information coming from the ITS detector and the TPC detector (for more details, see Sec. 2.2.3), for the generated event sample. As one could have expected, since the PID capability of the ITS and the TPC considered separately are limited to the low momentum region (apart from the case of pions), even combining the information coming from both of them, the results do not change significantly. In particular, since the ITS particle identification has been performed for this analysis in a very limited p_T range for kaons and protons, for these two particle species the results at intermediate and high p_T are the same as those obtained with the TPC stand-alone PID procedure.

The ITS+TPC combined PID performance in the case of pions remains still excellent in terms of efficiency ($\varepsilon \sim 100\%$ over the whole p_T range), and satisfactory as regards contamination ($C \leq 30\%$ for $0.15 < p_T < 1.5$ GeV/c, and $C \sim 35\%$ for higher p_T). On the other hand, for kaons and protons (for which the ITS and TPC particle identification is more problematic), in the case of the combined ITS+TPC PID, the low momentum region in which the PID efficiency stays high ($\varepsilon > 50\%$) becomes wider than for the stand-alone detector PID case. In particular, this holds true in the interval $0.15 < p_T < 0.75$ for kaons, and $0.15 < p_T < 1.3$ GeV/c for protons. For what concerns K and p contamination, at small transverse momenta the dominant contribution comes from the ITS.

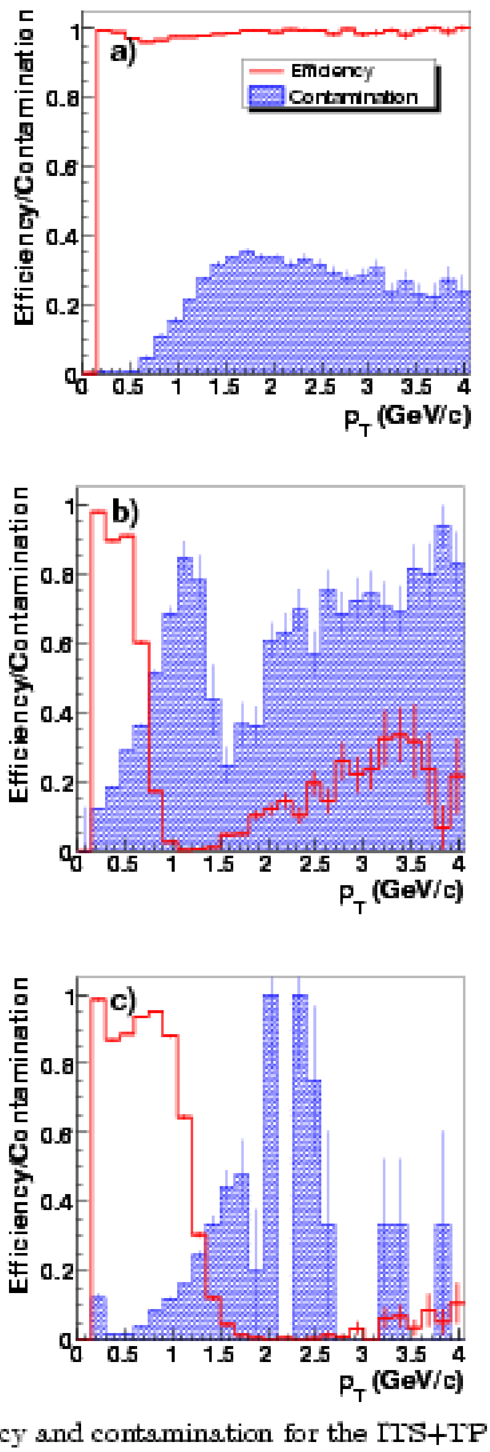

Figure 3.15: Efficiency and contamination for the ITS+TPC combined particle identification procedure applied to $\sim$ 300 HIJING central events for the three particle species: pions (a), kaons (b) and protons (c).

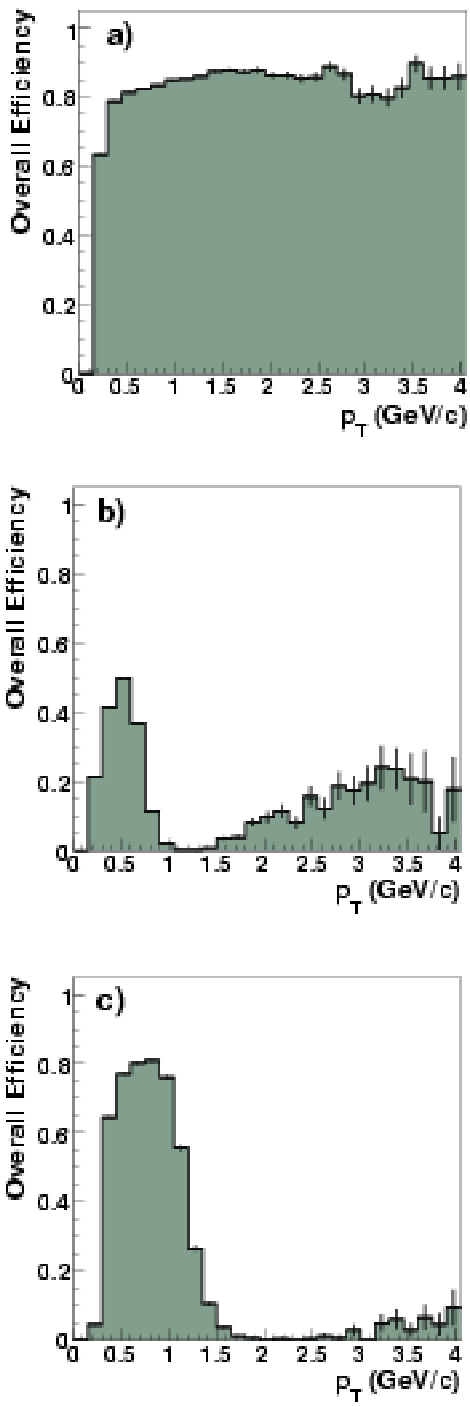

Figure 3.16: Overall efficiency for the ITS+TPC combined particle identification procedure applied to $\sim$ 300 HIJING central events for the three particle species: pions (a), kaons (b) and protons (c).

The improvement of the combined particle identification with respect to the stand-alone PID can be also seen in terms of the overall efficiency, which is shown in Fig. 3.16. The integrated overall efficiency values for π, K, and p are reported in Table 3.4, to be compared with those in Table 3.2 and 3.3 for the stand-alone detector results.

Particle species	p_T range (GeV/c)	Overall Efficiency
π	$0.15 < p_T < 4$	75%
K	$0.15 < p_T < 4$	31%
p	$0.15 < p_T < 4$	61%

Table 3.4: ITS+TPC combined particle identification overall efficiency for π, K, and p integrated over the corresponding transverse momentum range.

TOF

As said in Sec. 2.2.2, the Time Of Flight detector is able to provide an optimum particle separation up to a particle momentum $p \simeq 2.5$ GeV/c for π/K, and $p \simeq 4$ GeV/c for K/p. Figure 3.17 shows the particle identification performance of the TOF PID algorithm (see 2.2.2) in terms of efficiency and contamination, when applied to the ~ 300 HIJING central events generated for this study. The transverse momentum cut $p_T > 0.3$ GeV/c has been applied since particles with lower p_T would not reach the TOF sensitive surface as a consequence of the magnetic field. In fact, the increased effect of the energy loss in the case of kaons and protons should have made the cut be higher ($p_T > 0.35$ and $p_T > 0.45$ GeV/c for kaons and protons, respectively). Nonetheless, for consistency, the same p_T range for π, K, and p has been considered.

As can be seen, the TOF PID efficiency for pions stays above 95% over almost the whole p_T interval considered, while for kaons and protons it is significantly lower, and shows a momentum-dependence. In particular, as far as kaons are concerned, the efficiency decrease at low momenta is mainly due to decays and reconstruction failures, which are responsible also for the fall of the proton efficiency for $p_T < 1$ GeV/c. On the other hand, at high momenta, the decrease of the TOF separation power makes the efficiency become lower. This effect is especially visible in the case of kaons for which the probability to be mis-identified mostly as pions is high in the high p_T region (see Fig. 2.24).

For what concerns contamination, in the case of pions it ranges from a few percents up to $\sim 20\%$, coming mainly from kaons. A similar level of contamination can be observed

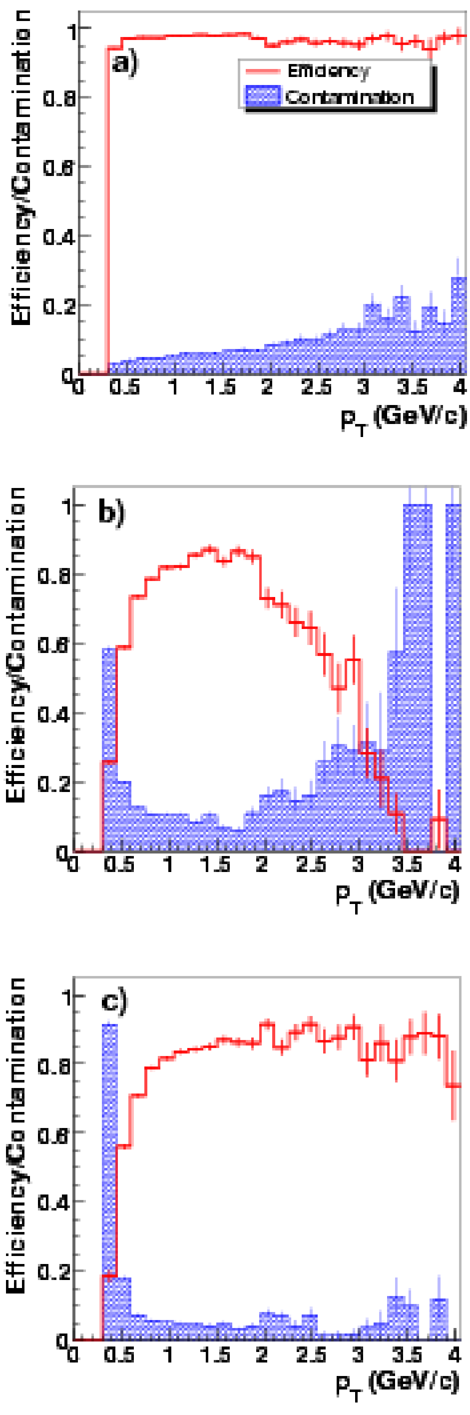

Figure 3.17: Efficiency and contamination for the TOF particle identification procedure applied to $\sim$ 300 HIJING central events for the three particle species: pions (a), kaons (b) and protons (c).

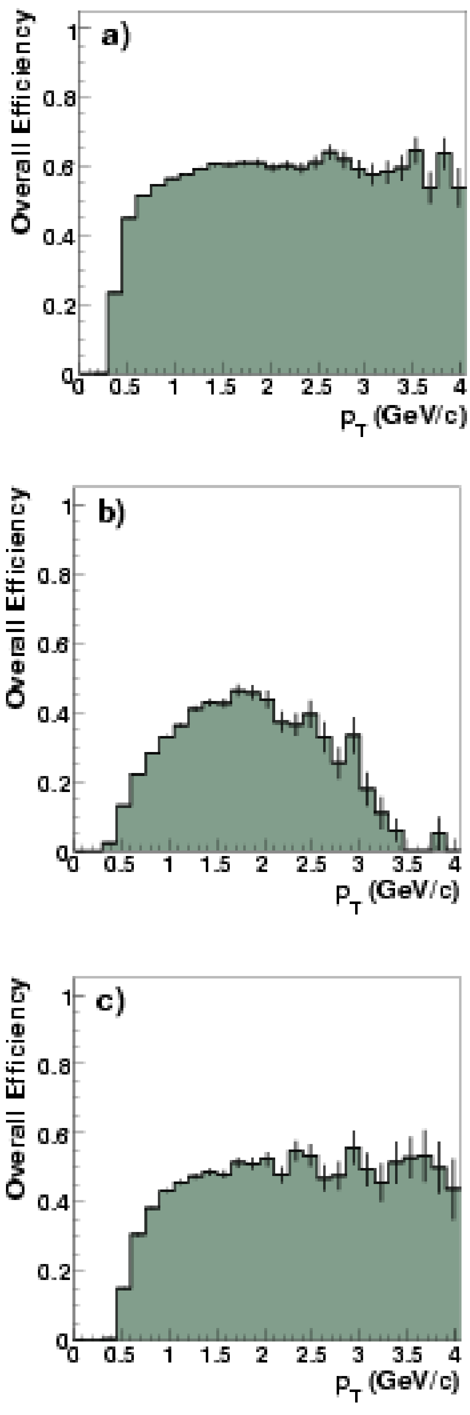

Figure 3.18: Overall efficiency for the TOF particle identification procedure applied to $\sim$ 300 HIJING central events for the three particle species: pions (a), kaons (b) and protons (c).

for protons ($\sim$ 15% over the whole transverse momentum region, $p_T > 0.45$ GeV/c), even if at small p_T it rises up to $\sim$ 90%, especially due to pion mis-identification and because of the very small number of low-p_T protons which can actually reach the TOF. On the contrary, the kaons contamination varies from $\sim$ 20% up to $\sim$ 30% in the interval $0.45 < p_T < 3.45$ GeV/c. At lower transverse momenta, the higher kaon contamination comes especially from pions, while at higher momenta it is a consequence of the reduced TOF separation power.

Figure 3.18 shows the overall TOF PID efficiency for pions, kaons and protons. In Table 3.5 the values of the same overall efficiency integrated over the whole momentum range taken into account for the TOF detector are quoted. As can be observed, with respect to the other detectors (ITS and TPC), the TOF overall efficiency is considerably lower. This is mainly due to the particle losses due to interactions (absorptions) in the material in front of the TOF, that is to say the material of the TRD detector. In fact, this reduces the number of primaries actually reaching the TOF of a factor $\sim 1.5 \div 2$.

Particle species	p_T range (GeV/c)	Overall Efficiency
π	$0.3 < p_T < 4$	39%
K	$0.3 < p_T < 4$	17%
p	$0.3 < p_T < 4$	27%

Table 3.5: TOF particle identification overall efficiency for π, K, and p integrated over the corresponding transverse momentum range.

ITS+TPC+TOF Combined PID

In this section, the results concerning the combined particle identification will be presented, considering all the three detectors, ITS, TPC and TOF. Figure 3.19 shows the performance of the combined PID algorithm (see Sec. 2.2.3 for more details) when applied to the event sample. Comparing Fig. 3.15 with Fig. 3.19, the importance of the TOF role in the particle identification procedure catches one's eye. As far as pions are concerned, the combined PID allows to reduce the contamination from $\sim$ 30% to $\sim$ 20%, while the efficiency still stays around 99%. A significant improvement in the kaon efficiency can be observed as well, with $70 < \varepsilon < 90\%$ in the low transverse momentum region ($0.15 < p_T < 0.75$ GeV/c), and an almost constant value $\varepsilon \sim 60\%$ up to $p_T < 3$ GeV/c. At higher transverse momenta, a decrease in the kaon efficiency occurs, since the TOF

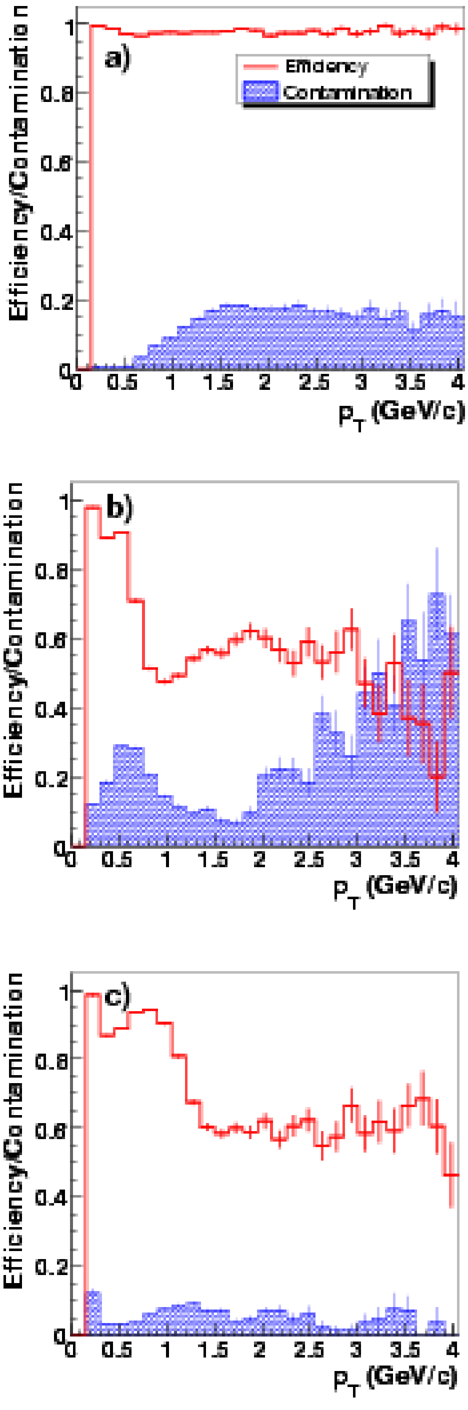

Figure 3.19: Efficiency and contamination for the combined ITS+TPC+TOF particle identification procedure applied to ~ 300 HIJING central events for the three particle species: pions (a), kaons (b) and protons (c).

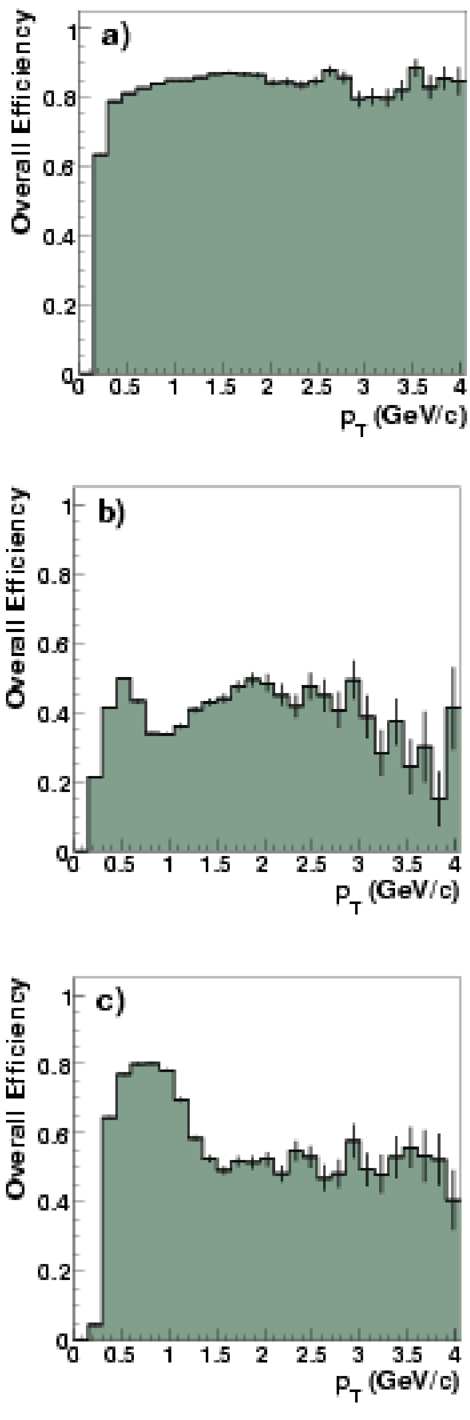

Figure 3.20: Overall efficiency for the ITS+TPC+TOF combined particle identification procedure applied to $\sim$ 300 HIJING central events for the three particle species: pions (a), kaons (b) and protons (c).

kaon identification in this region suffers from a reduction in the separation power of the detector. Nevertheless, an efficiency gain of a factor 1.5 with respect to ITS+TPC particle identification can be found. For what concerns protons, at low momenta ($p_T < 1.3$ GeV/c) the efficiency ranges from 70 to 90%, while at intermediate and high p_T, it remains almost constant at a value of $\sim 60\%$.

		Overall Efficiency	
Particle species	p_T range (GeV/c)	ITS+TPC	ITS+TPC+TOF
π	$0.15 < p_T < 4$	75%	75%
K	$0.15 < p_T < 4$	31%	39%
p	$0.15 < p_T < 4$	61%	66%

Table 3.6: ITS+TPC+TOF combined particle identification overall efficiency for π, K, and p integrated over the corresponding transverse momentum range.

On the other hand, while the contamination for pions and protons is still very low ($\leq$ 15%, and $\leq$ 10% for π and p respectively), in the case of kaons it is limited to $\sim 30\%$ up to $p_T < 3$ GeV/c, but then it increases up to $\sim 65\%$ at $p_T \sim 4$ GeV/c. This is a consequence of the combined particle identification technique, which requires that a particle is identified by *at least* one detector, such that the contamination coming from mis-identified particles in the TPC arises and almost dominates. Such a drawback in the criterion applied to select the particle for the PID procedure is compensated by the advantage of an increased overall efficiency (see Fig. 3.20), crucial when carrying out studies on an event-by-event analysis. Anyway, since the E-by-E analysis which will be presented in the following sections mainly concentrates on identified charged particles in a limited transverse momentum range (up to $p_T \sim 2.5$ GeV/c), the large kaon contamination at high momenta becomes less important. Table 3.6 shows the overall efficiency values for π, K and p integrated over the whole momentum region. The same overall efficiency obtained from the ITS+TPC combined PID (see Table 3.4) is reported in order to emphasize the particle identification role of the TOF detector..

For a summary, Table 3.7 quotes the efficiencies and contaminations for the three particle species obtained from the stand-alone PID procedures for the ITS, TPC and TOF detectors, together with the results of the combined PID (ITS+TPC, and ITS+TPC+TOF) techniques, integrated over the corresponding transverse momentum ranges.

Moreover, it is important to derive the average number of particles of different species

	Efficiency ε			Contamination C		
	π	K	p	π	K	p
ITS	97%	61%	79%	4%	41%	13%
TPC	$<$ 100%	48%	70%	5%	13%	2%
ITS+TPC	98%	31%	79%	3%	27%	6%
TOF	96%	68%	75%	4%	17%	10%
ITS+TPC+TOF	98%	76%	86%	2%	22%	5%

Table 3.7: Efficiencies and contaminations for π, K, and p using the stand-alone detector PID procedures and the combined tecniques, integrated over the corresponding momentum ranges (see text for more details).

	π	K	p
N_{id}	5163	357	263
$N_{\mathrm{id,true}}$	5058	277	250
$N_{\mathrm{id,wrong}}$	105	80	13

Table 3.8: Average numbers of identified pions, kaons and protons per event. The distinction among the correctly ("true") and the uncorrectly ("wrong") identification is reported.

that can be identified per event by the combined PID technique. Table 3.8 quotes the number of pions, kaons and protons which are identified in a Pb+Pb central collision (the numbers are mean values over $\sim$ 300 events). As one can see, even in the case of kaons and protons, there is a considerably high number of identified particles. This will make ALICE the first experiment able to perform event-by-event fluctuation analysis also for hadron species other than pions, with a higly efficiency PID and over a wide momentum range.

3.3.3 Temperature Fluctuations in ALICE

Temperature Fluctuation Results

As already said, thanks to the excellent particle identification capabilities of the ALICE experiment discussed in the previous section, and to the large number of charged particles per event that will be identified by ALICE in central Pb+Pb collisions, an analysis of the event-by-event temperature fluctuations will be feasible.

Figure 3.21 shows the transverse momentum particle spectra separately for pions, kaons and protons obtained for the 300 HIJING central event sample described in Sec. 3.3.1. The distributions referred to as *identified* have been obtained with the combined particle identification procedure presented in Sec. 3.3.2. The labels *true* and *wrong* refer to correctly identified and mis-identified particles, respectively. From the shape of the spectra it is possibile to infer that an exponential fit to the distributions as discussed in Sec. 3.2.7 is a reasonable choice. For this reason, an event-by-event fitting procedure has been applied to the event sample, using for the particle transverse momentum spectra an exponential function of the form:

$$\frac{1}{2\pi p_T}\frac{\mathrm{d}^2 N}{\mathrm{d}p_T\mathrm{d}y} = \exp(\mathrm{A} + \mathrm{B}p_T). \tag{3.2}$$

Here A and B are the parameters of the fit. In particular, the B parameter is the inverse of the so-called "effective" temperature T (B$=-1/T$) already discussed in Sec. 3.2.7. So analogously to Eq. 3.1 we can write:

$$\frac{1}{2\pi p_T}\frac{\mathrm{d}^2 N}{\mathrm{d}p_T\mathrm{d}y} \propto \exp(-\frac{p_T}{T}). \tag{3.3}$$

For the sake of simplicity, from now on we will refer to T as to the *temperature* of the distribution.

Figure 3.22 shows the results of the fitting procedure for one of the simulated events. In order to recover the p_T spectra of the charged particles generated in the collision, the transverse momentum distributions of the identified hadrons have been corrected. In particular, two correction factors have been applied. The first (ε) takes into account two "efficiency" contributions: *i*) the limited geometrical acceptance of the detectors (ε_{acc}), implying that not all the generated particles undergo the PID procedure discussed in Sec. 3.3.2; *ii*) the particle identification efficiency ($\varepsilon_{\mathbf{PID}}$), implying that not all the generated particles are correctly identified. The second correction factor (C) is instead related to the possible mis-identification of the charged hadrons ($C_{\mathbf{PID}}$). From now on, the p_T distributions of the identified particles corrected for both efficiency and contamination will be labelled as *reconstructed* spectra. As a result, the relation:

$$\frac{\mathrm{d}^2 N}{dp_T\mathrm{d}y}(\mathrm{reco}) = \varepsilon \times C \times \frac{\mathrm{d}^2 N}{dp_T\mathrm{d}y}(\mathrm{id}), \quad \varepsilon = \varepsilon_{acc} \times \varepsilon_{\mathbf{PID}}, \quad C = C_{\mathbf{PID}} \tag{3.4}$$

holds true. Here "reco" refers to the reconstructed spectra, while "id" stands for the p_T distributions of the identified particles. The efficiency and contamination factors have

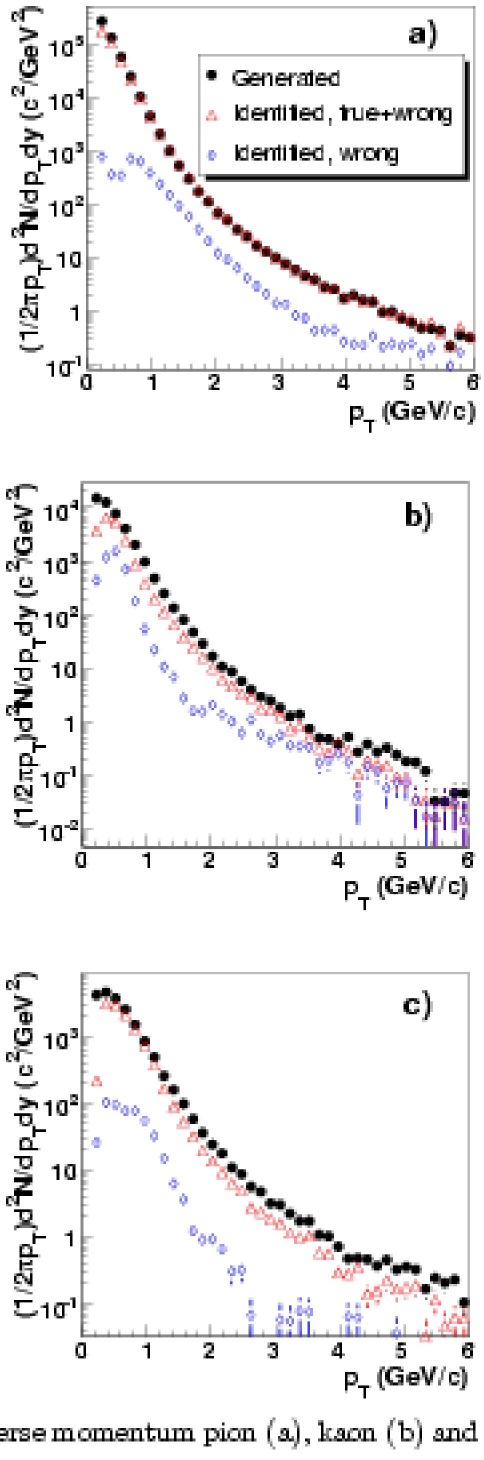

Figure 3.21: Transverse momentum pion (a), kaon (b) and proton (c) spectra for ~ 300 HIJING central events.

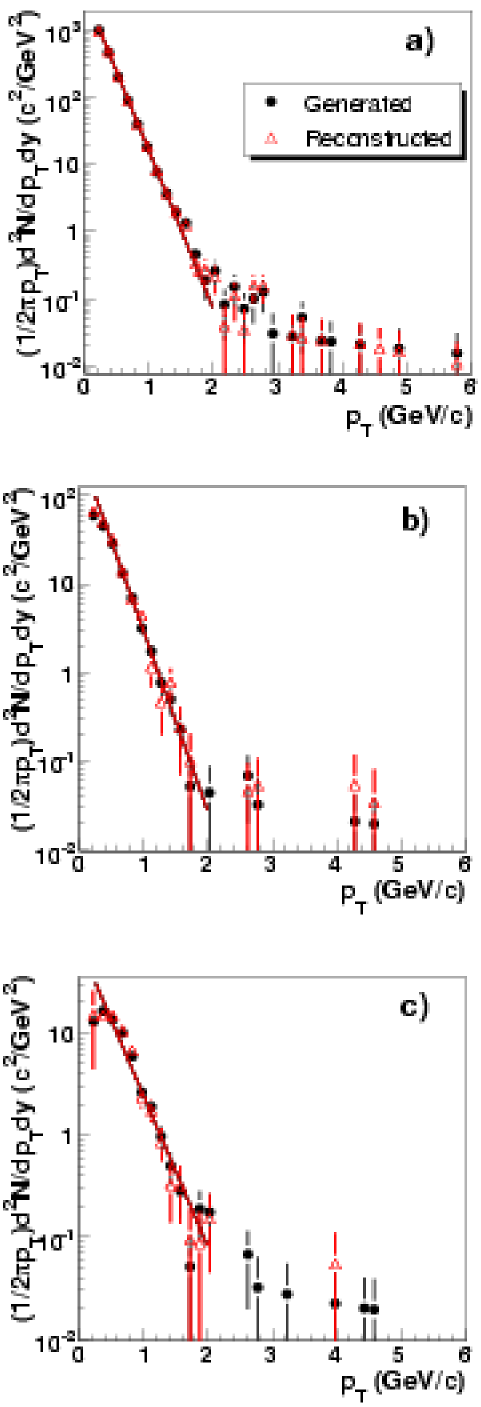

Figure 3.22: Reconstructed (see text) p_T pion (a), kaon (b) and proton (c) spectra for a single HIJING central event with the exponential fits of Eq. 3.2 superimposed. The generated spectra are drawn as well.

been calculated considering the whole event sample under study. In Fig. 3.22, the generated transverse momentum spectra for the three particle species are drawn as well, as reference for the reconstructed spectra.

The fit procedure has been applied for all the three particle species in the transverse momentum range $0.25 < p_T < 2$ GeV/c, which allows a good compromise between the efficiency and the contamination of the combined particle identification algorithm, and which sits below the high p_T region where the exponential form of the p_T spectra is no more expected. In particular, it has been found [121, 122, 123] that only up to $p_T \sim 1.5$-$-$ 2 GeV/c (above which the p_T spectra are expected to follow a power law rather than an exponential) hydrodynamic models are able to well reproduce π, K and p spectra, assuming that thermal equilibrium takes place and that the created particles are affected by a common transverse flow velocity freezing-out at the same temperatire T_{fo}. On the contrary, for $p_T > 4$ GeV/c, the dominant particle production mechanism is the hard scattering described by perturbative QCD, which produces particles from the fragmentation of energetic partons, and here a more detailed analysis has still to be performed.

Figure 3.23 shows the distributions of the temperatures obtained for the ~ 300 HIJING reference event sample, for pions, kaons, and protons. The results of the Gaussian fits performed over the temperature distributions relative to the reconstructed hadron p_T spectra are shown together with those relative to the generated distributions. Table 3.9 summarizes the results. A good agreement can be observed among the mean temperature values obtained considering the p_T distributions of the generated primaries, and the reconstructed ones. A small difference remains, probably due to the fitting procedure of the spectra which, in fact, are not rigorously exponential.

It could be interesting to compare the results obtained in this analysis with the data from recent experiments, such as those from the PHENIX experiment in Au+Au collisions at $\sqrt{s_{NN}} = 130$ and 200 GeV [21, 121]. Nevertheless, the results presented in [21, 121], which show higher temperature values, refer to inclusive identified particle spectra, and not to an event-by-event analysis, which has not yet been carried out by any heavy-ion collision experiment, but which will be feasible with ALICE, as shown in this Section. Moreover, the analysis presented here is a simulation aimed at investigating the capabilities of ALICE in terms of E-by-E fluctuations studies. As a consequence, such a comparison with existing experiments should take into account the fact that the HIJING Monte Carlo generator may not include some physical effects that instead could occur in real collisions. Finally, the slightly different ranges chosen for the fitting procedure could also be responsible for further differences.

Figure 3.24 shows the distributions of the errors on the determination of the temper-

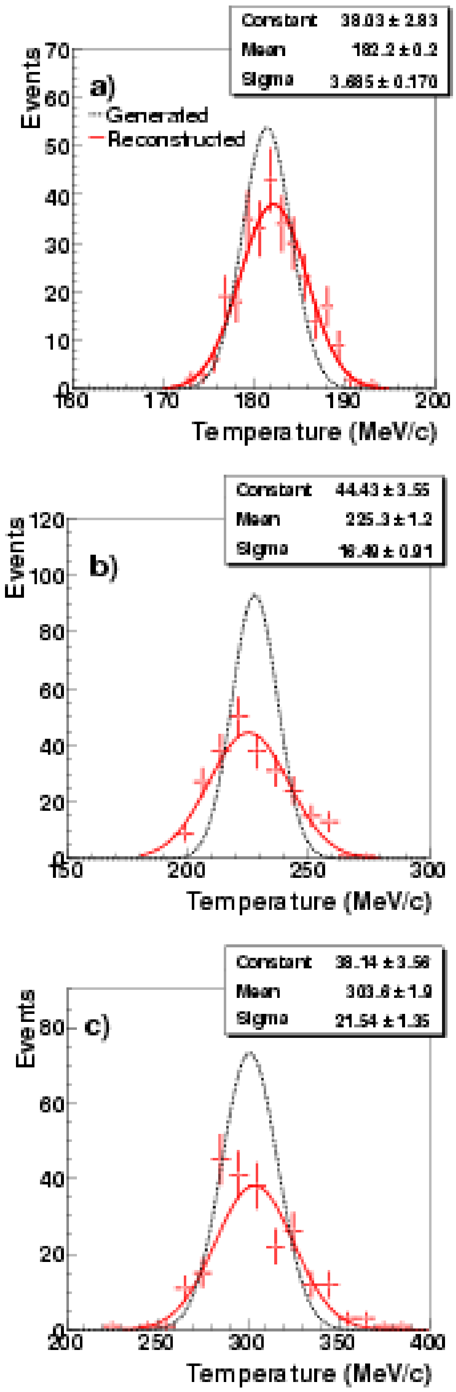

Figure 3.23: Temperature distributions for reconstructed π (a), K (b) and p (c) spectra. The Gaussian fits of the T distributions from reconstructed and generated spectra are superimposed. The fit parameters obtained for reconstructed hadron spectra are reported in the top right panels.

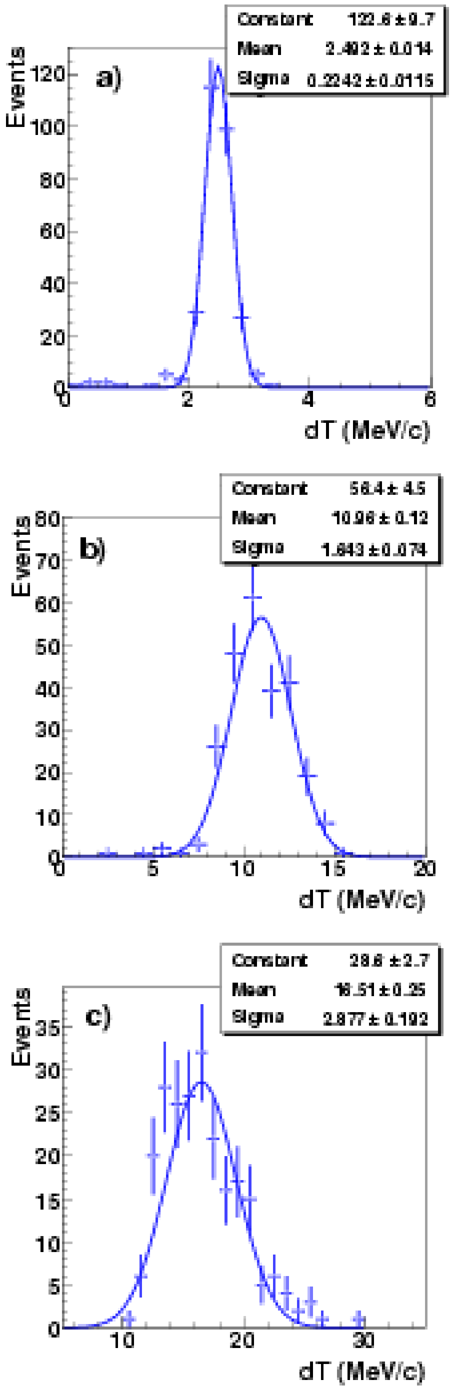

Figure 3.24: Distributions of the errors on the temperatures for recontructed pion (a), kaon (b) and proton (c) spectra. The Gaussian fits of the distributions are superimposed, and the resulting fit parameters are reported.

Particle Species	$\langle T \rangle$ Generated (MeV/c)	$\langle T \rangle$ Reco (MeV/c)	$\sigma(T)$ Reco (MeV/c)
π	181.5 ± 0.2	182.2 ± 0.2	3.7 ± 0.2
K	227.8 ± 0.5	225.3 ± 1.2	16.5 ± 0.9
p	301.0 ± 0.9	303.6 ± 1.9	21.5 ± 1.4

Table 3.9: Mean temperature values obtained from the Gaussian fits of the p_T distributions for generated and reconstructed π, K and p.

ature parameter from the fitting of the transverse momentum spectra distributions for reconstructed pions, kaons and protons. Even if for each event the intrinsic value of dT is from a statistical origin, the mean value of the dT distributions is compatible with the width of the temperature distributions, as expected.

As a conclusion, the analysis has shown that the ALICE experiment will be able to perform temperature fluctuation studies on an event-by-event basis, with a precision of the order of the 2% for identified pions, and of 7% for both kaons and protons (see Table 3.9). Any observed fluctuations larger than these values, if not from a known statistical or systematic origin, could be the searched clue for the formation of the QGP.

Temperature Fluctuation Uncertainties

The uncertainty on the results from event-by-event studies is largely due to the limited number of particles which are taken into account. For this reason, this kind of analysis has only recently got a footing with the advent of ultra-relativistic heavy-ion collision experiments, capable of producing a large amount of particles ($\mathbf{O}(10^3)$) per event.

Apart from statistical errors, there are other sources of uncertainties, such as the geometrical acceptance of the detector, in-flight decays, the effects of multiple scattering, the nuclear interactions with materials in the detectors, and weak decays. Moreover, p_T cuts applied in the PID algorithm, or in the analysis, and the efficiency and contamination of the particle identification procedure can affect the observed particle spectra.

The results presented in the previous Section have been obtained considering uncertainties of statistical origin only. In order to estimate at what extent the systematic errors on the efficiency and contamination correction factor could affect the results, a study concerning a possible variation of the 10% of these correction factors has been performed. The choice of the 10% level for the systematic uncertainty has been driven by the recent results from experiments similar to ALICE, such as, for example, PHENIX [21, 121].

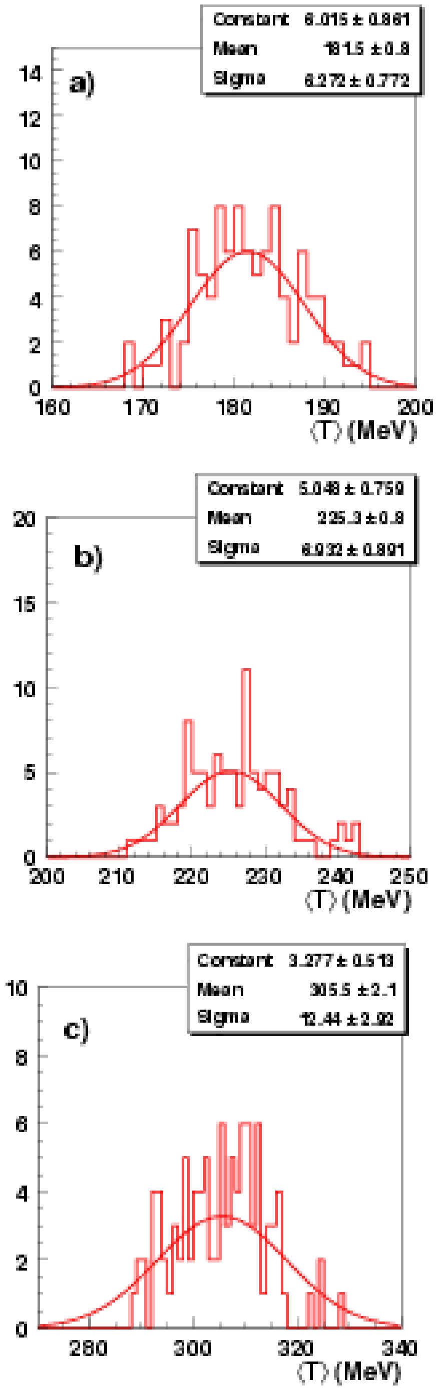

Figure 3.25: $\langle T \rangle$ distributions for the reconstructed pions (a), kaon (b) and proton (c) spectra obtained in the 100 *virtual* experiments relative to the efficiency factor. The Gaussian fits of the distributions are superimposed and the resulting parameters reported.

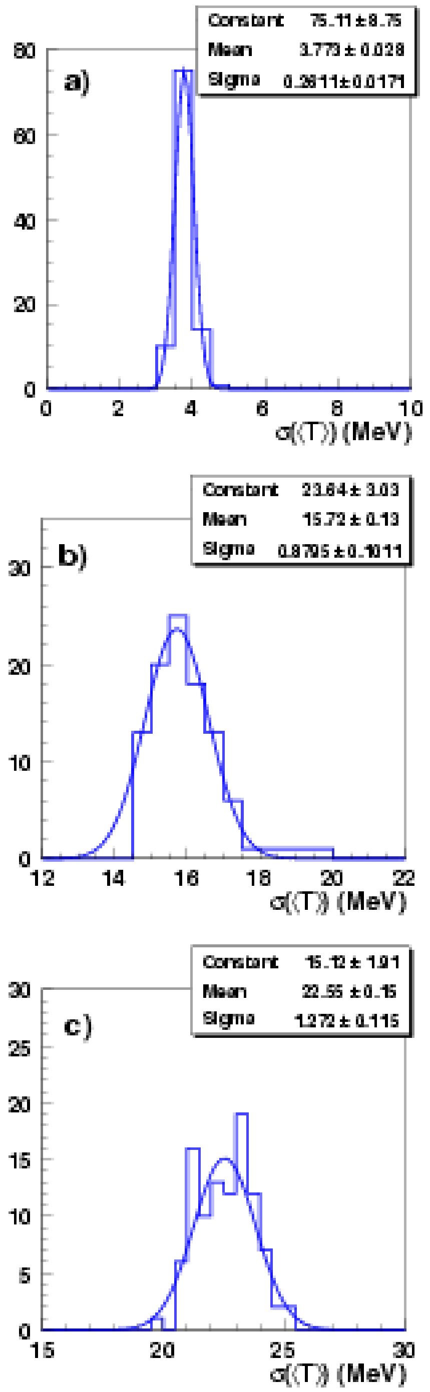

Figure 3.26: $\sigma(\langle T \rangle)$ distributions for the reconstructed pions (a), kaon (b) and proton (c) spectra obtained in the 100 *virtual* experiments relative to the efficiency factor. The Gaussian fits of the distributions are superimposed and the resulting parameters reported.

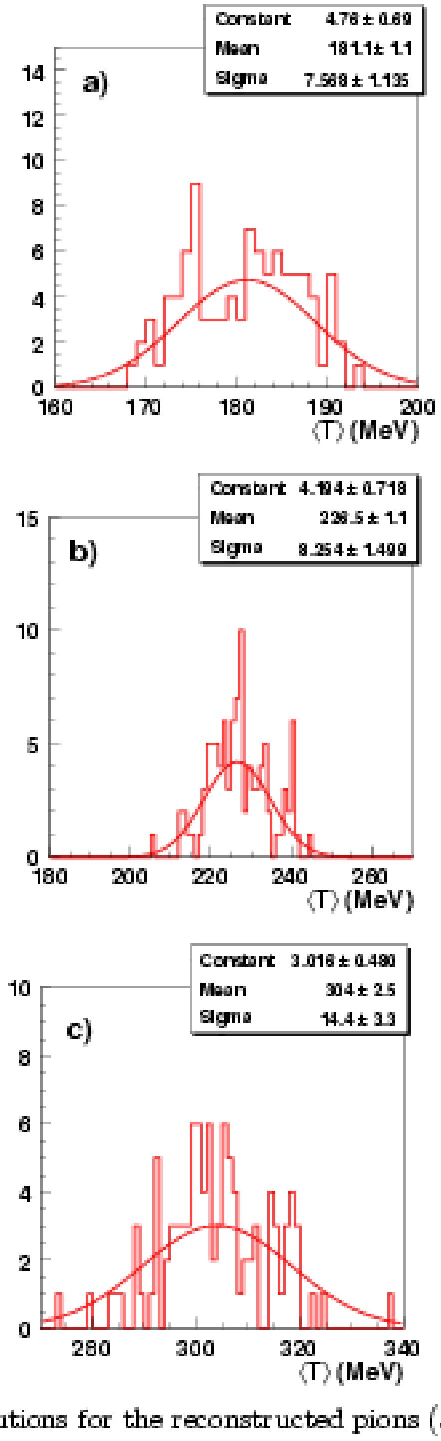

Figure 3.27: $\langle T \rangle$ distributions for the reconstructed pions (a), kaon (b) and proton (c) spectra obtained in the 100 *virtual* experiments relative to the contamination factor. The Gaussian fits of the distributions are superimposed and the resulting parameters reported.

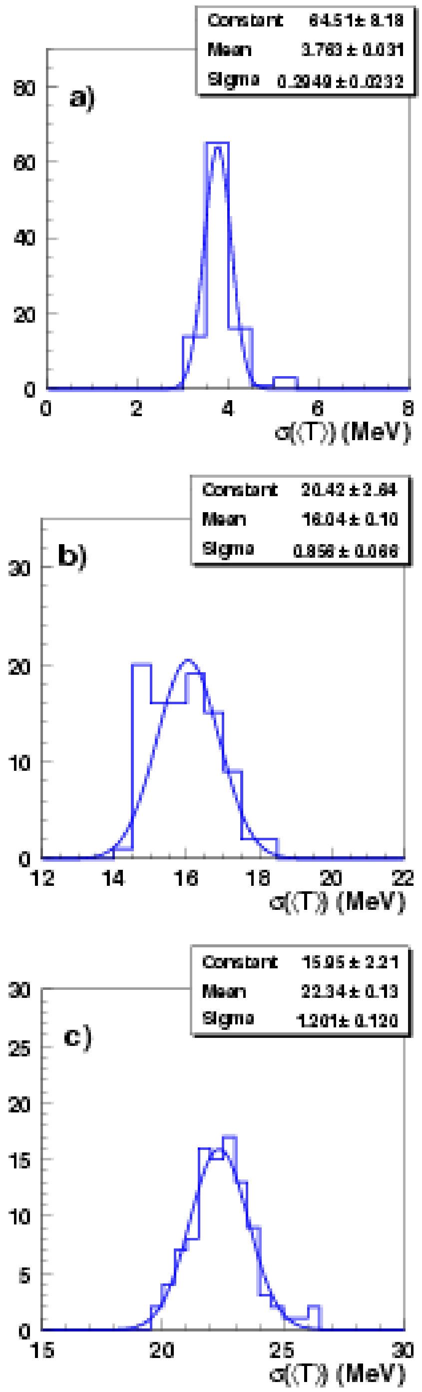

Figure 3.28: $\sigma(\langle T \rangle)$ distributions for the reconstructed pions (a), kaon (b) and proton (c) spectra obtained in the 100 *virtual* experiments relative to the contamination factor. The Gaussian fits of the distributions are superimposed and the resulting parameters reported.

The strategy adopted to study the systematic uncertainty effects on the transverse momentum distributions has taken into account the fact that since the efficiency and contamination correction factors are multiplicative (see Eq. 3.4), a constant variation along the whole spectra would not change the results of the fit in terms of temperature, but would simply act as a scaling. For this reason, 100 *virtual experiments* have been carried out. Each time, for each p_T bin, a random efficiency (contamination) value was extracted from a simulated Gaussian distribution centred at the corresponding "fiducial" efficiency (contamination) value, with a standard deviation σ equal to 10% of the "fiducial" value itself. The new efficiency (contamination) factor was then applied bin per bin to the identified particle p_T spectra.

The results of the systematic uncertainty analysis for the efficiency factor on E-by-E temperature fluctuations are reported in Figures 3.25, 3.26. In the first, the distributions of the mean temperature values $\langle T \rangle$ of the Gaussian fits to the temperature distributions obtained for the 100 *virtual experiments* are shown, while Fig. 3.26 presents the standard deviations $\sigma(\langle T \rangle)$ for the same fits. The same results are reported in Figures 3.27 and 3.28 for the systematic uncertainty analysis on the contamination factors.

As one can see, no significant change in the mean values of the distributions occurs, either in the case of a 10% variation of the efficiency factor or in that of an analogous variation of the contamination factor. Similarly, the σ of the distributions reflecting the precision with which the temperature value can be know are not dramatically affected by systematic uncertainties.

3.3.4 Particle Ratio Fluctuations in ALICE

Besides the event-by-event temperature fluctuation analysis, the particle identification skill of the ALICE experiment will make it possible also to study particle ratios, in particular K/π and p/π ratios. Figure 3.29 shows the result of the E-by-E particle ratio study performed on the ~ 300 HIJING reference events. As in the case of temperature fluctuations, the particle identification has been performed with the combined PID algorithm (see Sec. 3.3.2), and the identified particle spectra have been corrected for efficiency and contamination as described in Sec. 3.3.3. The Gaussian fits to the reconstructed particle ratios distributions are superimposed, as well as the Gaussian fits to the generated ones. Table 3.10 quotes the results of the fits for the generated and reconstructed particles. As one can see, the results agree with each other within the errors.

The intrinsic value of the particle ratios would be important in order to determine the chemical freeze-out temperature, along with the baryon density potential. On the other

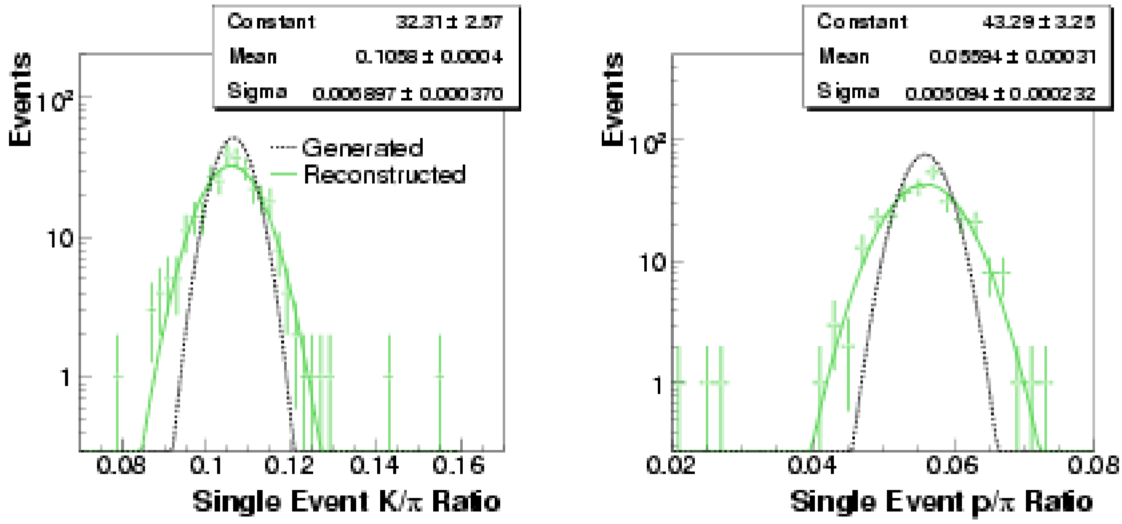

Figure 3.29: K/π and p/π particle ratios for generated and reconstructed particles in the reference event sample. The parameters of the fit to the reconstructed particle ratios are reported in the top right panel.

Particle Ratio	Generated Ratio	Reco Ratio	σ Reco Ratio
K/π	0.1063 ± 0.0003	0.1058 ± 0.0004	0.0069 ± 0.0003
p/π	0.0558 ± 0.0002	0.0559 ± 0.0003	0.0051 ± 0.0002

Table 3.10: K/π and p/π particle ratios for generated and reconstructed particles.

hand, the width of the distribution of the E-by-E particle ratios would be meaningful in order to understand whether a new state of matter has been created during the collision. In this sense, future experimental deviations from the results obtained in this analysis, in which no QGP is simulated would be very interesting and meaningful.

As a conclusion, particle ratio fluctuation analysis will be feasible with the ALICE detector with an uncertainty of the order of $\sim 4\%$ and $\sim 5\%$ for K/π and p/π respectively. If a width in the particle ratio distributions larger than that foreseen according to this analysis with no further apparent statistical or systematic origin will be experimentally observed, then this would contribute to the likely interpretation of the creation of a new state of matter.

Finally, it is worth to say that the systematic uncertainty studies carried out for temperature fluctuations, in the case of particle ratios have not be performed, since in this case, any change in the efficiency and contamination (multiplicative) factors would cancel out in the ratio.

3.3.5 dN_{ch}/dy Dependence

The results presented so far have been obtained assuming a charged particle multiplicity density per unit rapidity $dN_{ch}/dy \sim 4500$ (for central Pb+Pb collisions), which derives from the HIJING Monte Carlo generator. The most recent studies have suggested lower values for dN_{ch}/dy, considering also the results from RHIC. The limit value of $dN_{ch}/dy \sim 1500 \div 2000$ [68, 69] would imply a reduction of a factor $\sim 2 \div 3$ in the observed number of charged particles, and, in turn, an increase of a factor $\sim \sqrt{2} \div \sqrt{3}$ in the uncertainties on the E-by-E determination of the temperatures and particle ratios. Nonetheless, even in the case of a lower multiplicity, the number of identified π, K and p would still remain high enough to perform studies on an event-by-event basis, both in terms of temperature and of particle ratio fluctuations.

On the other hand, a lower charged particle multiplicity would allow to obtain a better performance as far as track reconstruction and particle identification are concerned (see [76]), thus limiting (more than compensating) the negative effect of the smaller statistics available. Moreover, if at $p_T \gtrsim 1.5$ GeV/c the relative particle concentrations of π, K and p become comparable (as suggested from the recent results at RHIC [21]), the PID performance would substantially improve, especially for kaons and protons. As a consequence, the uncertainties on temperature and particle ratio measurements would be significantly reduced.

3.3.6 Further Remarks

To conclude this Chapter, a brief comment on the TOF detector role will be given.

As shown in Sec. 3.3.2, the use of the combined particle identification technique is fundamental in order to maximize the transverse momentum range over which the PID can be applied, with a satisfactory compromise between efficiency and contamination. Obviously, the simultaneous use of different PID information coming from different detectors can slightly deteriorate the performance of the single detectors, when the ranges in which they can provide particle identification do not overlap and even clash.

A special remark has to be made about the Time Of Flight system. The TOF is the detector devoted to charged particle identification in the low and intermediate transverse momentum range ($p_T < 4$ GeV/c). As a consequence, it plays a fundamental role in the combined PID procedure, not only increasing the number of particles which can be identified (which is true every time a detector takes part in the particle identification), but also allowing to cover a wider p_T range during the PID. In turns, the TOF particle identification capability affects at a large extent the E-by-E fluctuation analysis. Besides increasing the particle multiplicity, it allows to take into account a transverse momentum range wider than that the only ITS and TPC would be able to cover which is crucial in the particular case of temperature fluctuations.

An analysis dedicated to the TOF particle identification role in event-by-event studies has also been carried out[3]. It has shown that even if the width of the temperature and particle ratio distributions and the uncertainties related to the mean values are larger than in the combined PID case (because of the smaller particle sample considered), the Time Of Flight is decisive especially for the particle transverse momentum spectra analyses.

[3]The results of the E-by-E analysis using the only TOF detector PID information are not presented in this thesis, for which the choice was made to emphasize the quality of the whole ALICE detector performance.

Chapter 4

The Time Of Flight Detector Calibration

One of the main tasks when dealing with an experiment is the calibration of the measurement instruments. Calibration is an essential procedure in order to make the instrument work, hence to obtain a measurement as precise as possible of the quantity one is interested in; in other words, it is essential to make the instrument resolution as small as possible.

In high-energy physics experiments, the calibration process is very delicate, since it requires to deal with very large and complicated detectors. In particular, the hardware complexity of the whole experiments, and their more and more ambitious physics programs make calibration a crucial procedure to be carefully studied and developed.

As shown in the previous Chapter, as far as the ALICE physics program is concerned, a precise particle identification is required. This implies that the detectors devoted to PID should be characterized by an excellent resolution, and, in turns, that thorough calibration algorithms should be provided. In this Chapter, the calibration procedure developed for the Time Of Flight detector will be discussed.

4.1 The Time Of Fligth Detector Resolution

As already said in Sec. 2.2.2, the Time Of Flight detector resolution σ_{TOF} is the result of different contributions. In particular,

$$\sigma^2_{\mathrm{TOF}} = \sigma^2_{\mathrm{MRPC}} + 2\sigma^2_{\mathrm{TDC}} + \sigma^2_{\mathrm{Cal}} + \sigma^2_{\mathrm{Clock}} + 2\sigma^2_{\mathrm{CTTRM}} + \sigma^2_{\mathrm{T0}}, \tag{4.1}$$

where $\sigma_{\rm MRPC}$ is the detector intrinsic resolution, $\sigma_{\rm TDC}$ is the HPTDC resolution[1], $\sigma_{\rm Cal}$ is the channel-to-channel calibration uncertainty, $\sigma_{\rm Clock}$ is the clock[2] distribution jitter via the TTC system[3], $\sigma_{\rm ClTRM}$ is the jitter introduced when distributing the clock in the TRM[4], and $\sigma_{\rm T0}$ is the uncertainty on the beam-beam (nucleus-nucleus or nucleon-nucleon) collision time (see [84] for more details). Table 4.1 quotes the values of the different sources of uncertainty used for the simulation for the results presented in Sec. 2.2.2, as well as for the ~ 300 HIJING central events analyzed in Chapter 3.

$\sigma_{\rm TOF}$	$\sigma_{\rm MRPC}$	$\sigma_{\rm TDC}$	$\sigma_{\rm Cal}$	$\sigma_{\rm Clock}$	$\sigma_{\rm ClTRM}$	$\sigma_{\rm T0}$
80 ps	40 ps	20 ps	30 ps	15 ps	10 ps	50 ps

Table 4.1: Values of the individual contributions to the Time Of Flight resolution used for the results presented in Chaps. 2 and 3.

It is worth to say that the value reported in Table 4.1 for what concerns the start time of the collision ($\sigma_{\rm T0}$) is, in fact, a conservative estimate used for this simulation (see Sec. 4.2.10). Besides, better resolutions are likely to be obtained for the electronics (in particular, $\sigma_{\rm Clock}$ and $\sigma_{\rm ClTRM}$). This would further improve the Time Of Flight detector resolution.

4.2 The TOF Calibration

The $\sigma_{\rm Cal}$ value reported in Table 4.1, related to the knowledge of the channel-to-channel relative timing and time slewing effect corrections, is expected to be obtained by online-

[1] The High Performance TDC (HPTDC) ASIC chip [124] will be used to digitize the data for the TOF system. It is characterized by multi-hit and multi-event capabilities, providing relative time measurement of each hit at external trigger arrival.

[2] The clock is the LHC signal defining the bunch crossing time. It will be distributed to all the LHC experiments through optical fibres using the TTC system. The frequency of the clock will be 40.079 MHz.

[3] The Trigger Timing and and Control (TCC) system will be encharged of distributing the LHC reference clock and trigger signals to all the different components of the LHC experiments. To guarantee a low jitter in the distribution of the clock to those components requiring a high-precision time reference (such as the TOF), dedicated lines using single-mode optical fibres will be used. The expected jitter of this high-quality clock will be ~ 20 ps.

[4] The TDC Readout Modules (TRM) will digitize the time information of the hits. Each TRM will be made up of 30 HPTDCs.

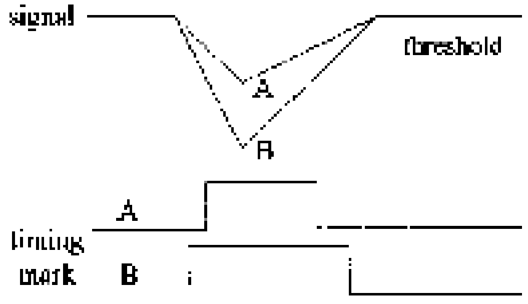

Figure 4.1: Time slewing effect: variation of timing marks due to amplitudes.

offline procedures. In the following Sections, the offline algorithm developed in order to limit as much as possible σ_{Cal}, that is the TOF calibration algorithm, will be presented.

4.2.1 The Time Slewing Effect

The TOF calibration procedure has to take into account different kinds of time delays, such as the delays due to cable lengths and those introduced by electronics. With respect to this, time slewing effects are the major contribution to the deterioration of the time information, coming along with the time jitter due to noise and statistical fluctuations.

As in the majority of the Time Of Flight detectors, the ALICE TOF system makes use of leading-edge discriminators (LED). One of the most peculiar features of the LED technology is that this type of discriminator provides a timing mark at the very instance the detector signal crosses the threshold level (which is the only parameter to be adjusted, making the set-up very simple). As a consequence, the relative timing of the mark is strongly affected by the amplitude of the signal, which corresponds to the so-called time slewing effect, as shown in Fig. 4.1. To be noted that here, the time signals have been simplified as straight lines in the leading and trailing regions instead of the actual analogic differential shapes. Even if the A and B signals are generated at the same time, they overcome the thershold at different instants, as a consequence of their different amplitudes. As Fig. 4.1 shows, larger signals arrive earlier than smaller ones. This is the so-called time slewing effect and it can be corrected via offline methods in case together with the the timing marks themselves, the amplitudes of the signals are collected as well.

There are many parameters which can be used in order to correct for time slewing, such as signal width, slew rate (how much steep the signal is), and charge amount (corresponding to the signal area) [125]. For the ALICE TOF calibration algorithm presented hereafter, the signal width will be used. It corresponds to the interval between the leading and the trailing edges of the signal, in other words to the *Time over Threshold* (ToT) information.

In the case of the ALICE Time Of Flight detector, after having being amplified and then discriminated by the LED, the signal is shaped to provide a Time over Threshold information, in which the leading edge corresponds to the time of the hit, and the width of the signal depends on how long the signal has stayed over the threshold (which is equivalent to a measurement of the signal amplitude). The time information is then provided by a HPTDC (*High Performance Time to Digital Converter*) chip fed with the signal directly from the output of the discriminator. For more details on the TOF readout system see [84].

4.2.2 The TOF Calibration Algorithm

The TOF calibration algorithm philosophy starts from test beam results. The results from the latest tests carried out during July 2004 at the CERN Proton Synchrotron (PS) facility have been used. In particular, the distributions of the measured times with respect to the corresponding Time over Threshold widths have acted as starting point and basic input for the TOF calibration in order to simulate a time slewing effect as likely as possible. The algorithm has been developed considering in the Monte Carlo simulation well-reconstructed tracks, for which the calculation of the expected time can be sufficiently precise. The use of the expected times (in detail, of the difference between the expected and the measured times) will allow to unfold the spread due to particle momentum spectra, as well as the different responses in terms of flight times of different particle species (particles with different masses would of course take different times to travel along the same distance as shown in Eq. 2.10), as it will be explained in the next Sections. The procedure then consists in the determination of a parametrized correction to be applied to the measured time.

The algorithm performance in terms of σ_{Cal} will be presented, and the results concerning the sensitivity of the algorithm with respect to the number of tracks used for the calibration will be discussed as well.

4.2.3 Statistical Estimates

The TOF calibration goal is to correct the measured times for the time delays introduced by the hardware components of the experiment (mainly cables), and, at the same time, for the time slewing effect due to the use of a LED discriminator. The procedure has to take into account that a huge amount of channels has to be calibrated individually, since each TOF channel is independent of the others.

The number of events necessary for a TOF calibration consistent with the σ_{Cal} value reported in Table 4.1 obviously depends on the number of tracks needed to calibrate each channel, and on the number of "useful" tracks per channel, per event. A track is labelled as "useful" if it satisfies the calibration algorithm requirements that will be described in Sec. 4.2.5 (i.e. if it is a selected track). So, the relation:

$$N_{\mathrm{ev}} = N_{\mathrm{tr}}\frac{1}{k}$$

holds true. Here, N_{ev} is the number of necessary events to obtain the desidered σ_{Cal} value, N_{tr} is the number of needed tracks for that σ_{Cal}, and k is the TOF "useful" track occupancy (how many "useful" tracks there are in one event for each channel). A first rough estimate of N_{ev} can be done. Since from test beams it has been found that ~ 1000 tracks are required to determine sufficiently accurate time slewing corrections, and since in one Pb+Pb central collision there are at most $\sim \mathbf{O}(10^{-3})$ "useful" tracks per channel (strongly depending on the calibration procedure requirements), the number of necessary events would be $\sim \mathbf{O}(10^{6})$. A more refined evaluation will be done further on in this Section, once the calibration algorithm will have been properly taken into account.

In order to know how long it will take to collect a sufficient number of events, the ALICE event rates have to be considered. In particular, since in a typical data-taking scenario the Pb+Pb central event trigger can be acquired at a rate of $\sim$ 10–20 Hz [71], then $\sim$ 1 day of data-taking would be necessary. In the case of p+p collisions (for which a track multiplicity reduction by a factor $\sim \mathbf{O}(10^{3})$ is expected with the same track selection criteria), the much lower number of "useful" tracks in an event would make it harder and more time consuming to have sufficient statistics. Nevertheless, as it will be explained later, also in this case it will be possible to apply the calibration algorithm, with less strict track selection criteria because of the very reduced event multiplicity.

The estimate of the calibration uncertainty can be expressed as:

$$\sigma_{\mathrm{Cal}} = \frac{\sigma_{\mathrm{X}}}{\sqrt{kN_{\mathrm{ev}}}}$$

where X is the calibration parameter chosen, σ_{X} is the resolution on X, and k and N_{ev} are the same as defined above. In the TOF case, the choice has fallen on the difference between the expected time[5], for which the particle identity is obtained thanks to a dedicated

[5] The expected time is calculated for each mass hypothesis m_i ($i = \pi, \mathrm{K}, \mathrm{p}$) during track reconstruction, according to Eq. 2.11.

particle identification procedure, and the measured time. Since in this case $\sigma_X \sim \mathbf{O}(10^2)$ ps[6], with the same values for k and N_{ev} as before, one would then obtain $\sigma_{Cal} \sim \mathbf{O}(10)$ ps, in good agreement with the value assumed in Table 4.1.

4.2.4 Simulation from Test Beam Results

As anticipated at the beginning of this Section, the time slewing effect has been simulated starting from test beam results.

The tests were carried out in July 2004 at the T10 beam line of the CERN PS East Hall using a collimated beam of charged particles (π^- and μ^-) with momentum $p = 7$ GeV/c (see [126, 127] for more details).

Figure 4.2 shows three typical examples of Time over Threshold (i.e. signal width) distributions which have been obtained during the tests. From now on, the three cases will be referred to as case a), case b) and case c), respectively. As it can be observed, the ToT distribution shape can vary, showing one, two, or even three peaks. The peak structure is due to a slight impedance mismatch which may occur in some channels, interfering with the non-linear amplifying characteristic of the front-end ASIC chip [124]. However, as explained in the following, a time slewing correction can be applied in all the three cases.

For analysis convenience, the average arrival time of the tracks (*hit time*) measured during the tests has been shifted to zero. Figure 4.3 shows the distributions of the arrival hit times (centred at zero) vs. ToT, for the three cases. Because of the centering at zero, the distributions show both positive and negative values, and the residuals with respect to zero represent the time slewing effect. The highly populated regions that can be observed correspond to the Time over Thresholds ranges where the peaks seen in Fig. 4.2 lie.

Cases a), b) and c) will be used for the results presented in the following sections in order to simulate the time slewing effects for three different likely experimental scenarios. To be noted that under the real experimental conditions, each channel is expected to behave differently from the others (as they are all independent), in such a way that the time slewing effect will be a peculiar characteristic of each channel. This will result in a necessary *channel-to-channel* calibration dealing with a different time slewing effect for each channel. Anyway, for the sake of simplicity, the results presented in this thesis are based on the assumption that all the channels are affected by the same time slewing (all the three cases a), b) and c) have been tested). As a result, the TOF channels have

[6] σ_X takes into account both the TOF detector resolution and the uncertainty on the track reconstruction.

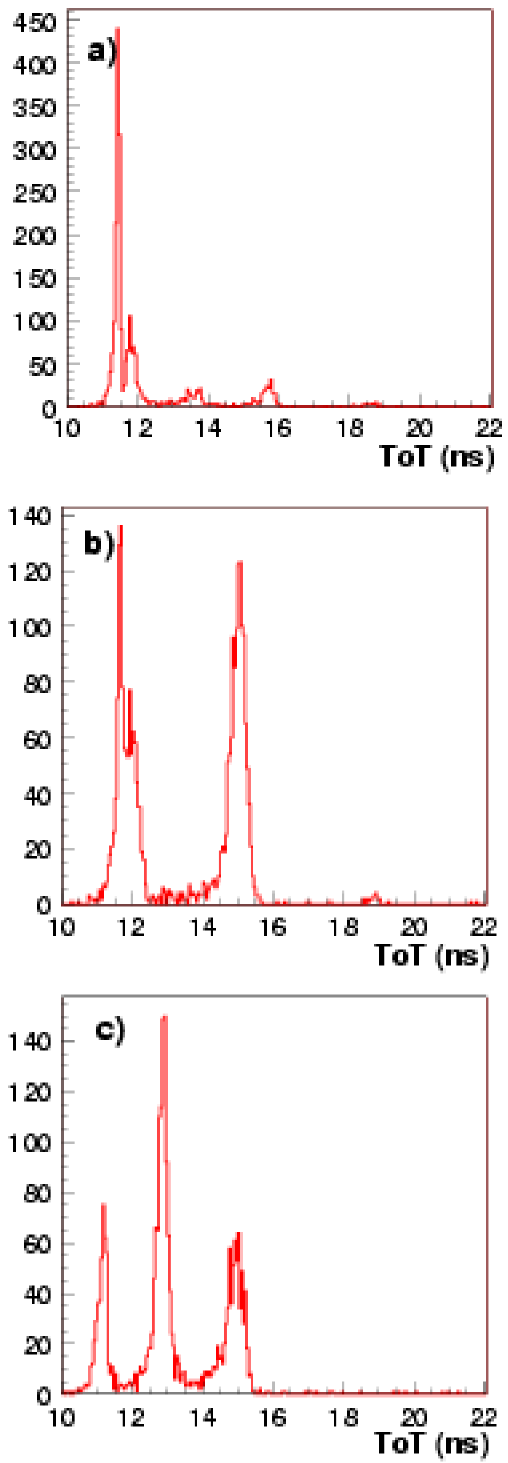

Figure 4.2: Examples of ToT distributions obtained from test beam measurements.

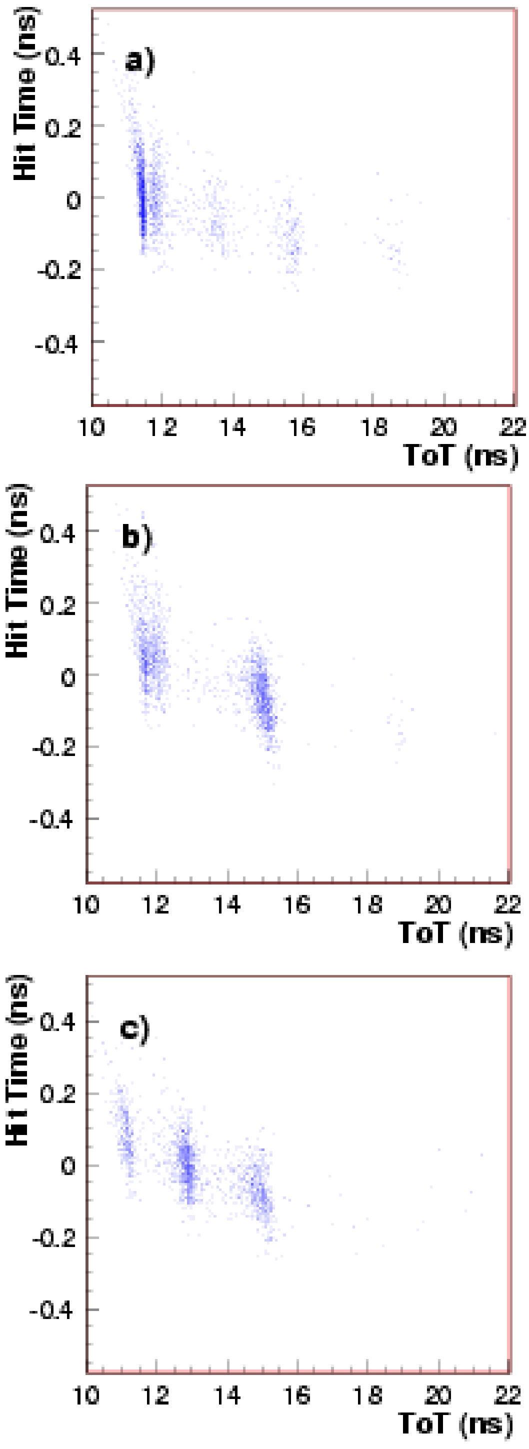

Figure 4.3: Arrival hit time (centred at zero) vs. Time over Threshold distributions for case a), b) and c), as obtained from test beam measurements. The residuals of the hit times with respect to zero correspond to the time slewing effect.

been treated as a whole in order to take advantage of the limited Monte Carlo statistics[7]. However, in the real experiment each channel will be treated individually.

To simulate the time slewing effect from test beam results (case a), b) and c)), for each scenario a function describing the dependence of the measured time slewing from the observed Time over Threshold has been found. In order to do this, a *profiling* procedure has been applied to the distributions in Fig. 4.3, in such a way that for each ToT bin, the mean value of the measured hit times for all the entries falling in that ToT bin has been calculated, provided that at least 20 measurements had fallen within the bin. If this was not the case, then the subsequent bin was merged with the previous one. Figure 4.4 shows the results of such a procedure for the three scenarios. The measured hit time dependence on the ToT (corresponding to the dependence of the time slewing effect on the ToT itself) has been obtained fitting the distributions with a $5^{\mathbf{th}}$-order polynomial function, which well reproduces the data in the ToT range of interest.

In order to develop the TOF calibration procedure, for each scenario (a), b), or c)), the simulation of the time slewing effect has been introduced at the level of digitization for a sample of central ($0 \leq b \leq 5$ fm) HIJING Pb+Pb events. A ToT value has been generated for each track using the *hit or miss* Monte Carlo technique, from the ToT distributions shown in Fig. 4.2. The time slewing contribution has been calculated according to the $5^{\mathbf{th}}$-order polynomial fit performed, then added to the original digitized signal. An additional delay of 2 ns has been introduced, in order to include the simulation of hardware delays. As a result, a *decalibrated* time signal has been associated to each track. The purpose of the following calibration procedure step was to recover the additional delay from the decalibrated times, in order to go back to the original digitized detector signal.

From now on, we will refer to the expected times (obtained with a dedicated particle identification combinatorial algorithm) as $t^{\mathbf{exp}}$, to the simulated original times of flight as $t^{\mathbf{TOF,ND}}$ (where the superscript "ND" stands for "Non Decalibrated"), while the decalibrated times will be labelled as $t^{\mathbf{TOF}}$ (since they represent what will be measured during data taking, i.e. before TOF calibration). Finally, $t^{\mathbf{TOF,cal}}$ will refer to the calibrated (corrected) times.

[7]As a matter of fact, since the Time Of Flight detector will be endowed with $\sim$ 160000 read-out channels, the Monte Carlo statistics necessary to simulate a different time slewing effect for each TOF channel would have been prohibitive.

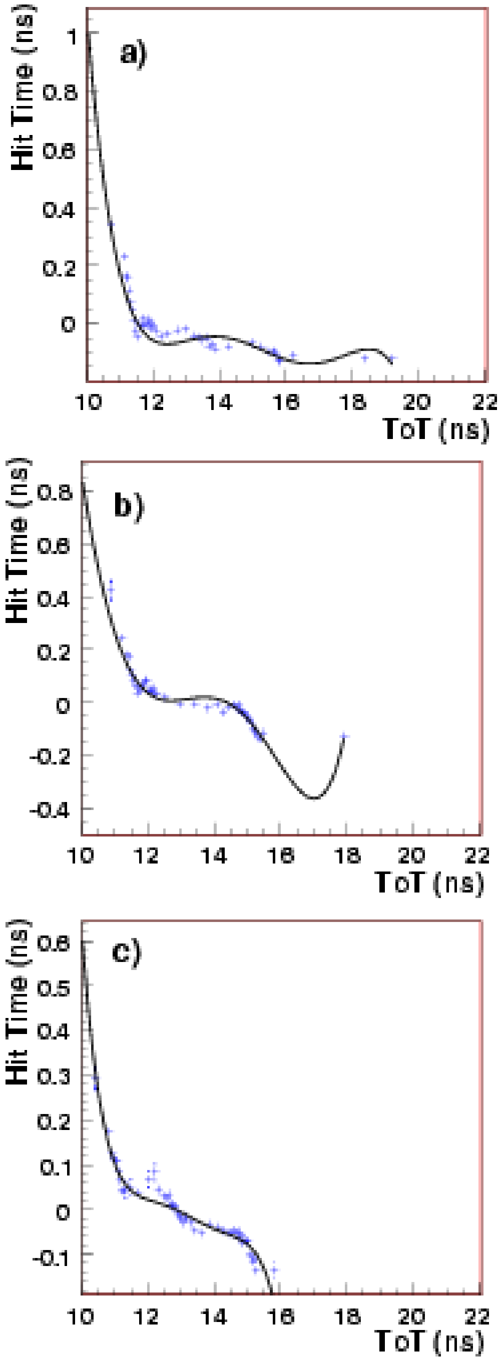

Figure 4.4: Average arrival hit time (centred at zero) vs. Time over Threshold after "profiling" (see text) for case a), b) and c), as obtained from test beam measurements. The residuals of the hit times with respect to zero correspond to the time slewing effect. The 5$^{\mathrm{th}}$-order polynomial fits are superimposed.

4.2.5 Track Selection

As already stated at the beginning of this Section, in order to unfold the time spread due to the momentum distributions and to the different particle masses, the channel-to-channel calibration parameters have been determined using the difference between the expected and the measured times, $\Delta t = t^{\exp} - t^{\rm TOF}$ (where $t^{\rm TOF}$ is obtained after the decalibration procedure). In case of an exact particle identification (which affects the $t^{\exp}$ value) and of a null decalibration (which, instead, affects $t^{\rm TOF}$), the mean value of the distribution of Δt should be centred at zero, with a width determined by the TOF system resolution only. In fact, both particle identification and decalibration introduce a deterioration in the measurement of Δt. On one hand, neither the PID algorithm described in Sec. 2.2.2 (for what concerns the TOF PID), nor that in Sec. 2.2.3 (for what concerns the combined PID technique), can be appplied, since both of them assume TOF time signals not affected by any source of delay. For this reason, an alternative and dedicated particle identification procedure has been studied, which does not rely on the *a priori* knowledge of any information about the TOF time. On the other hand, even in case the particle identities were known, the width of the distribution of Δt would be enlarged by time slewing effects because of a worsening of the time resolution, and its mean value would be shifted because of the delays (both time slewing and hardware delays). The increased time resolution and the residual shifts are exactly what the calibration algorithm has to deal with.

As far as the particle identification is concerned, a combinatorial approach has been chosen, which assigns the particle identity to each track thanks to a χ^2 minimization technique. Since the algorithm relies on reconstructed particles, selection criteria have been defined in order to keep as low as possible mis-identification due to reconstruction defects. So, the TOF calibration procedure starts from a track selection preliminary step. In particular:

1. only tracks which have been propagated up to the TOF detector and which have been associated with a signal on the TOF system are taken into account, as the time of flight information is necessary;

2. tracks with momentum $p < 0.8$ GeV/c are discarded, since in this momentum region the efficiency of the track association with a TOF sensitive volume during reconstruction is too poor (see Sec. 2.2.2);

3. tracks with $p > 1.8$ GeV/c are also excluded, since an optimal separation between the charged hadron species (π, K and p) is easily achievable up to this limit;

4. the tracks are required to have a good extrapolation to the primary vertex[8] in order to ensure a reliable calculation of the expected time;

5. after having determined the minimum time of flight for the subsample of tracks selected so far, those with a time of flight larger than the minumum by more than 5 ns are rejected, in such a way that only the fastest particles (for which the reconstruction performance should be better) are considered.

This subsample of tracks then goes through the combinatorial particle identification procedure described in the following Section.

4.2.6 Combinatorial Particle Identification

The second step of the TOF calibration algorithm is particle identification. Since the corrected times of flight are still not available at this stage (i.e. after decalibration, which corresponds to the initial experimental condition during ALICE runs), a dedicated procedure has to be used. Hence, the algorithm can not rely on the time of flight measurements to assign the particle identity to each track (as Eq. 2.10 would require). Nonetheless, it has to be able to perform particle identification on the selected sample of tracks with high efficiency. In order to do so, a combinatorial approach has been chosen.

After having being ordered according to a momentum hierarchy (such that those tracks with the highest p come first)[9], the selected tracks obtained as described before, are subdivided into sets of N tracks each. For the results presented here, $N = 6$ has been set, as an optimum compromise between the computing CPU time (3^N combinations have to be processed) and the algorithm performance (the more the tracks, the more efficient the algorithm). Then, for each set, a combinatorial PID algorithm based on finding the best combination $C^{best}(m_1, ...m_N)$ on the 3^N mass hypotheses (m_π, m_K, and m_p) is applied, by minimizing the χ^2:

$$\chi^2(C) = \sum_{i=1,...N} \frac{\left[t_i^0(m_i) - \langle t^0(C)\rangle\right]^2}{\sigma_i^2}, \tag{4.2}$$

where $t_i^0(m_i)$ is the start time value for the i-th particle under the hypothesis its mass was m_i:

$$t_i^0(m_i) = t_i^{exp}(m_i) - t_i^{TOF}, \tag{4.3}$$

[8]The efficiency of this extrapolation to the interaction vertex is $\sim 95\%$ for primary tracks.

[9]The momentum ordering is meant to reduce as much as possible the uncertainty on reconstruction, in such a way that the performance of the subsequent combinatorial PID procedure should improve.

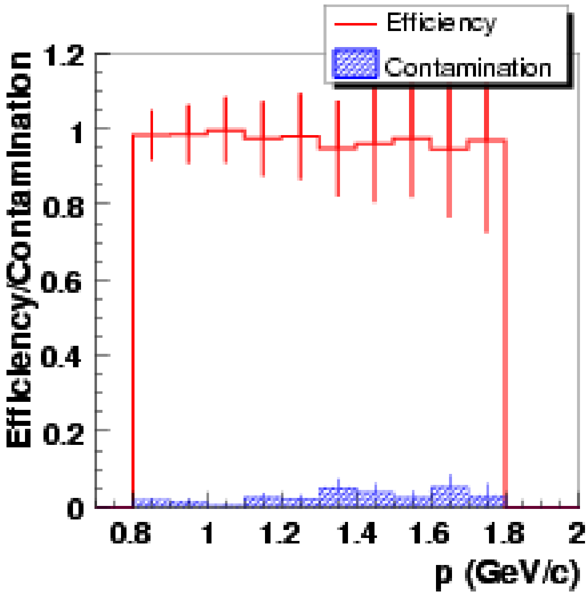

Figure 4.5: Efficiency and contamination as a function of the track momentum for the sample of tracks selected for the TOF calibration procedure.

that is to say, it is the time offset for track i; σ_i is the error on the i-th t^0 offset:

$$\sigma_i^2 = \sigma^2(t_i^{exp}(m_i)) + \sigma^2(t_i^{TOF}), \tag{4.4}$$

and

$$\langle t^0(C)\rangle = \sum_{i=1,...N} \frac{t_i^0(m_i)/\sigma_i^2}{1/\sigma_i^2} \tag{4.5}$$

is the average t^0 offset for the mass combination $C^{best}(m_1, ...m_N)$.

The mass combination corresponding to the minimum χ^2 is then chosen to assign to each track its particle identity. It is worth to say that during the calculation of the χ^2 for the various sets, those sets for which the confidence level (CL) is lower than 1% are discarded. In fact, a detailed study has shown that in those sets for which CL $<$ 1%, the mis-identified tracks are mainly mis-associated tracks (i.e. tracks which have been matched with a wrong TOF signal).

Figure 4.5 shows the efficiency and contamination of the combinatorial PID technique just described. The efficiency is defined as the ratio of the correctly identified particles ($N_{id,t}$), to the total number of identified particles (N_{id}) which will be then used for the TOF calibration,

$$\varepsilon = \frac{N_{id,t}}{N_{id}}.$$

Contamination is the complementary fraction of tracks. The definition used in this case for the efficiency, different from that of Eq. 2.9, is meant to emphasize the quality of the track sample which is selected for the calibration algorithm. That is, since (as it will be explained in the next Section) the expected time calculated from a mass hypothesis for each track is the key parameter, the purity of the sample of selected tracks used in the analysis has to be guaranteed, as it seems to be for the combinatorial PID procedure, according to Fig. 4.5.

4.2.7 Calibration Parameter Determination

Finally, the determination of the calibration parameters has to be performed. The method used for HIJING tracks in order to simulate the time slewing effect is very similar to the one adopted for test beam tracks.

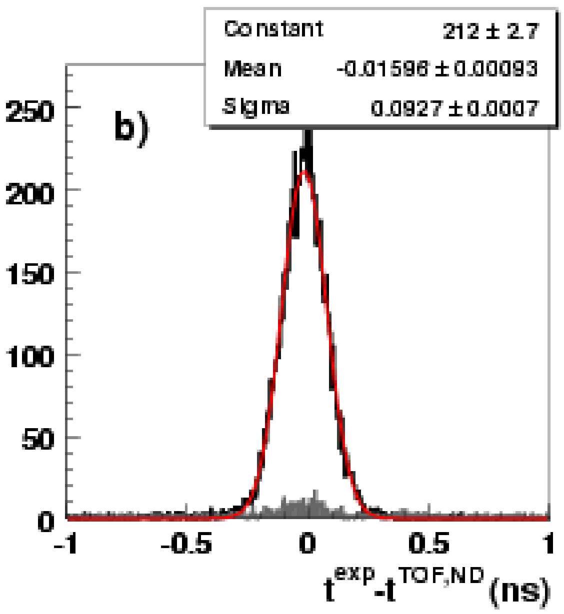

Figure 4.6: Distribution of $t^{exp} - t^{TOF,ND}$ (scenario b)) for well reconstructed tracks correctly associated with a TOF time signal (empty histogram). The Gaussian fit to the distribution is superimposed. The shaded histogram refers to well-reconstructed tracks which are, however, mis-associated to TOF signals. The track selection has been applied to a sample of seven HIJING central Pb+Pb events.

Again, the distributions of the decalibrated times of selected tracks as a function of their simulated Time over Threshold are fitted with a 5^{th}-order polynomial function.

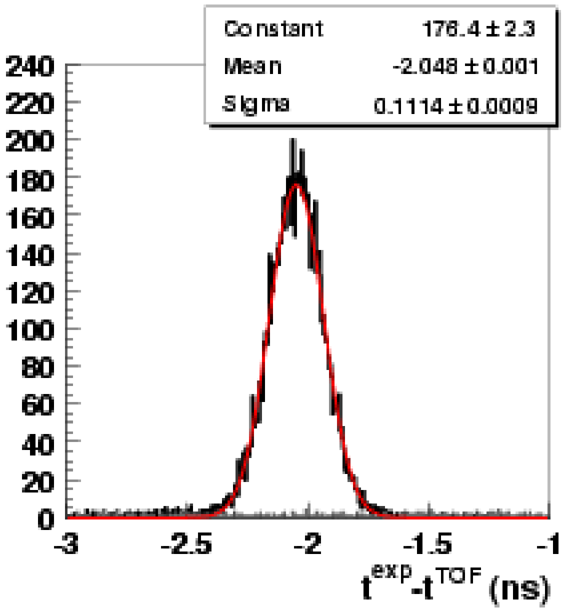

Figure 4.7: Distribution of $t^{exp} - t^{TOF}$ (scenario b)) for well reconstructed tracks correctly associated with a TOF time signal (empty histogram). The Gaussian fit to the distribution is superimposed. The shaded histogram refers to well-reconstructed tracks which are, however, mis-associated to TOF signals. The track selection has been applied to a sample of seven HIJING central Pb+Pb events. The time shift of the mean value with respect to zero corresponds to the 2 ns time delay added to the decalibrated times of flight to simulate hardware delays.

The parameters of the fit are then set as calibration parameters. Under the simplified hypothesis that all the TOF channels are affected by the same time slewing effect (as a consequence of having used in the simulation the same test beam input spectrum for all the channels, were it the spectrum of scenario a), b) or c)), the calibration parameters obtained in this way are considered as effective for all the ~ 160000 TOF read-out channels.

In Fig. 4.6, the difference $t^{exp} - t^{TOF,ND}$ for well reconstructed tracks (satisfying both conditions 1) and 4), see Sec. 4.2.5) for seven simulated HIJING central Pb+Pb collisions is presented. From now on, scenario b) will be taken as a reference as it is well-representative of the real experimental conditions. To be noted that to determine the calibration parameters, a subsamble of only 500 tracks among the selected ones has been used, for which two HIJING Pb+Pb central events have been necessary (see Sec. 4.2.9). Figure 4.7, instead, shows the distribution of the difference between the expected times and the decalibrated times (t^{TOF}) for the same tracks (scenario b)). As one can see, the

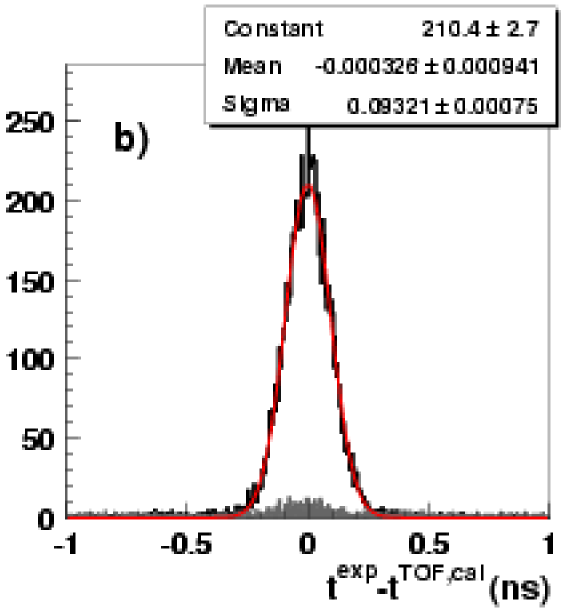

Figure 4.8: Same as Fig. 4.7 for $t^{exp} - t^{TOF,cal}$. In this case, the 2 ns shift of the mean value has disappeared, since the calibration procedure has been able to correct the decalibrated times also for it.

$t^{exp} - t^{TOF}$ distribution is centred at ~ -2 ns, as expected from the fact that an additional constant time delay equal to 2 ns has been added to reproduce the delays due to hardware. In both Fig.s 4.6 and 4.7, the empty histograms refer to tracks which have been associated to the correct TOF time signal during reconstruction, while the shaded histograms show the constribution coming from tracks matched with an uncorrect signal on TOF. The particle identity of the track used to calculate t^{exp} comes from the Monte Carlo simulation information. Superimposed, the Gaussian fit to the correctly associated tracks is shown. While for the distribution in Fig. 4.6 the standard deviation of the Gaussian fit originates both from the TOF time resolution ($\sigma_{TOF} = 80$ ps) and the uncertainty related to track reconstruction ($\sigma_{trabo} \sim 30$ ps), in Fig. 4.7 the time slewing effect contribution sums up. As a result, the width of $t^{exp} - t^{TOF}$ is larger than that of $t^{exp} - t^{TOF,ND}$, as expected. The calibration procedure should be able to recover the time resolution due to σ_{TOF} and σ_{trabo} only. With respect to this, in order to evaluate the performance of the calibration algorithm presented in this Section, the $t^{exp} - t^{TOF,cal}$ distribution is also shown (Fig. 4.8), for the same sample of tracks used for Figs. 4.6 and 4.7.

Table 4.2 summarizes the results of the Gaussian fits applied to the $t^{exp} - t^{TOF,ND}$, $t^{exp} - t^{TOF}$, $t^{exp} - t^{TOF,cal}$ distributions for the three cases, a), b), and c). The last row of

Table 4.2 quotes the residual uncertainties due to the calibration procedure. As one can see, the resolution $\sqrt{\sigma^2_{TOF} + \sigma^2_{t_{zero}}}$ is recovered within ~ 15 ps for all the three scenarios, well below the value used during simulation (see Table 4.1).

σ (ps)	scenario a)	scenario b)	scenario c)
$(t^{exp} - t^{TOF,ND})$	92.7	92.7	92.7
$(t^{exp} - t^{TOF})$	104.9	111.4	106.9
$(t^{exp} - t^{TOF,cal})$	93.8	93.2	94.2
σ_{Cal}	14	10	17

Table 4.2: Standard deviations of the Gaussian fits to the specified time difference distributions for the three scenarios (a), b) and c)). The calibration uncertainty σ_{Cal} (see text) is correspondingly given in the last row.

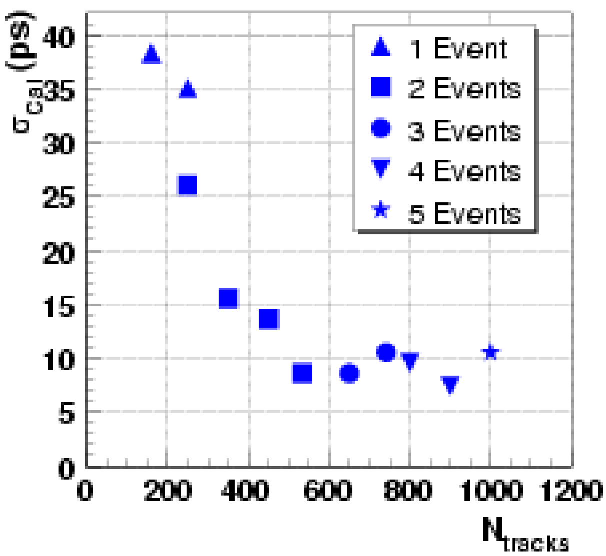

Figure 4.9: Calibration uncertainty as a function of the number of selected tracks/channel used for the determination of the calibration parameters. The different symbols refer to the different numbers of events (HIJING, central Pb+Pb collisions) which are to be collected in order to obtain the corresponding number of tracks.

Obviously, the residual calibration uncertainty depends on the fitting procedure. With respect to this, the number of selected tracks per channel which are used to determine the calibration parameters from the 5$^{\text{th}}$-order polynomial function is a keystone, as Fig. 4.9 clearly shows. This, in turn, affects the number of events which must be collected. As one can see from Fig. 4.9, the uncertainty on the channel-to-channel calibration procedure decreases as the number of selected tracks increases and levels at a value of $\sim$ 10 ps already for $\sim$ 500 tracks, which is actually the statistics used to compute the values of Table 4.2.

It should be recalled that the above estimates are based on a charged particle density $dN_{\mathrm{ch}}/dy \sim 4500$, as derived from HIJING Pb+Pb central events.

4.2.8 Time Delays

The results presented so far have been obtained simulating both the time slewing effect and a hypothetical time delay due to cable and electronics of 2 ns. In order to test the stability of the calibration procedure, different delays have then been introduced in the decalibration step, namely 0, 5, 8, and 10 ns. Actually, some estimates quantifying the time delays due to hardware will be possible prior to calibration in such a way that only smaller residual contributions of a few ns are expected to intervene in the measured times of flight. Anyway, the calibration procedure should be able to correct them as well.

Table 4.3 quotes the uncertainties on the $t^{\mathrm{exp}} - t^{\mathrm{TOF,ND}}$, $t^{\mathrm{exp}} - t^{\mathrm{TOF}}$, $t^{\mathrm{exp}} - t^{\mathrm{TOF,cal}}$ distributions (from the applied Gaussian fits) for the five simulated time delays. Again, scenario b) has been taken as a reference. Figure 4.10 summarizes the results, showing

σ (ps)	0 ns Delay	2 ns Delay	5 ns Delay	8 ns Delay	10 ns Delay
$(t^{\mathrm{exp}} - t^{\mathrm{TOF,ND}})$	92.7	92.7	92.4	92.7	92.7
$(t^{\mathrm{exp}} - t^{\mathrm{TOF}})$	111.4	111.4	110.0	111.4	111.4
$(t^{\mathrm{exp}} - t^{\mathrm{TOF,cal}})$	93.0	93.2	93.1	93.5	94.0
σ_{Cal}	8	10	11	12	16

Table 4.3: Standard deviations of the Gaussian fits to the specified time difference distributions for scenario b), as a function of time delay. The corresponding calibration uncertainty σ_{Cal} (see text) appears in the last row.

the residual calibration uncertainties as a function of the time delay introduced during the decalibration step. Even if a small dependence of the performance of the calibration procedure on the time delay appears, the σ_{Cal} increase with increasing time delay is of the order of a few ps only, which means that the algorithm developed will indeed be able to recover also the residual uncertainties due to cable length and electronics.

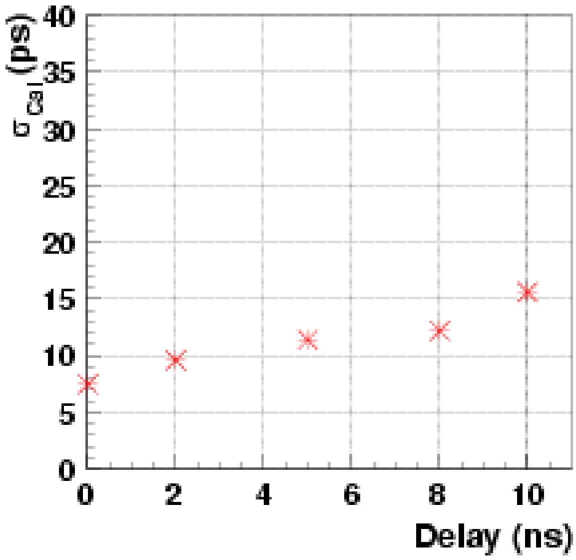

Figure 4.10: Calibration uncertainty as a function of the time delay simulated during decalibration.

4.2.9 Required Statistics

The dependence of the calibration procedure performance on the number of tracks shown in Fig. 4.9 clearly influences the amount of statistics needed to obtain a certain σ_{Cal}. With respect to this, the number of events to be collected, which is a crucial point in high-energy physics experiments, has to be carefully considered.

As Fig. 4.9 shows, in order to have available given numbers of selected tracks (according to the criteria previously listed in this Section), different numbers of events have to be collected. This implies that, since increasing the number of events makes the calibration resolution improve, a longer data-taking period is necessary, as the number of events is larger. Therefore a compromise has to be adopted between the σ_{Cal} value one would like to obtain, and the required statistics.

In the case of Pb+Pb central collisions, the calibration algorithm selects a mean number of tracks per event equal to ~ 250. According to Fig. 4.9, a calibration resolution of the order of ~ 15 ps can be achieved using ~ 500 selected tracks. Since at LHC the

Pb+Pb central event trigger is expected to be acquired at a rate of $\sim$ 10–20 Hz [71], the number of necessary events is $\mathbf{O}(10^5)$.

On the other hand, p+p collisions (which will be the only runs at ALICE start-up), the situation is more complicated. These initial runs will be carried out at LHC at a nominal luminosity $\mathcal{L} = 10^{30}$ cm^{-2}s^{-1} with the requirement to collect the data at the maximum possible rate for the ALICE detectors, which means 1000 events s^{-1}, with an expected average of 100 events s^{-1}. Since in a p+p collision the charged particle multiplicity is much lower (with $\sim$ 2 tracks reconstructed on average in a Minimum Bias event), track reconstruction occurs in a much cleaner environment, which allows to apply selection criteria much less stringent than for the Pb+Pb case. This means that for calibration it will be possible to make use of all the tracks reaching the TOF and producing a signal on it, with no further cut on momentum[10].

As a result, in the case of p+p events, a calibration within $\sim$ 35 ps will still be feasible, with a required event statistics $\sim \mathbf{O}(10^7)$. Considering a Minimum Bias p+p event rate $\sim$ 1000 Hz (for the maximum nominal LHC luminosity during p+p runs), this means $\sim \mathbf{O}(10^4)$ s of data-taking, which is well affordable.

To summarize, the algorithm developed for the ALICE Time of Flight system calibration has shown to be able to correct the measured times of flight for both time slewing effects and time delays due to hardware components. The TOF time resolution can be recovered with a residual uncertainty which depends on the collected statistics, in terms of number of tracks used for the procedure, and of events, which is a crucial point in view of an efficient data taking for physics analysis. Nevertheless, taking into account the data taking rate expected for ALICE, both in the case of Pb+Pb collisions and of p+p runs, the calibration algorithm described in this Chapter will be usable.

4.2.10 The T0 Algorithm

The combinatorial particle identification algorithm described in Sec. 4.2.6 can be used also to determine the Time Zero (T0) of the event, that is, the reference time of the collision. In ALICE, the T0 system is the detector devoted to the measurement of this time. The uncertainty with which it will be able to provide such an information (which is essential for time of flight measurements) is $\sim$ 50 ps (see Table 4.1). This, in fact, is a conservative value set for simulation, which will be replaced with the improved $\sigma_{T0} = 15$ ps that the T0 detector is expected to reach in Pb+Pb collisions.

[10]The $p > 0.4$ GeV/c selection will be in any case applied, since it corresponds to the minimum mo-

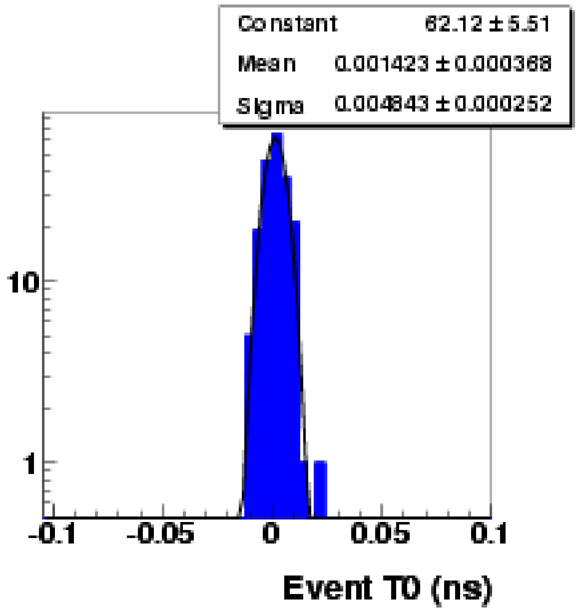

Figure 4.11: Event T0 determination for a sample of 120 HIJING central Pb+Pb events. The Gaussian fit to the distribution is superimposed, and the results of the fit are reported.

The algorithm used for in the particle identification step for the TOF calibration procedure allows to obtain offline even better T0 resolutions. As a matter of fact, reminding Eqs. 4.2, 4.3, 4.4 and 4.5, for each set in which the selected tracks have been subdivided, the $\langle t^0(C^{best})\rangle$ (corresponding to the minimum χ^2) gives the T0 measurement for the set. Then, the T0 of each event is:

$$\mathrm{T0} = \sum_{i=1,\dots N_{sets}} \frac{\langle t^0\rangle/\sigma^2(\langle t^0\rangle_i)}{1/\sigma^2(\langle t^0\rangle_i)}$$

Figure 4.11 shows the results of the event T0 determination for the HIJING central Pb+Pb event sample described in Sec. 2.2.2. From the Gaussian fit applied to the distribution, one can infer that for Pb+Pb central collisions, the event T0 can be measured with an uncertainty of ~ 5 ps. An analysis performed on p+p events has shown that in this case, when the track density is $\mathbf{O}(10^3)$ times lower compared to central Pb+Pb events, the T0 of the event can still be measured with an average resolution of ~ 45 ps. However, in Minimum Bias p+p events, the much lower track multiplicity makes it possible to

mentum necessary for the particle to reach the TOF in the presence of the magnetic field (see Sec. 3.3.2).

determine the event T0 using the above algorithm with at least 2 selected tracks[11] per event only in $\sim 35\%$ of the cases.

[11] In p+p collisions, the cases where only two tracks are found for the T0 algorithm may result in non-Gaussian tails in the event T0 distribution.

Conclusions

The analyses presented in this thesis have shown the highly performing capabilities of the ALICE experiment in studying hadron yields and transverse momentum particle spectra in Pb+Pb central collisions. The basic ingredient for this kind of analysis is particle identification, for which the use of a combined PID technique is an advantageous choice. As a matter of fact, the simultaneous use of the PID information coming from different detectors extends the particle momentum range over which to perform the analysis, keeping the efficiency high with a low contamination.

The number of particles per event which are expected to be identified in a Pb+Pb central collision at LHC makes ALICE the first heavy-ion experiment capable of studying on an event-by-event basis the transverse momentum spectra for the three charged hadrons species π, K and p. This will be important in order to investigate the possible non-statistical fluctuations induced in the p_T spectra (temperature fluctuations) by the expected phase transition from ordinary matter to a quark-gluon plasma.

The sensitivity of the ALICE experiment with respect to dynamical temperature fluctuations has been found to be affected by statistical fluctuations of the order of $\sim 2\%$ for pions and $\sim 7\%$ for kaons and protons. Any further widening of the temperature distributions that may be detected, will be a likely signature of the creation of a new state of matter. The effects of systematic uncertainties on the correction factors for efficiency and contamination applied to the identified particle p_T spectra have been evaluated as well. It has been shown that the mean temperature values for all the three species (π, K and p) do not significantly change, as well as the E-by-E precision with which the temperatures are determined.

Particle ratio fluctuations have also been studied, as one of the most significant signatures of any anomalous strangeness production in heavy-ion collisions. The statistical uncertainty on the K/π and p/π ratios as measured by ALICE will be of the order of $\sim 4\%$ and $\sim 5\%$, respectively. Any other contribution from dynamical fluctuations due to new physics will result in an increase of the observed values.

Obviously, the accurateness with which dynamical fluctuations will be observed depends on the amplitude of the statistical ones. The results presented in this thesis have been obtained from HIJING simulations assuming a charged particle multiplicity per unit rapidity $dN_{ch}/dy \sim 4500$. In case of a reduction of dN_{ch}/dy by a factor $\sim 2 \div 3$ (as recent results from RHIC may suggest), event-by-event studies with ALICE will still be feasible, since the corresponding reduced (by a factor $\sim \sqrt{2} \div \sqrt{3}$) numbers of identified π, K and p would in any case remain high.

Finally, since the performance of the ALICE experiment is strongly influenced by the calibration quality of its detectors, an algorithm devoted to the Time of Flight detector calibration has been developed. The calibration procedure has been shown to be able to correct the measured times of flight with no significant deterioration of the TOF time resolution. The stability of the procedure with respect to the type of TDCs' spectra has been validated, as well as with respect to the time delays introduced to simulate the effects of cable lengths and electornics. As a result, the TOF calibration algorithm will allow to correct, at the same time, time slewing effects and delays from hardware. The required event statistics runs has been evaluated both for Pb+Pb central collisions and Minimum Bias p+p collisions, showing that an accurate TOF calibration will be possible in both cases.

Bibliography

[1] F. Karsch and E. Laermann, Thermodynamics and in-medium hadron properties from lattice QCD, in Quark-Gluon Plasma 3, edited by R. C. Hwa and X. N. Wang (World Scientific, Singapore, 2004), p.1 [arXiv:hep-lat/0305025].

[2] R. D. Pisarski and F. Wilczek, Phys. Rev. D29 (1984) 338.

[3] E. Shuryak, Phys. Lett. B701 (1981) 103.

[4] S. Gavin, A. Gocksch and R. D. Pisarski, Phys. Rev. D49 (1994) 3079.

[5] R. D. Pisarski and F. Wilczek, Phys. Rev. D29 (1984) 338.

[6] F. Karsch, E. Laermann and C. Schmidt, Phys. Rev. Lett. B520 (2001) 41.

[7] F. R. Brown et al., Phys. Rev. Lett. 65 (1990) 2491.

[8] S. Aoki et al., Nucl. Phys. Proc. Suppl. 73 (1999) 459.

[9] Z. Fodor and S. D. Katz, Phys. Lett. B534 (2002) 87.

[10] K. Rajagopal and F. Wilczek, hep-ph/0011333;

R. Rapp, T. Scäfer and E. V. Shuryak, Annals Phys. 280 (2000) 35;

M. Alford, Ann. Rev. Nucl. Part. Sci. 51 (2001) 131;

K. Rajagopal, Comments Nucl. Part. Phys. A2 (2002) 120.

[11] F. Karsch and E. Laermann, Phys. Rev. D50 (1994) 6954.

[12] F. Karsch, E. Laermann and A. Peikert, Phys. Lett. B478 (2000) 447.

[13] T. Matsui and H. Satz, Phys. Lett. B178 (1986) 416.

[14] P. V. Ruuskanen, Photons and lepton pairs: The deep probes of quark-gluon plasma, in Particle Production in Highly Excited Matter, H. H. Gutbrod and J. Rafelski (Eds.), NATO ASI Series B: Physics Vol. 303 (1993) 593 (Plenum, New York).

[15] D. d'Enterria (2003) arXiv:nucl-ex/0302016 and references therein.

[16] L. Van Hove, Phys. Lett. B118 (1982) 138;

L. Van Hove, Z. Phys. C21 (1983) 93.

[17] J. Kapusta, S. Pratt, L. Mc Lerran and H. v. Gersdorff, Phys. Lett. B163 (1985) 253.

[18] H. Von Gersdorff, Nucl. Phys. A461 (1987) 251c.

[19] H. Stöker, A. A. Oglobin and W. Greiner, Z. Phys. A303 (1981) 259.

[20] WA97 Collaboration, F. Antinori et al., Eur. Phys. J. C14 (2000) 633.

[21] PHENIX Collaboration, S. S. Adler et al., Phys. Rev. C69 (2004) 034909.

[22] R. J. Fries, B. Müller and D. K. Srivastava, Phys. Rev. Lett. 90 (2003) 132301.

[23] B. G. Zakharov, JETP Lett. 80 (2004) 1.

[24] J. Kapusta, P. Lichard and D. Seibert, Phys. Rev. D44 (1991) 2774. [Erratum: *ibid* D47 (1993) 4171.]

[25] C. Song, Phys. Rev. C47 (1993) 2861.

[26] D. K. Srivastava, B. Sinha, M. Guylassy and X. N. Wang, Phys. Lett. B276 (1992) 285.

[27] S. Chakrabarty, J. Alam, S. Raha, B. Sinha, and D. K. Srivastava, Phys. Rev. D46 (1992) 3802.

[28] K. Adcox et al., Nucl. Instrum. Meth. A499 (2003) 469.

[29] S. S. Adler et al., Phys. Rev. Lett. 94 (2005) 232301.

[30] J. Rafelski and B. Müller, Phys. Rev. Lett. 48 (1982) 1066;

P. Koch, B. Müller and J. Rafelski, Phys. Rev. 142 (1086) 167.

[31] A. M. Rossi et al., Nucl. Phys. B84 (1975) 269;

NA23 Collaboration, J. L. Bailly et al., Phys. Lett. B195 (1987) 609.

[32] T. Alexopoulos et al., Phys. Rev. D 48 (1993) 984.

[33] STAR Collaboration, C. Adler et al., Phys. Lett. B 595 (2004) 143.

[34] J. Rafelski, Phys. Rep. 88 (1982) 331.

[35] WA97 Collaboration, E. Andersen et al., Phys. Lett. B449 (1999) 401.

[36] M. L. Mangano, Phenomenology of Quarkonium Production in Hadronic Collisions, hep-ph/9507353;

G. A. Schuler, Z. Phys. C71 (1996) 317.

[37] R. Vogt, Phys. Rep. 310 (1999) 197.

[38] J. P. Blaizot and J. Y. Ollitrault, Phys. Rev. Lett. 77 (1996) 1703;

H. Satz, Colour Deconfinement and J/ψ Suppression in High Energy Nuclear Collisions, hep-ph/9711289;

D. Kharzeev, Nucl. Phys. A638 (1998) 279c.

[39] V. Černý, I. Horvát, R. Lietava, A. Nogova and J. Pišút, Z. Phys. C46 (1990) 481;

J. Hüfner, P. Povh and S. Gardner, Phys. Lett. B238 (1990) 103;

J. Cleymans and R. L.Thews, Z. Phys. C45 (1990) 391.

[40] S. Gupta and H. Satz, Phys. Lett. B283 (1992) 439;

R. Vogt, S. J. Brodsky and P. Hoyer, Nucl. Phys. B383 (1992) 643;

M. A. Doncheski, M. B. Ducati and F. Halzen, Phys. Rev. D49 (1994) 1231.

[41] R. L. Thews, M. Schroedter and J. Rafelski, Phys. Rev. C63 (2001) 054905;

R. L. Thews and M. L. Mangano, Phys. Rev. C73 (2006) 014904.

[42] L. Grandchamp and R. Rapp, Nucl. Phys. A709 (2002) 415;

L. Grandchamp and R. Rapp, Phys. Lett. B523 (2001) 60.

[43] A. Andronic, P. Braun-Munzinger, K. Redlich and J. Stachel, Phys. Lett. B571 (2003) 36.

[44] PHENIX Collaboration, K. Adcox et al., Phys. Rev. Lett. 88 (2002) 022301.

[45] STAR Collaboration, J. Adams et al., Phys. Rev. Lett. 91 (2003) 072304.

[46] STAR Collaboration, C. Adler et al., Phys. Rev. Lett. 90 (2003) 082302.

[47] STAR Collaboration, J. Adams et al., Phys. Rev. Lett. 93 (2004) 252301.

[48] For an overview, see Proc. of Quark Matter 2004, J. Phys G: Nucl. Part. Phys. 30 (2004).

[49] H. Sorge, Phys. Rev. Lett. 82 (1999) 2048.

[50] P. F. Kolb, J. Sollfrank and U. Heinz, Phys. Rev. C62 (2000), 054909.

[51] STAR Collaboration, J. Adams et al., Phys. Rev. Lett. 92 (2004) 052302.

[52] PHENIX Collaboration, S. S. Adams et al., Phys. Rev. Lett. 91 (2003) 182301.

[53] P. Huovinen, P. Kolb, U. Heinz, P. V. Ruuskanen and A. S. Voloshin, Phys. Lett. B503 (2001) 58.

[54] P. R. Sorensen, *PhD Thesis* UCLA (2003), nucl-ex/0309003.

[55] R. Hanbury-Brown and R. Q. Twiss, Phil. Mag. 45 (1954) 633.

[56] R. Hanbury-Brown and R. Q. Twiss, Nature 177 (1956) 27;

R. Hanbury-Brown and R. Q. Twiss, Nature 178 (1956) 1046.

[57] G. Goldhaber, S. Goldhaber, W. Lee and A. Pais, Phys. Rev. 120 (1960) 300.

[58] W. Bauer, C. K. Gelbke and S. Pratt, Ann. Rev. Nucl. Part. Sci. 42 (1002) 77;

U. Heinz and B. V. Jacak, Ann. Rev. Nucl. Part. Sci. 49 (1999) 529.

[59] S. Pratt, Phys. Rev. D33 (1986) 1314;

[60] U. Heinz, B. Tomasik, U. A. Wiedemann and Y. F. Wu, Phys. Rev. Lett. B382 (1996) 181.

[61] S. Pratt, Phys. Rev. Lett. 53 (1084) 1219;

A. N. Makhlin and Y. M. Sinyukov, Z. Phys. C39 (1988) 69.

[62] U. A. Wiedmann, Phys. Rev. C57 (1998) 266;

B. Tomasik, U. A. Wiemann and U. Heinz, Nucl. Phys. A663 (2000) 753;

U. A. Wiemann, P. Scotto and U. Heinz, Phys. Rev. C53 (1996) 918.

[63] STAR Collaboration, J. Adams et al., Phys. Rev. C71 (2005) 044906.

[64] M. Harrison, T. Ludlam and S. Ozaki, Nucl. Instrum. Meth. A499 (2003) 235, Special Issue on RHIC.

[65] K. M. Potter, LHC Project Report 36 (1996) and references therein.

[66] B. B. Bach et al., Phys. Rev. Lett. 91 (2003) 052303.

[67] N. Armesto and C. Pajares, Int. J. Mod. Phys. A15 (2000) 2019.

[68] K. J. Eskola, P. V. Ruuskanen, S. S. Rasanen and K. Tuominen, Nucl. Phys. B570 (2000) 379.

[69] M. Nardi, J. Phys. Conf. Ser. 5 (2005) 148.

[70] ALICE Collaboration, Technical Proposal (1995) CERN/LHCC/95-71.

[71] ALICE Collaboration, ALICE: Physics Performance Report Volume I (2003) CERN/LHCC 2003-049, Eds. F. Carminati et al. (ALICE Collaboration), J. Phys. G: Nucl. Part. Phys. 30 (2004) 1517.

[72] A. N. Akindinov et al., Nucl. Instrum. Meth. A533 (2004) 74.

[73] F. Piuz, Nucl. Instrum. Meth. A371 (1996) 96;

E. Nappi, Nucl. Intrum. Meth. A471 (2001) 18.

[74] M. Bedjidian et al., to appear in the CERN Yellow Book of the Workshop Hard Probes in Heavy Ion Collisions at the LHC (2003), hep-ph/0311048.

[75] B. Mohanty and J. Serreau, Phys. Rept. 414 (2005) 263.

[76] ALICE Collaboration, ALICE: Physics Performance Report Volume II (2005) CERN/LHCC 2005-030, Eds. B. Alessandro et al. (ALICE Collaboration).

[77] http://wwwinfo.cern.ch/asdoc/geantold/GEANTMAIN.html.

[78] X. N. Wang et al., Phys. Rev. D44 (1991) 3521;

X. N. Wang et al., Phys. Rev. Lett. 68 (1992) 1480;

M. Gyulassy and X. N. Wang, Comput. Phys. Commun. 83 (1994) 307;

OSCAR, Open Standard Code and Routines, http://nt3.phys.columbia.edu/OSCAR.

[79] R. Fruehwirth et al., Data Analysis Techniques in HEP, 2nd Edition, Cambridge University Press, Cambridge (2000).

[80] P. Billior, Nucl. Instrum. Meth. A225 (1984) 352.

[81] N. Wiener, Extrapolation and Smoothing of Stationary Time Series, Wiley, New York (1949);

W. H. Press, S. A. Teukolsky, W.T. Vetterling and B. P. Flannery, Numerical Recipes, Second Edition, Cambridge University Press, Cambridge (1992).

[82] M. Regler and R. Frühwirth, Reconstruction of Charged Tracks (1990), from Techniques & Concepts of High Energy Physics V, Ed. T. Ferbel, Plenum Publ.;

R. Frühwirth, Application of Filter Methods to the Reconstruction of Tracks and Vertices in Events of Experimental High-Energy Physics (1988), Vienna, HEPHY-PUB-88-516.

[83] R. Brun, F. Bruyant, A. Mc Pherson and P. Zanarini, Geant3 User Guide, CERN Data Handling Division DD/EE/84-1.

[84] ALICE Collaboration, Addendum to the Technical Design Report of the Time of Flight System, CERN/LHCC 2002-16, Addendum to ALICE TDR 8, 24 April 2002.

[85] S. Radomski et al., ALICE Internal Note 2003-008.

[86] J. Velkovska for the PHENIX Collaboration, Nucl. Phys. A698 (2002) 507.

[87] D. Di Bari et al., ALICE Internal Note 2005-048.

[88] D. Di Bari, Nucl. Instrum. Meth. A502 (2003) 300.

[89] R. Stock, Proc. of a NATO Advanced Research Workshop on Hot Hadronic Matter: Theory and Experiment, June 27-July 1, 1994, Divonne, France, Eds. J. Letessier, H. Gutbrod and J. Rafelski.

[90] S. Pratt, Phys. Rev. Lett. 53 (1984) 1219;

T. Csörgö and B. Lörstad, Phys. Rev. C54 (1996) 1390;

U. Heinz and B. V. Jacak, Ann. Rev. Nucl. Part. Sci. 49 (1999), and references therein.

[91] C. L. Bennett et al., Astrophys. J. 583 (2003) 1.

[92] G. de Zotti, L. Toffolatti, F. Argüeso, R. D. Davies, P. Mazzotta, R. B. Partridge, G.F. Smoot and N. Vittorio, The Planck Surveyor Mission: Astrophysical Prospects, Proc. of the EC-TMR Conference held in Rome, Italy, October 1998, Eds. L. Maiani, F. Melchiorri, N. Vittorio, American Institute of Physics 476 (1999) 204 (Woodbury, N.Y.).

[93] M. Stephanov, K. Rajagopal and E. Shuryak, Phys. Lett. Rev. 81 (1998) 4816;

M. Stephanov, K. Rajagopal and E. Shuryak, Phys. Rev. D60 (1999) 114028.

[94] L. Stodolsky, Phys. Rev. Lett. 75 (1995) 1044.

[95] E. Shuryak, Phys. Lett. B430 (1998) 9.

[96] M. Gazdzicki and S. Mrowczynski, Z. Phys. C54 (1992) 127.

[97] H. Heiselberg, Phys. Rept. 351 (2001) 351.

[98] A. Bialas, M. Bleszynski and W. Czyz, Nucl. Phys. B111 (1977) 461.

[99] S. Gavin, Phys. Rev. Lett. 92 (2004) 162301.

[100] WA98 Collaboration, M. M. Aggarwal et al., Phys. Rev. C65 (2002) 054912.

[101] NA49 Collaboration, S. V. Afanasiev et al., Phys. Rev. Lett. 86 (2001) 1965.

[102] PHENIX Collaboration, K. Adcox et al., Phys. Rev. Lett. 93 (2004) 092301.

[103] Q. Liu and T. Trainor, Phys. Lett. B567 (2003) 184.

[104] PHENIX Collaboration, K. Adcox et al., Phys. Rev. C66 (2002) 024901.

[105] NA49 Collaboration, M. Rybczyński et al., J. Phys. Conf. Ser. 5 (2005) 74 [arXiv:nucl-ex/0409009].

[106] PHENIX Collaboration, to appear in the Proceedings of the 18th International Conference on Ultrarelativistic Nucleus-Nucleus Collisions: Quark Matter 2005 (QM 2005), Budapest, Hungary, 4-9 August 2005 [arix:nucl-ex/0510076].

[107] S. Jeon and V. Koch, Phys. Rev. Lett. 85 (2000) 2076;
M. Bleicher, S. Jeon and V. Koch, Phys. Rev. C62 (2000) 061902(R).

[108] M. Asakawa, U. Heinz and B. Müller, Phys. Rev. Lett. 85 (2000) 2072.

[109] H. Heiselberg and A. D. Jackson, Phys. Rev. C63 (2001) 064904.

[110] PHENIX Collaboration, K. Adcox et al., Phys. Rev. Lett. 89 (2002) 082301.

[111] STAR Collaboration, J. Adams et al., Phys. Rev. C68 (2003) 044905.

[112] J. Kapusta and A. Mekjian, Phys. Rev. D33 (1986) 1304.

[113] C. Roland, J. Phys. G: Nucl. Part. Phys. 31 (2005) s1075.

[114] M. Bleicher et al., J. Phys. G: Nucl. Part. Phys. 25 (1999) 1859.

[115] C. Roland, J. Phys. G: Nucl. Part. Phys. 30 (2004) s1381.

[116] S. Das, Contribution to 5th International Conference on Physics and Astrophysics of Quark Gluon Plasma (ICPAQGP 2005), Salt Lake City, Kolkata, India, 8-12 February 2005 [arXiv:nucl-ex/0503023].

[117] L. D. Landau and E. M. Lifshitz, Statistical Physics, (1980), Pergamon Press, Oxford.

[118] R. Korus, S. Mrówczyński, M. Rybczyński and Z. Wlodarczyk, Phys. Rev. C64 (2001) 054908.

[119] W. M. Alberico, A. Lavagno and P. Quarati, Nucl. Phys. A680 (2000) 680.

[120] NA49 Collaboration, A. Appelshäuser et al., Phys. Lett. B459 (1999) 679.

[121] PHENIX Collaboration, K. Adcox et al., Phys. Rev. C69 (2004) 024904.

[122] D. Teaney, J. Laurent and E. V. Shuryak, nucl-th/0110037 (2001);
D. Teaney, J. Laurent and E. V. Shuryak, Phys. Rev. Lett. 86 (2001) 4783.

[123] P. F. Kolb and R. Rapp, Phys. Rev. C67 (2003) 044903.

[124] F. Aghinolfi, P. Jarron, A. N. Martemiyanov, E. Usenko, H. Wenninger, M. C. S. Williams and A. Zichichi, A Ultra-Fast and Low-Power Front-End Amplifier and DiscriminatorASIC Designed for the Multigap Resistive Plate Chamber, Nucl. Instrum. Meth. A533 (2004) 183.

[125] H. Lim and J. Park, Review of Scientific Instruments 74 (2003) 3115.

[126] A. Alici, Proceedings of the VIII Workshop on Resistive Plate Chambers and Related Detectors, Seoul, Korea October 10-12 2005, in preparation.

[127] G. Scioli, Proceedings of the VIII Workshop on Resistive Plate Chambers and Related Detectors, Seoul, Korea October 10-12 2005, in preparation.